Fused Filament Fabrication of Prosthetic Components for Trans-Humeral Upper Limb Prosthetics

By

Steven M. Lathers

A Dissertation Presented in Partial Fulfillment
of the Requirements for the Degree
Doctor of Philosophy

Approved August 2017 by the
Graduate Supervisory Committee

Jeffrey La Belle, Chair
David Vowels
Thurmon Lockhart
James Abbas
Troy McDaniel

ARIZONA STATE UNIVERSITY

December 2017

ABSTRACT

Presented below is the design and fabrication of prosthetic components consisting of an attachment, tactile sensing, and actuator systems with Fused Filament Fabrication (FFF) technique. The attachment system is a thermoplastic osseointegrated upper limb prosthesis for average adult trans-humeral amputation with mechanical properties greater than upper limb skeletal bone. The prosthetic designed has: a one-step surgical process, large cavities for bone tissue ingrowth, uses a material that has an elastic modulus less than skeletal bone, and can be fabricated on one system.

FFF osseointegration screw is an improvement upon the current two-part osseointegrated prosthetics that are composed of a fixture and abutment. The current prosthetic design requires two invasive surgeries for implantation and are made of titanium, which has an elastic modulus greater than bone. An elastic modulus greater than bone causes stress shielding and overtime can cause loosening of the prosthetic.

The tactile sensor is a thermoplastic piezo-resistive sensor for daily activities for a prosthetic's feedback system. The tactile sensor is manufactured from a low elastic modulus composite comprising of a compressible thermoplastic elastomer and conductive carbon. Carbon is in graphite form and added in high filler ratios. The printed sensors were compared to sensors that were fabricated in a gravity mold to highlight the difference in FFF sensors to molded sensors. The 3D printed tactile sensor has a thickness and feel similar to human skin, has a simple fabrication technique, can detect forces needed for daily activities, and can be manufactured in to user specific geometries.

Lastly, a biomimicking skeletal muscle actuator for prosthetics was developed. The actuator developed is manufactured with Fuse Filament Fabrication using a shape memory polymer composite that has non-linear contractile and passive forces, contractile forces and strains comparable to mammalian skeletal muscle, reaction time under one second, low operating temperature, and has a low mass, volume, and material costs. The actuator improves upon current prosthetic actuators that provide rigid, linear force with high weight, cost, and noise.

TABLE OF CONTENTS

Page

LIST OF TABLES

Table Page

LIST OF FIGURES

Figure Page

Figure Page

CHAPTER ONE: INTRODUCTION

In the United States, there are approximately two million with limb loss with 185,000 people losing a limb each year; with hospital costs of approximately $8.3 billion for amputations each year. 54% lose a limb to a vascular disease including diabetes and peripheral arterial disease, 45% to a physical trauma and fewer than 2% to cancer with a ratio of upper limb to lower limb loss of 1:4[1-9]. Prosthetics can cost up to $50,000 per limb with the possibility of the majority not being covered under insurance[10,11]. Additionally, many prosthetics need to be replaced as the user grows, while insurances will not typically cover the cost of continual replacement.

Prosthetics are composed of an attachment system to the amputated limb, a support structure/skeleton, a functional end (i.e. hand/gripper), and a system to provide movement and force through the functional end (i.e actuator). Additionally, prosthetics can be equipped with a feedback/control system for touch and prosthetic control depending on the type of prosthetic.

There are currently two main types of prosthetics: body powered and electric motor powered (intelligent) prosthetics. A body powered prosthetic is typically composed of rigid cables attached to a functional end and to a secondary attachment system. Where the main attachment system allows the prosthetic to be attached to the amputation sight, and the secondary system is attached at an intact anatomical joint. For example, an amputation below the elbow with a prosthetic hand, the secondary system could be

attached to the shoulder joint. When the shoulder is displaced (forward/backwards or up/down) the prosthetic hand opens or closes.

An intelligent prosthetic is a prosthetic system that uses DC/servo motors to apply movement and force to the functional end and joints with the addition of a feedback/control system. Where the muscle or neural electrical signals are collected to control the prosthetic and motors, and pressure, shear, temperature, or visual sensors are to provide feedback to the wearer.

Currently, both types of prosthetics and their components are mass manufactured with current industry practices. This would include injection molding, metal forming/extrusion, CNC, hand assembly of complex components, and hand forming/molding of components. With the current practices, this results in prosthetics that are: expensive due to the large overhead costs associated with industry manufacturing, heavy components due to out dated designs and products, limited availability to various markets/regions, complex systems/components with multiple integrated components, and systems that are designed for one user size/functionality.

To overcome these pitfalls, additive manufacturing 3D printing can be implemented. Additive manufacturing is a process by which: a 3D model file is converted into various horizontal slices, with a defined thickness, then a material is deposited on to a bed/platform to replace each digital slice representation. For example, a square CAD file can be cut/sliced into 10 horizontal slices/layers, where the horizontal slice is parallel

to the bed, and then material from a fabrication/extrusion point is applied to each slice/layer. Once material is placed in a layer, the fabrication point begins to place material in the next layer moving in a vertical direction.

This manufacturing technique is accomplished through various techniques including Fused Filament Fabrication (FFF), Stereolithography (SLA), Selective Laser Sintering (SLS), or Selective Laser Melting (SLM). FFF uses a polymer filament with a hot end extruder as the material fabrication point (MFA). SLA uses a container filled with two or more monomers, a photocatalyst, and a light emitting device (MFA). SLS or SLM has a container filled with a powdered polymer (SLS) or metal (SLM), and a light emitting device (MFA). Where the light emitting device in either SLA, SLS, or SLM allows for material to be placed in each layer.

Additive manufacturing allows for complex parts or devices to be: fabricated on one system, manufactured to fit a user's anatomy or specifications, manufactured with embed parts/systems simultaneously, create fully assembled systems on one machine, switch quickly and effectively between various materials, and a decrease in overhead costs making it available to more users and regions.

With the new technology available, the purpose of this dissertation is to develop prosthetic components that are functional and manufactured on one system via FFF. Components developed were focused on attachment, tactile sensing, and actuation/movement devices. These three components were chosen since they represent

the major systems that impact the user's prosthetic functionality and acceptance. Additionally, Fused Filament Fabrication was chosen since it allows for a wide array of compatible material. Any thermoplastic polymer/composite can be used with FFF since the system simply extrudes material, in filament form, out the hot extruder end on to the bed/build platform.

The following chapters will show the development and functionality of a one surgical step osseointegrated attachment system, a flexible conductive thermoplastic pressure and shear tactile sensor, and a biomimicking skeletal muscle actuator using a shape memory polymer composite (SMPC) for trans-humeral amputations.

CHAPTER TWO: BACKGROUND LITERATURE

FUSED FILAMENT FABRICATION OSSEOINTEGRATION SCREW FOR TRANSHUMERAL AMPUTATIONS

Current upper limb prosthetics can weigh up to eight pounds, and sometimes more for trans-humeral prosthetics. These types of prosthetics are then attached to the user with either a socket and sleeve system or with an osseointegrated prosthesis. Osseointegration prosthetics are a one or two-part system that allows an abutment or shaft to attach directly to the skeletal bone system and protrude out from the user's skin for a prosthetic to attach to.

Prosthetics are commonly attached to the user with a socket and sleeve system due to their lower costs, degree of formability to the amputated limb, and easiness of implementation for the wearer. The pitfalls of a socket and sleeve system are user discomfort due to changes in stump shape throughout the day caused by swelling, the socket shifting during use, and sweat pooling due to little or no airflow throughout the socket for heat exchange.

The socket and sleeve systems also have weak attachment strengths when compared to the osseointegrated systems since the socket and sleeve are only attached to the users' skin. The prosthetic can "wobble or have play" in them since they are only being attached to the skin, which allows for movement caused by the skin being able to move relative to the muscle and the muscle relative to the bone. Lastly, socket and sleeve systems cause a loss of sensation for the user by the socket creating a barrier between the socket and the user's skin, which does not allow forces or vibrations to be transferred to the user directly.

To overcome the pitfalls associated with socket and sleeve systems, an osseointegrated prosthesis is used since it is a direct attachment to the skeletal bone. This allows for forces and vibrations to be sensed by the user's nervous system through their skeletal structure, and helps reduce and sometimes eliminate the pain associated with phantom limb[12,13,14].

There are many different types of osseointegrated prosthetics that include: cylindrical/coned rods that are press fitted into the medullary cavity, an "x-shape" rod that allows bone tissue ingrowth into the voided space, and two-part systems that are composed of a sleeve and abutment that protrudes out of the skin. The abutment either attaches with a tapered press fit or has threads to engage with the sleeve[15], with threaded sleeves and abutment/screws being the ideal attachment system. Osseointegrated screws are a two-part system being composed of a fixture/sleeve and abutment, see figure 1, with outer threads to create fixation to the bone and inner threads to allow the abutment to attach to. The system allows the bone to grow around and into the threads of the fixture with a porous surface to create a hard fixation point first and then using the abutment for the external prosthetic to attach to. The two-part system is inserted surgically in two separate surgeries, with one to insert the fixture/sleeve with a six-month healing time and a second one to insert the abutment, which then requires 12 -16 months of recovery/rehabilitation to be able to put full force on the system.

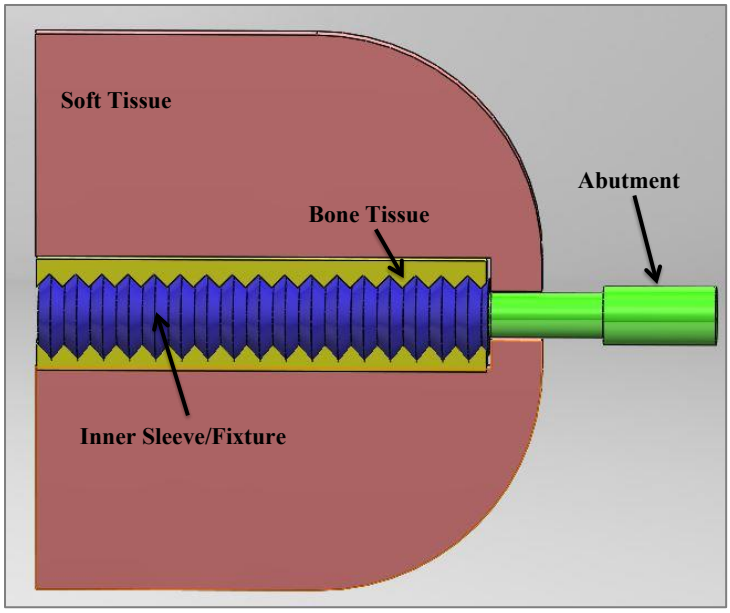

Figure 1. Schematic of Trans-Humeral amputation with a two-part osseointegrated prosthesis screw implant.

These current osseointegrated prosthetics are made from titanium for its biocompatibility and high strength. The two-part systems described here have long recovery times, are made of a material that has an elastic modulus around 120GPa, when the elastic modulus on cortical bone is between 12 – 16GPa, which causes stress shielding to the bone. This shielding causes the skeletal bone cells to pull away from the site of fixation since they are not receiving any forces that would require bone cell formation, which can then cause loosening of the system. Lastly, the current osseointegrated screws do not allow for large amounts of bone ingrowth in to them, cannot be quickly or easily manufactured to match the users anatomical shape/size of their skeletal bone shafts, and require multiple invasive surgeries.

To overcome the pitfalls of titanium osseointegrated screws, a Fused Filament Fabrication (FFF) 3D printed osseointegrated screw is developed. The screw uses a

polyamide six based material, designed to withstand forces seen during a fall, have large area for bone ingrowth, and decrease rehabilitation time.

INITIAL CADAVER FIXATION STRENGTH AND POLYMER LEACHING OF FFF 3D PRINTED OSSEOINTEGRATION SCREW FOR LONG-TERM TRANSHUMERAL AMPUTATION IMPLANTS

Continuing from the previous work on a FFF osseointegration screw for upper limb trans-humeral amputation[38], research involves performing initial FFF 3D printed polymer cytocompatibility with human osteoblast cells and evaluating the fixation strength of the 3D printed osseointegration screws in fresh frozen cadaver humeri at initial insertion, or time zero.

Initial biocompatibility was performed with a cytotoxicity test and incubation in Phosphate Buffer Saline (PBS) solution. The cytotoxicity was performed with a 48-hour cytotoxicity test with human osteoblast cells to determine if the polymer was toxic to the cells. A 48-hour cytotoxicity, per ISO 10993-1 FDA guidance, is used as the initial step taken to determine a medical device's compatibility. Where the FFF polymer was allowed to incubate in the PBS solution at 37^0C for 30+ days with a 1:5 ratio of polymer to PBS. A PBS solution is used due to its physiological equivalent pH value to create an in vitro environment[49] and 30+ days of incubation is used since the FDA recommends testing permanent implant devices for >30days.

FUSED FILAMENT FABRICATION 3D PRINTED PRESSURE SENSOR FOR PROSTHETICS WITH LOW ELASTIC MODULUS AND HIGH FILLER RATIO FILAMENT COMPOSITES.

Current intelligent prosthetics use feedback systems to relay important information back to the user. One type of feedback system uses tactile sensors to relay touch/contact of the prosthetic with an object. The sensors relay to the user when the prosthetic has come in to contact with an object, the amount of force applied to that object, and how it is situated within/on their prosthetic. Tactile sensors are typically composed of a pressure or shear sensor, and sometimes contain both. A pressure sensor detects forces acting perpendicular to its loading surface, whereas a shear sensor detects forces acting parallel to its surface.

When referring to upper limb prosthetic pressure and shear sensors, these sensors are typically placed on the hand of the prosthetic due to the role they play in manipulating objects and daily activities. Sensor types include capacitive, piezo-resistive/electric, inductive, optoelectric, and strain gage based[62]. The main design types used for current prosthetics for detecting pressure, or shear, are strain gage sensors.

Strain gage sensors provide a large operating range that can detect very high or low-pressure values, but suffer from being bulky and expensive. This forces the prosthetic fingers to be large and decreases the fine motor grasping function of the prosthetic. Having less bulky sensors allows the fingers to have improved fine motor control and greater ease when manipulating large or small objects.

To overcome the barriers of strain gage sensors, academic research has developed many different types/styles of pressure sensors, most commonly referred to as thick or

thin film sensors. These thick/thin film sensors are mostly piezo-resistive/electric based sensors, but can be transistor, capacitance, or optical based, and can achieve high and low force detection. Additionally, this type of sensor design has been used for shear force detection too.

Each of these two sensors has their benefits but they lack in the areas of size, feel, and manufacturing techniques. As stated before, strain gage sensors are bulky and expensive, while thick/thin film sensors do not have a synthetic skin feel or appearance, have complicated manufacturing processes, high costs, and difficulty being implemented on to a prosthetic.

The film-based pressure sensors in research have been shown to detect low-pressure values, down to 0.001Pa, and high-pressure values of 200kPa[63-73]. These pressure values are well within the human skin threshold for pressure detection, where human skin is able to detect between 100Pa - 1MPa, with the pressure required for common daily tasks being 10kPa[74].

The secondary sensors, shear sensors, are currently designed to detect low levels from 0-0.8N, mid-range levels from 0-2N, or higher levels from 0-8N; the exact detection level is not the end factor for prosthetic use. The ultimate factor is to detect shear forces or movement across the sensors surface that would results in the loss of grasp on an object; where a ratio less than one, in equation 1, would represent the prosthetic digit sliding across a surface. Equation 1 is the equation for minimum grasp strength where the

normal to tangential reaction forces ratio is multiplied by the static coefficient of friction, μ_F, and exceeds a value of one, equation 1[75].

$$1 < \mu_F * \frac{F_{Normal}}{F_{Tangential}} \qquad (1)$$

Thick/thin film sensors are simply composed of: a top and bottom flexible layer, an inner conductive layer, and then a top and bottom electrode surface for signal recording. To demonstrate the complex manufacturing seen with thick/thin film sensors, a few common film sensor designs are described below: 1) A micropillar array based pressure sensor with the active pressure sensing area is comprised of PPy/PDMS substrate and an Au covered micropillar array. The pillars would have a repeating cell unit of 70.0 μm × 120.0 μm with the diameter of the pillars varying from 5 μm to 65 μm. 2) A microstructured rGO/PDMS film and ITO-coated PET film, that was created through the use of silicon mold masters created from a photolithography method. The molds were then subjected to the elastomer precursor, which created a base layer to do a layer-by-layer fabrication method to add layers of uniform microstructure graphene to the elastomer surface. Or 3) A laminating two layers together, where the bottom layer contains a source-drain electrode and the semiconducting polymer and the top contains the gate electrode and the microstructure dielectric[65, 66, 70].

These film sensors can detect the typical forces for daily activities and even forces beneath a light touch on human skin. But to fabricate these sensors, they require

complicated manufacturing processes and are subsequently expensive due to the materials used and complex fabrication. Additionally, the sensors do not create a look or feel similar to human skin, and have a hard or smooth plastic finish that makes it difficult to be implemented on a prosthetic.

To overcome the pitfalls of strain gage and thick/thin film tactile sensors for prosthetics, a Fused Filament Fabrication (FFF) 3D printed piezo-resistive pressure and shear sensor for daily activity sensing was developed. The 3D printed tactile sensor is manufactured out of a composite comprising of a low elastic modulus compressible thermoplastic elastomer, and carbon, in graphite form, as the conductive material in high filler amounts.

FUSED FILAMENT FABRICATION 4D PRINTED BIOMIMICKING ACTUATOR WITH PLA AND TPU SHAPE MEMORY POLYMER COMPOSITE FOR PROSTHETIC ACTUATORS.

Actuators are used to provide movement and force to joints within a prosthetic device. For upper-limb prosthetics, this would include digit/wrist manipulation, grip force, and rotation at the elbow. To achieve these types of outputs, an actuator that provides linear output or translates rotational energy to a linear force/direction is needed.

For upper-limb amputations, current prosthetics use either a body-powered system or an electric/intelligent system. Body-powered prosthetics use a system of cables and pulleys that allow the user to actuate the prosthetic with the use of an intact anatomical

system. Body powered systems are lightweight, inexpensive, lack complexity, but generate low force output with no feedback system. Whereas electric systems use high powered DC/servo motors with a control system that collects input from electrodes monitoring muscular (EMG) or neural (EEG) activity and has a feedback system. The downside to electric systems are that they are expensive, heavy, and generate noise pollution. For example, EMG control hands can weigh between 31.75% - 86.5% more than the average human hand[82-83], making it difficult/uncomfortable to wear since the weight is being applied to soft tissue instead of the skeletal system.

Both body and electric powered systems cannot provide an actuated motion that mimics bulk skeletal muscle. This is due to the motors and their control system providing a linear output and the body-powered system using rigid cables to transfer force and motion, which generates a linear output. Where bulk skeletal muscle generates a non-linear output under contraction/active and passive movements, with the output changing depending on the muscle's stretched length.

To overcome the issues with current actuators, academic research has developed many different types of actuators that include pneumatic or soft robotic actuators, shape memory alloys, large thermal expansion materials, combination mechanical and tissue engineered systems, thin films, nanofibers, and shape deposition manufactured[84-93].

Pneumatic or soft robotic actuators[84,85] use compressed air or fluid to transfer into specific chambers within an actuation system, where the chambers are independent of

one another. This allows the system to fill specific chambers with fluid and creates a structure that deforms to grasp/move objects. The disadvantage is that these systems are complex, require a source of compressed fluid, and can be heavy relative to their size.

Shape memory alloys (SMA) and thermal expansion materials[86,87] can generate high force per weight characteristics with heat by changing microstructure orientation/phase or by reversible, directional thermal expansion. Shape memory alloys have the benefit of being able to memorize a shape and then recover back to its memorized shape when deformed.

Both materials require high temperatures, up to 120°C, for actuation/displacement which can decrease actuation response time, and have low strain recovery, where SMA's can only achieve a maximum of eight percent. Additionally, thermal expansion materials require an applied load to hold it in a deformed position so it can recover a shape when heated.

Lastly, mechanical/tissue engineered, thin films, nanofibers, or shape deposition manufactured[88-93] actuators have been used to create actuators but either require living skeletal muscle cells, complex nanowire/fiber manufacturing and structure, or requires embedded electronic components. Actuators with living cells or nanofibers can generate high or physiological comparable strain rates, but have living cells that need nutrients and require complex manufacturing. Additionally, current shape deposition manufactured

actuators still require the use of embedded electronics during the printing process to create an actuator, but these actuators still provide a linear output.

To overcome the issues of high operating temperatures, low contractile strain, complexity, high weight and cost, and linear output, a Fuse Filament Fabrication (FFF) 3D printed shape memory polymer composite (SMPC) actuator was developed.

CHAPTER THREE: FUSED FILAMENT FABRICATION OSSEOINTEGRATION SCREW FOR TRANSHUMERAL AMPUTATIONS

INTRODUCTION

To overcome the pitfalls of titanium osseointegrated screws previously stated, the development of a Fused Filament Fabrication (FFF) 3D printed osseointegrated screw was performed, which will allow for the complex geometries and customized shapes to be manufactured with large volumes for bone in growth[16]. The osseointegrated screw will be a one step process where the patient will only have one surgery to get the screw implanted, have tissue scaffolding for bone growth into the screw for increased attachment strength, a flanged head to allow for pretension to be generated in the screw to prevent the screw from moving during tissue ingrowth, manufactured out of a polyamide six based material, and meet the average forces seen during a fall with hands stretched all the way out. The polyamide-six based material was chosen since it is widely used in sutures and other devices that interface with the soft tissue of the body.

There have been many advances in Fused Filament Fabrication 3D printing of medical devices but none for osseointegrated screws or prosthetics that require higher strength or implantation. Current research includes a larger area of topics but some key areas include tissue scaffolding[17], anatomical molds for veterinarian research[18], surgical and patient training[19,20], tissue regeneration guide[21], and prosthetic hands/fingers[22,23].

MATERIALS AND METHODS

All parts were printed on a Maker Gear M2 and tested on an Instron Model 1331 (maximum load cell capability of 10,000lbs) or Model 4411 (maximum load cell capability of 900lbs). Parts were created using SOLIDWORKS 3D CAD software and custom tensile and three-point bending, figure 2, test fixtures were fabricated to accommodate the unique screw design. Lastly, the filament was dried in an oven at 79°C for 36 – 48 hours for a 30 gram roll of filament to ensure that all the moisture was removed before printing.

The FFF 3D printed osseointegrated screw was made from a polyamide-six based material made by Taulman 3D, the filament used is Taulman 680 FDA 1.75mm diameter with an elastic modulus of 0.197GPa. The material is an FDA approved material, designed to meet FDA 21CFR177.1500. Part 177, for food storage and handling, can be sterilized with ethylene oxide or steam/boiling, and has been used for tissue scaffolding and prosthetics[24,25]. The polyamide-six base material was chosen because these materials have shown positive results for the use of bone tissue regeneration[26,27,28].

Figure 2. Three-point bending test fixture for FFF 3D printed osseointegrated screw.

To determine the optimal print settings, tensile and shear tests were performed with various variables, with a sample size of N=1 for each variable. Dog bone (DB) samples, following ASTM D638-14 design shape for tensile testing of plastics, were printed with two shells, and four top and bottom solid layers with the percent infill adjusted from 10% to 100% in 30% increments. The layer heights for the dog bone samples were printed at 0.15mm. This makes the solid top and bottom 4 layers only 37.5% of the total sample thickness with the infill making up 62.5% of the sample. Shear samples were printed with 10 shells, and four top and bottom solid layers with the layer height adjusted from 0.10mm to 0.30mm with 0.05mm increments. Both tensile and shear

samples had the infill printed at 45° angles that inverted or rotated between each layer, so if layer one is at 45°, then layer two is at -45° and so on. Figure 3 shows sample parts and results; samples were tested on the Instron model 4411 to provide greater accuracy at the lower force levels.

Following these tests, the optimum percent infill of 100% and layer height of 0.15mm were chosen to print the osseointegrated screw with. The 100% infill was chosen due to it providing the highest strength and the 0.15mm providing a tradeoff of print time and detail accuracy. When a layer height of 0.10mm was used, the FFF screw would begin to warp during manufacturing since the part would cool much faster than the larger layer height. Printer settings on the MakerGear were 600mm/min for printing speed, extruder temperature at 267°C, print bed at 100°C, and auto generated supports. The chosen speed and temperatures provided the best print quality with a maximum printing time of 17 hours.

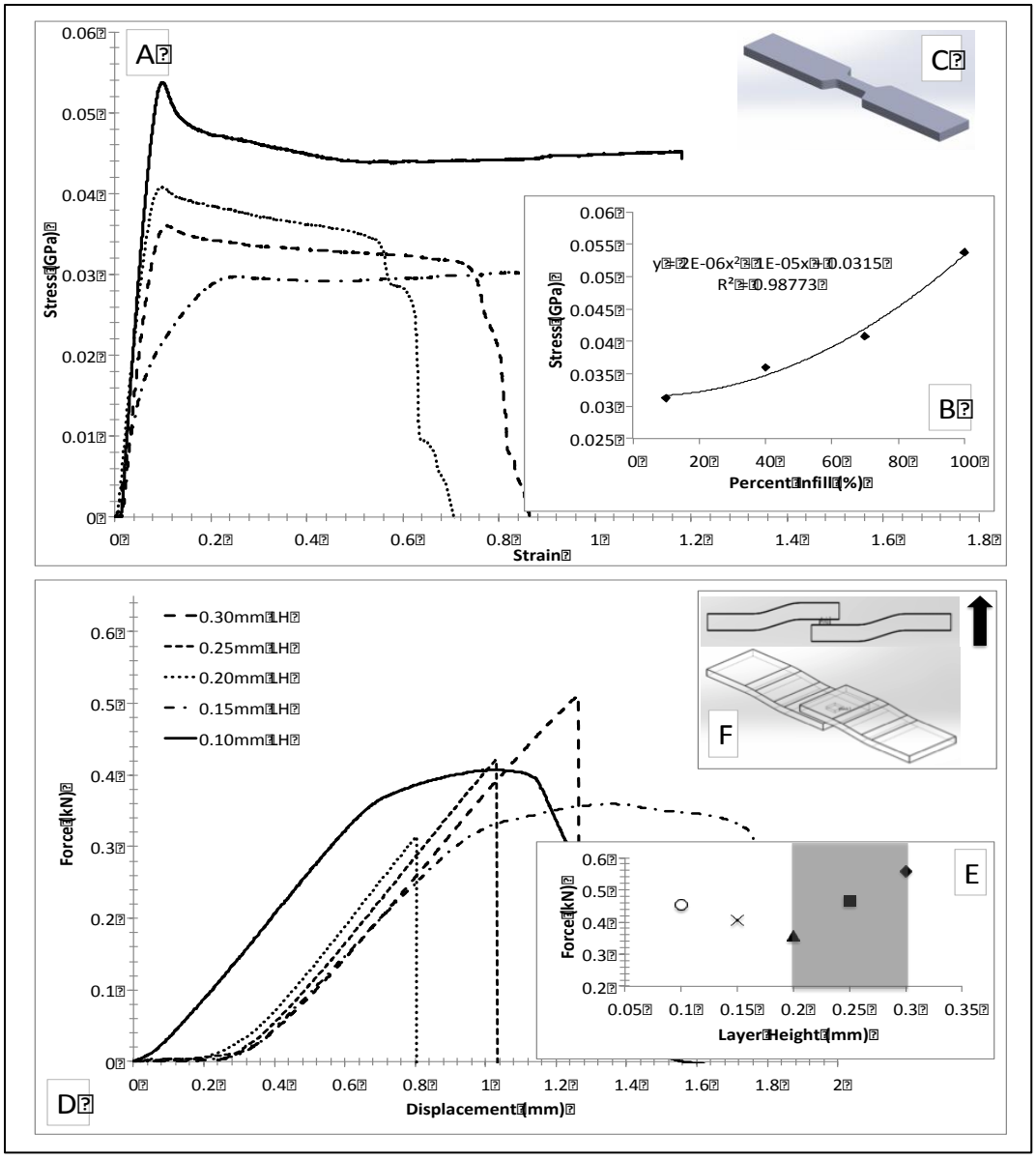

Figure 3. (A) Tension dog bone force vs displacement data (solid line is 100%, dotted line is 70%, dash line is 40%, and dash dot is 10% infill, (B) Tensile stress peak force vs dog bone percent infilll, (C) Dog bone test sample, (D) Shear force vs displacement data, (E) Peak shear force vs 3D printer layer height, grey zone represents the increase in moment arm and cross-sectional area (legend: circle is 0.10mm, cross is 0.15mm, triangle is 0.20mm, square is 0.25mm, and diamond is 0.30mm), and (F) Shear test sample with the printing direction indicated by the bold arrow (the bottom of the arrow indicating the platform of the 3D printer and the top arrow indicating the direction the nozzle direction in the z-axis). All data has an error of 0.5% or less, error was determined by testing Instron with calibrated weights prior to testing.

Next, the screw design was evaluated with SOLIDWORKS finite element modeling (FEM) software. Four different designs were evaluated: a simple four fin design, four fin with a center rod, four fin with a center rod and ribs, and a four fin with center rod and external double helix, see table 1. This FEM evaluation was to determine what designs would work best with a finned screw shape. The optimal design was a finned screw with center rod and ribs. The helix design did provide an overall stronger design, but the helix covered too much of the surface to allow area for tissue scaffolding, therefore the ribbed design provided a strength increase but did not obstruct the area for scaffolding and provided multiple anchor points for the tissue scaffolding.

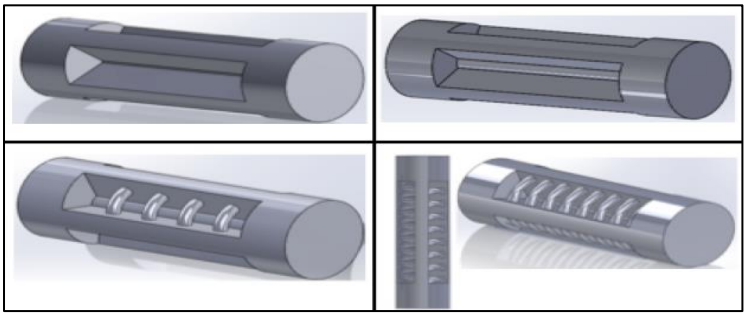

	Δ Stress (%)		Δ Displacement (%)	
	Tension	Bending	Tension	Bending
Fins Only (Baseline)	0.00	0.00	0.00	0.00
Fins with Center Rod	-95.60	1.45	-89.65	-9.58
Fins with Center Rod and Ribs	3.21	1.67	-10.34	-10.62
Rod and Double Helix	24.09	-99.83	-3.65	-99.82

Table 1. Results of FEM simulations of the multiple osseointegrated screw designs under a give load.

RESULTS

After characterizing the material and determining the ideal screw design, the screw was printed with an overall diameter of 20.00mm with a 2.50mm thread pitch. The screw was manufactured to match the current overall diameter titanium sleeves that are used[29,30]. Tensile and three-point bending tests, with a sample size of N=1, were performed on the osseointegrated screw with the Instron model 1331 since the screw had absorbed 6568.33N (1476.62lbs) in tension and 5256.37N (1181.68lbs) in bending before failure, which exceeded the load cell of the 4411 model. A small sample size was used due to the long print times, and material and testing equipment availability.

Testing samples include a three and four fin design with a center rod of nine millimeters in diameter and ribs. Samples were printed longitudinally or parallel to direction of applied tension to provide the greatest strength since printing perpendicular to the direction of applied tension would result in a weaker part due to the layer adhesion strength of FFF parts, this same effect has been seen here[31].

All samples were threaded into four M20x2.50 steel nuts with nickel coating to simulate a rigid fixation that would be seen when the screw is fully implanted into the bone canal of the patient. For the three-point bending tests, the samples were tested with the applied force perpendicular and parallel to the flange design since the flange is a partial flange and does not completely wrap around the head of the screw, see figure 4.

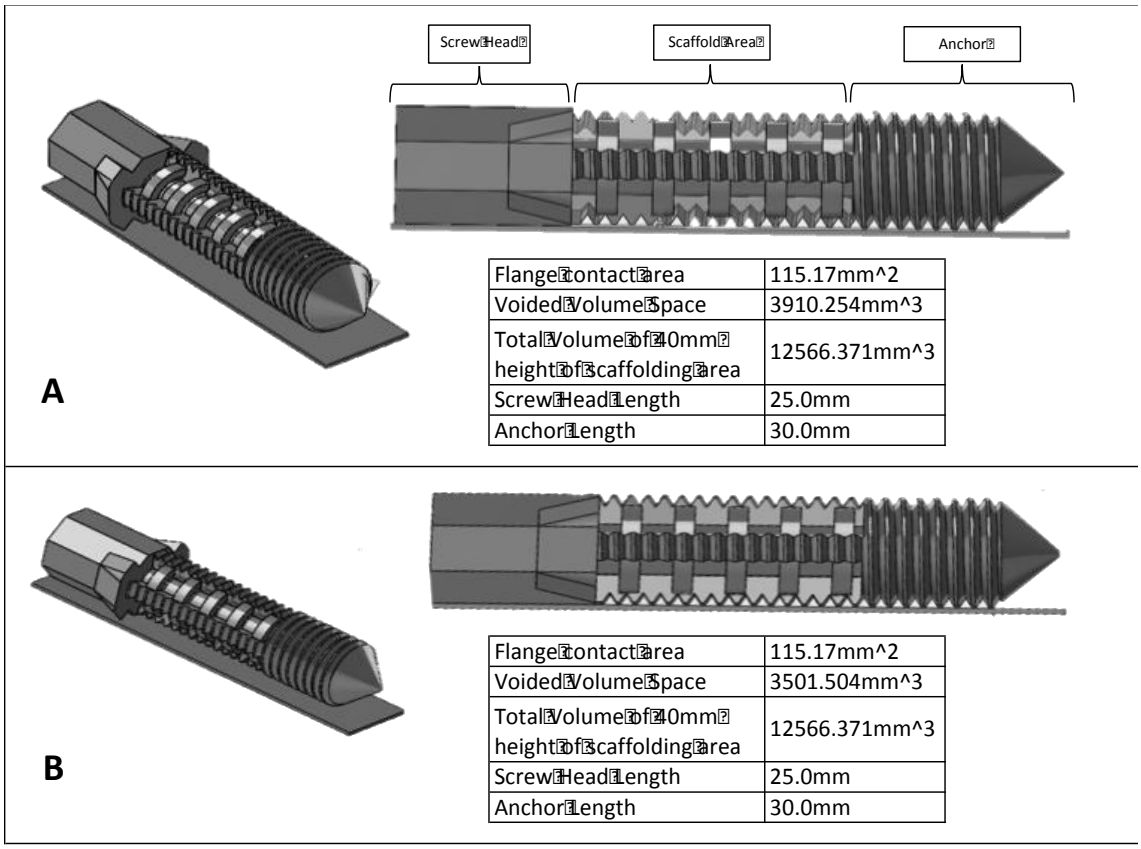

Flange contact area	115.17mm^2
Voided Volume Space	3910.254mm^3
Total Volume of 40mm height of scaffolding area	12566.371mm^3
Screw Head Length	25.0mm
Anchor Length	30.0mm

Flange contact area	115.17mm^2
Voided Volume Space	3501.504mm^3
Total Volume of 40mm height of scaffolding area	12566.371mm^3
Screw Head Length	25.0mm
Anchor Length	30.0mm

Figure 4. Three-finned (A) and Four-finned Fused Filament Fabrication 3D printed osseointegrated screw dimensioning.

In both tension and bending, the four-fin design performed better in tension due to the increase in cross-sectional area and the applied force parallel to the flange has a higher resistance to bending due to the increase in area moment of inertia. In figure 5, the tensile and three-point bending sample force versus displacement results can be seen. A force versus displacement graph was used to allow for easier comparison to literature on osseointegrated prosthetics.

The screw was designed to meet the average force seen at the wrist of 500.00lbs or 2.20kN at an average fall height and up to a maximum value of just over 900.00lbs or

4.00kN seen at a fall height of six meters[32]. The force seen at the wrist was chosen since it sees the greatest force during a fall. The shoulder and elbow see less of a force because they have the degree(s) of freedom to displace during a fall and decrease the force seen at that joint and subsequent body parts around them. Where the wrist makes a hard contact with the ground during a fall and provides no deflection on contact with a surface.

Additionally, torque-to-failure with initial creep tests were performed to demonstrate the storage of linear tension generated by torsion and the maximum seating torque. Figure 5 shows the seating and break-off torques and torque-to-failure values. The FFF osseointegrated screws were seated to 3.00Nm, given five minutes to settle, then loosened to remove tension, and then repeated two more times. After performing the creep tests, the samples were taken to failure. The seating torque value needed to fall between 4.00Nm and 0.50Nm, representing a secure and loose-fitting implant for insertion[29]. These seating values represent osseointegrated titanium prosthesis used for femur attachment. Femur attachments require higher strength and seating values than humerus attachment, therefore using these as a requirement/thershold gives the screw design presented here a safety factor.

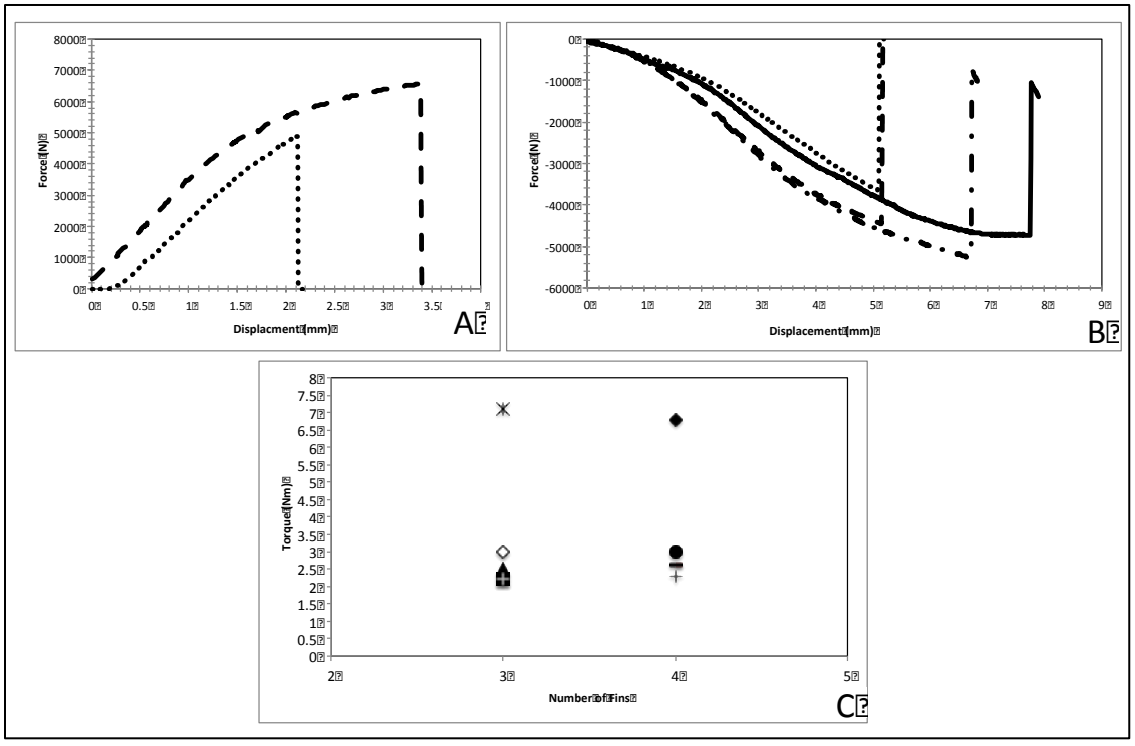

Figure 5. 3D printed osseointegrated screw tension, dash line is four fin and dotted line is three fin (A), three-point bending, dash-dot line is four-fin parallel, dash line is three fin parallel, solid line is four fin perpendicular, and dotted line is three fin perpendicular (B), and seating/loosening torques, and torque-to-failure test results, triangle and circle are seating torques, star and diamond-filled are failure torques, and all others are loosening torques (C).

DISCUSSION

MATERIAL CHARACTERIZATION

The results from the dog bone (DB) and shear samples show that print settings can affect the strength of the design and portray unique performance characteristics for the layer height when using Taulman 680 FDA. The dog bone sample performance curves follow a trend of increased strength with increased percent infill. Using 100% infill was chosen since it provided the greatest strength and created the densest part. Having a denser part allows the device to absorb more energy and be more durable for

the potential user. The dog bone samples were designed to match the ASTM D638-14 for testing tensile strength of plastics, this way the tensile strength of the FFF 3D printed part can be compared to plastic injected or molded parts.

Individual tensile dog bone samples demonstrate an unusual trend just after peak load is collected. The DB sample does not follow a continuous decline in load; the sample begins to fail, stabilizes, and then continues its failure. This stabilization is due to the fact the infill layers collapse, become more aligned with the loading direction, and then fail as a whole unit. This effect is not seen as substantially at the lower percent infill, 10%, since the infill layer percentage is small and has little influence over the strength of the sample.

A shear testing sample was created to determine the layer height strength with different printing layer heights. Figure 3 shows the shear sample shape and the direction of printing, indicated by the bold arrow. The shear sample is created with two s-shape bars that allow the square in the center of the bars to align with the direction of applied tensile force. This printing direction causes the layers within the square to be subjected solely to the applied tensile force. This allows the strength of each layer thickness to be determined. The shear sample was made with 10 shells instead of two to ensure that there would be no deformation in the bars like what was seen with the DB samples. The increase in shells allow for more layers in the direction of the applied force to create a stronger tensile modulus.

Results from the shear testing show a unique curve that was not originally anticipated. The graph shows a parabola curve for peak layer height (LH) strengths, where a linear curve was original anticipated, figure 3. The results show that the thickest layer height, 0.30mm, has the strongest shear strength, 0.20mm being the weakest, and then a gradual increase as the layer height heads toward 0.10mm. This parabola curve appears to confirm that a thicker layer height is strongest since it has a greater cross-sectional area compared to the smaller layer heights. With the smaller LH, there is greater layer fusion and decrease in moment generated, which causes the increase in strength. While the middle sample, 0.20mm, has the weakest since it has a smaller cross-sectional area (CSA) compared to the 0.30mm LH but has less layer fusion and a greater moment generated during testing compared to the lower LH. This play of both smaller CSA and greater moment causes the 0.20mm to have the weakest shear strength.

No samples were printed at a layer height lower than 0.10mm because the machine has not been calibrated to accurately and consistently print beneath that. The Maker Gear M2 can print at layer heights lower than 0.10mm, but it requires modifications to the machine and many printing trials to get it to print at that level. Due to this, we did not print any below 0.10mm to eliminate the variable of inconsistency.

FFF 3D PRINTED OSSEOINTEGRATED SCREW TESTING

After completing the preliminary testing, three and four fin osseointegrated screws were printed to test the maximum tension and three-point bending strength. Inserting the screw into the four steel nuts, clapping the head of the screw in to the

Instron, and then grabbing the top nut surface with our custom test fixture was performed to test the samples in tension. Samples failed just beneath the head of the nut, within the fins and center rod of the screw, and with linear fracture lines perpendicular to the applied force. All samples failed appropriately within the smaller CSA and demonstrated a brittle type of fracture with little yielding. This property is not consistent when referring to polyamide-six based materials, but since the Taulman 680 FDA is a cross-linked polyamide-six material this follows an appropriate trend.

Three-point bending samples were performed in a non-conventional way to demonstrate the strength of the screw if it were in a more realistic implant environment then compared to the standard three-point bending test. The screw was placed in to the four steel nuts and then rested on the u-shape test fixture with the contact points being 22.60mm and 38.00mm from the applied force, with the smaller distance being the contact point for the head of the screw. The nut closest to the flange of the screw had a sleeve fixed to its surface where the test fixture above could push while inserted in to the sleeve. This allowed the applied force to be applied downward on the object and not slip off in one direction, see figure 2. All samples failed with tension on the distant edge and compress on the near edge of the applied force.

For the three-point bending test, the samples were tested with the applied force perpendicular and parallel/inline to the flange. The flange was not created to wrap around the entire screw design to ensure a minimal design that could leave additional area for possible skin/skeletal muscle scaffolding on to the head of the screw for future prototypes

to reduce infections[29]. The bending samples with the applied force parallel to the flange had the greatest strength due to the larger CSA and area moment of inertia.

The last form of testing that was completed was the creep and torsion tests. To demonstrate that the sample to could be repeatedly seated at a torque and backed-off after a settling time and still be within the range of a loose and tight fitting osseointegrated prosthetic. The screw needs to be able to be seated during the rehabilitation process to allow for bone growth into the area dedicated for bone tissue scaffolding. If the screw rotates during this process, the bone that has currently formed would be broken and displaced causing that bone fixation to be remodeled. Once the bone has formed enough into the voided areas, it will prevent the screw from being rotated accidently during the rehabilitation process. All seated samples had a maximum decrease of 26.70% from the original seated torque to the back-out torque. Additionally, all samples had a maximum failure torque of 6.80Nm-7.30Nm, which is above the ideal tight-fitting implant of 4.00Nm.

DESIGN IMPACT/ADVANTAGES

The FFF 3D printed screw presented here has a bending stiffness (K) of 769.26N/mm within the simulated environment at a maximum displacement of 6.833mm, and a bending moment (M) of 118,793.74Nmm (118.79Nm) to screw head (M_h) and 199,741.69Nmm (199.74Nm) to steel nut contact (M_n). Extrapolating this data out to the forces seen in the referenced paper[34], the printed screw would be able to hold 12.14% more load at the same moment distance as the synthetic humeri and 69.11% more load at

the same moment distance as the cadaver humeri. The cadaver and synthetic humeri bones have bending moments of 36.7Nm and 104.9Nm respectively.

The printed screw also has a pull-out strength of 6,568.33N, which is larger than the axial pullout strength of cemented osseointegrated prosthesis in a femur[34] and is larger than the pull-out forces seen on a sheep animal model of an osseointegrated prosthetic at time zero before bone ingrowth and three months after bone ingrowth[35]. Here we are only comparing the values of titanium cemented and seat osseointegrated prosthetics to demonstrate that the 3D printed screw has similar or improved fixation tensile strength in its working environment. The osseointegrated prosthesis, titanium or the 3D printed one presented here, would fail at the bone-prosthetic interface prior to maximum loading of the cortical bone. Where the tensile strength of an average humeri bone is approximately 40,000N, using an average adult cross-sectional area and stress of 125MPa for humeri bone[36].

This screw can withstand loads greater in bending than what the skeletal bone can handle, causing the bone to break before the FFF 3D printed screw does, even with the large cavities design for large volume of bone ingrowth. This puts a higher level of safety that the screw will not fail and cause an open wound to the user that could lead to severe heath concerns.

Additionally, the screw has an elastic modulus of only 0.197GPa, meaning that stress shielding will be seen significantly less than its titanium counterparts' due to its

increased compliance. This will result in bone continuing to form instead of reabsorbing and removing itself from the site of the implant. Having this effect is beneficial for bone tissue growth since the area will continually see stress and will want to keep building/rebuilding bone cells at the site, preventing prosthetic loosening. Having an elastic modulus well below that of bone has been shown to prevent stress shielding when using the material PEEK[33,37], PEEK has an elastic modulus of only 3.6-3.9GPa.

DESIGN PITFALLS/DISADVANTAGES

The pitfalls/disadvantages to the FFF osseointegration screw is the material's lack of implantation history, and possibility of polymer pitting and screw movement during bone ingrowth. Current osseointegration screws use titanium which has a long history for internal implants that interface with bone. Titanium has a been used for internal hip/knee replacements, dental implants, bone fixture plates and screws, and bone scaffolding; which provides it with a long successful history. Additionally, titanium will not pit or erode away due to its metallic properties, allowing its surface to be uncompromised in-vitro.

Since the FFF osseointegration screw uses a polymer material it has the possibility of eroding when placed in an aqueous environment, which can prevent it from being a successful long-term implant. Additionally, its one step design opens the possibility of it rotating during bone ingrowth. If the screw where to have a large force impacted on it, it could rotate and cause the bone ingrowth process to start over again.

The flange head is designed to prevent this, but since it is a step design there is the possibility for rotation, which would increase the rehabilitation time.

FFF 3D PRINTING PITFALLS

Throughout the FFF printing process, a few minor issues were observed when printing. First, we had to print at a much higher temperature then what is recommended from the Taulman 3D site of only 238°C, where we needed to print at 267°C to get high quality prints with the semi-transparent, very light tan finished parts. Secondly, we had to print with a solid 0.90mm thick platform on the bottom of our CAD model file to ensure that the threads would stick since they were the first layer on the platform. Lastly, the parts were modeled and printed with an overall diameter of 19.00mm and a thread pitch of 2.55mm due to tolerances in the machine and material expansion during printing.

CONCLUSIONS

We present here an alternative to current titanium osseointegrated prosthetics with a thermoplastic FFF 3D printed osseointegrated screw that can withstand forces greater than an average humeri bone. The screw is a one-step surgical procedure for implantation with large volumes of bone ingrowth, which will allow for an increase in fixation strength.

The one step design will allow for a significant decrease in rehabilitation time since the patient does not need to go through two surgeries, which is necessary for the current osseointegration system. We are proposing a maximum decrease in rehabilitation

time of six months due to the one step surgical design; an animal study is needed to confirm the actual decrease time. The six-month time frame comes from the removal of the first surgery that is required for the two-part titanium osseointegration screw fixture/sleeve. Having a flange head will allow for pretension of the prosthetic for fitting and rehabilitation. The device can also be customized to the patient's body with an FFF 3D printer for a point-of-care medical device.

Additionally, the design presented here will have a manufacturing cost of approximately $5.91, ignoring equipment over head and surgery costs. It is very difficult to find the exact cost of a titanium osseointegrated screw since there are multiple processing and finishing steps in order to have a final product that is compatible with the human body and each supplier can perform different manufacturing steps.

The 3D printer material and medical grade titanium are approximately equal for cost per kilogram of material. The cost reduction comes into play with the manufacturing and processing of the screw, and the density difference between the two materials. The 3D printer screw only requires one step until a final product is manufactured, where the titanium based screws require multiple processing and finishing steps to create the final product. Additionally, the density of medical grade titanium is approximately four times greater than the Taulman 680 filament. This allows the 3D printer filament to have four times the volume of material per same cost compared to titanium.

CHAPTER FOUR: INITIAL CADAVER FIXATION STRENGTH AND POLYMER LEACHING OF FFF 3D PRINTED OSSEOINTEGRATION SCREW FOR LONG-TERM TRANSHUMERAL AMPUTATION IMPLANTS

INTRODUCTION

The continued research presented below on the FFF osseointegration screw shows initial biocompatibility via polymer leaching, cytotoxicity testing, and screw fixation strength prior to bone ingrowth. An initial 36day polymer incubation study was performed by incubating the FFF 3D printed polymer in to a phosphate buffer saline solution along with a 48-hour live-dead assay to determine the polymer's cytotoxicity to human osteo cells. Cadaver samples were tapped and threaded to measure the fixation strength of the screw in three-point bending and torsion. Positive initial results show that the polymer causes minimal to no rejection from the body during the 48-hour cytotoxicity test. Additionally, there is minimal change in mechanical properties when implanting the screw in a cadaver sample instead of a simulated steel environment, see chapter three.

MATERIALS AND METHODS

The material used for manufacturing the FFF 3D print osseointegration screws was Taulman3D Nylon 680 due to it being a nylon-6 based material, that currently has FDA approval, designed to meet FDA 21CFR177.1500. Part 177, for food storage and handling, can be sterilized with ethylene oxide or autoclav, and has been used for tissue scaffolding and prosthetics[38,39]. Additionally, the polyamide-six base material was chosen because these materials have shown positive results for the use of bone tissue regeneration[4,40,41,42,43]. The osseointegration screws were FFF 3D printed on a Maker

Gear M2 and the three-point bending tests were performed on an Instron Model 1331 (maximum load cell capability of 10,000lbs). Lastly, the 3D printed rings and discs used for the cytocompatibility testing were design in SOLIDWORKS 3D CAD software.

Osseointegration screws were printed with the optimized settings of 100% infill and a layer height of 0.15mm. The 100% infill was chosen due to it providing the highest strength and the 0.15mm providing a tradeoff of print time and detail accuracy. Printing methods, procedures, and material characterization results are shown in detail in chapter three, or our original paper[38], on the FFF 3D printed osseointegration screw.

The fresh frozen non-preserved cadaver samples were donated by the MORE Foundation and were of a 68-year-old male at 73inches in height and a body weight of 230lbs, and a 67-year-old male at 71inches in height and a body weight of 250lbs. A total of three cadaver samples were donated for testing. Cadaver samples were stored at -20^0C but were tested at -10^0C due to transportation and temporary storage of the samples during testing. Samples were kept in an insulated cooler while three-point bending and torsion tests were performed.

Cytotoxicity of leached material into solution was determined using the U-2 OS human osteosarcoma cell line (ATCC HTB-96) since this material has not been tested for its cytotoxicity. Although U-2 OS has several genomic aberrations and is highly proliferative, the cells are still vulnerable to cytotoxins such as rotenone and tumor-suppressor activation, as demonstrated in previous work[44]. Prior to performing the

cytotoxicity tests, the FFF 3D printed parts were sterilized using a Steris Autoclave SG-120. The samples were placed in CROSSTEK autoclave sealable bags and then were sterilized. Autoclave settings used were a one-minute purge followed by a 30minute sterilization time at 121.0^0C, then were dried under a 10.0inHg vacuum for 30minutes. Following sterilization, the bags were kept at room temperature until the cytotoxicity testing was performed.

U-2 OS cells were grown to 90% confluency in a T-75 flask in complete growth medium (McCoy's 5A, 10% fetal bovine serum, 1% penicillin streptomycin) at 37ºC in a 5% CO_2 humidified incubator. To generate treated medium, a 8mL sample of sterilized FFF 3D printed material was incubated in 40mL complete growth medium with slow agitation (30 rpm on a Labnet H5600 Revolver Rotator) at 4ºC for 72 hours. U-2 OS cells were washed with 5.0mL 1x PBS, harvested with 2.0mL trypsin-EDTA buffer, and brought up to ~1.0E6 cells/mL with 8.0mL complete growth medium. Cells were diluted to ~1.0E5/mL in either treated medium (1:10 resuspended cells to treated medium) or growth medium (control). Diluted cells were seeded at a density of ~ 25 cells/mm^2 in each well of a 12-well tissue culture plate in the presence or absence of a of a 3D printed ring or disc (15mm outer diameter, 2mm height). Cells were grown at 37ºC, 5% CO_2 for 24hours. The medium in each well was replaced with fresh treated or control medium as appropriate and cells were grown for an additional 24hours. Images of cultured cells were captured directly from plates by wide field microscopy using phase contrast at 100x magnification on a Nikon Eclipse T.i instrument via NIS-Elements software v. 4.12. To prepare samples for flow cytometry, cells were washed with 0.5mL 1x PBS, harvested

with 0.25mL trypsin-EDTA buffer, and resuspended with 0.75mL growth medium. Cells were pelleted at 200 xg for 5minutes and resuspended in 0.5 mL 1x PBS. A dead cell control sample was generated by incubating one of the untreated samples at 65^{o}C for 10 minutes. All samples were stained with 1.0µL green SYTOX dye (S34860) swirled to mix, and incubated at room temperature for 20minutes. Stained samples were passed through 35µm strainers into 6mL tubes analyzed using a BD Accuri C6 flow cytometer with CFlow Plus software. Raw data fcs files were processed using FlowJo v.10.1

Lastly, the polymer was tested in a Phosphate Buffer Saline (PBS) solution and allowed to incubate at 37^{0}C for 36days with a 1:5 ratio of polymer to PBS, 1.5mL of polymer was used to incubate with. A PBS solution is used due to its physiological equivalent pH value to create an in vitro environment[45] and 36days of incubation is used since the FDA recommends testing permanent implant devices for >30days. Well samples included blank, deionized water, PBS, and PBS with incubated polymer at 96hours, 144hours, 192hours, 336hours, and 864hours (36days) of incubation time. One PBS tablet from Calbiochem® was dissolved in a 1.0L bottle to create the PBS solution.

RESULTS

Cadaver samples were first dimensionally analyzed to determine the outer diameter of the FFF 3D printed osseointegration screw for testing, see figure 6 for cadaver dimensioning locations and overall sample shape. The three different cadaver samples had dimensions listed in table 2, and show the minimum and maximum diameters measured in each region. Since the cadaver samples do not have perfectly

round shapes, the minimum and maximums were needed to appropriately determine the size osseointegration screw that could be implanted. Samples one and two had a similar shape and dimensions, while the third sample had much larger portions seen at the middle and upper regions of the cadaver Humerus. The sample has an average increase of 66%, 45%, and 15% in the upper, middle, and lower regions compared to samples one and two. Cadaver samples were taken from the middle region and then cut and threaded.

After reviewing the cadaver sample dimensions, it was determined that samples one and two would receive an M14x2.0 screw and sample three would receive an M20x2.5mm, which is the original screw dimensions from chapter three, or our previous work[38]. The M14x2.0mm and M20x2.5mm sizes were used because they are standard thread sizes and profiles used in practice and industry, while the M20x2.5mm matches the outer diameter used in current titanium osseointegration screws[46,47]. The scaled down M14 screw size was only scaled down in the x and y axis leaving the z-axis or overall length unchanged.

From here, the M20 screw would be used as the comparison to our simulated steel environment torsion data collected and the two M14 screws will be used as the comparison to the simulated steel environment three-point bending data collected in chapter three.

Tested samples were a four-fin design with a center rod and external ribs, see figure 7. Samples were printed longitudinally or perpendicular to the direction of applied

force during the three-point bending test to provide the greatest strength since printing parallel to the direction of applied force would result in a weaker part due to the layer adhesion strength of FFF parts, this same effect has been seen here[48].

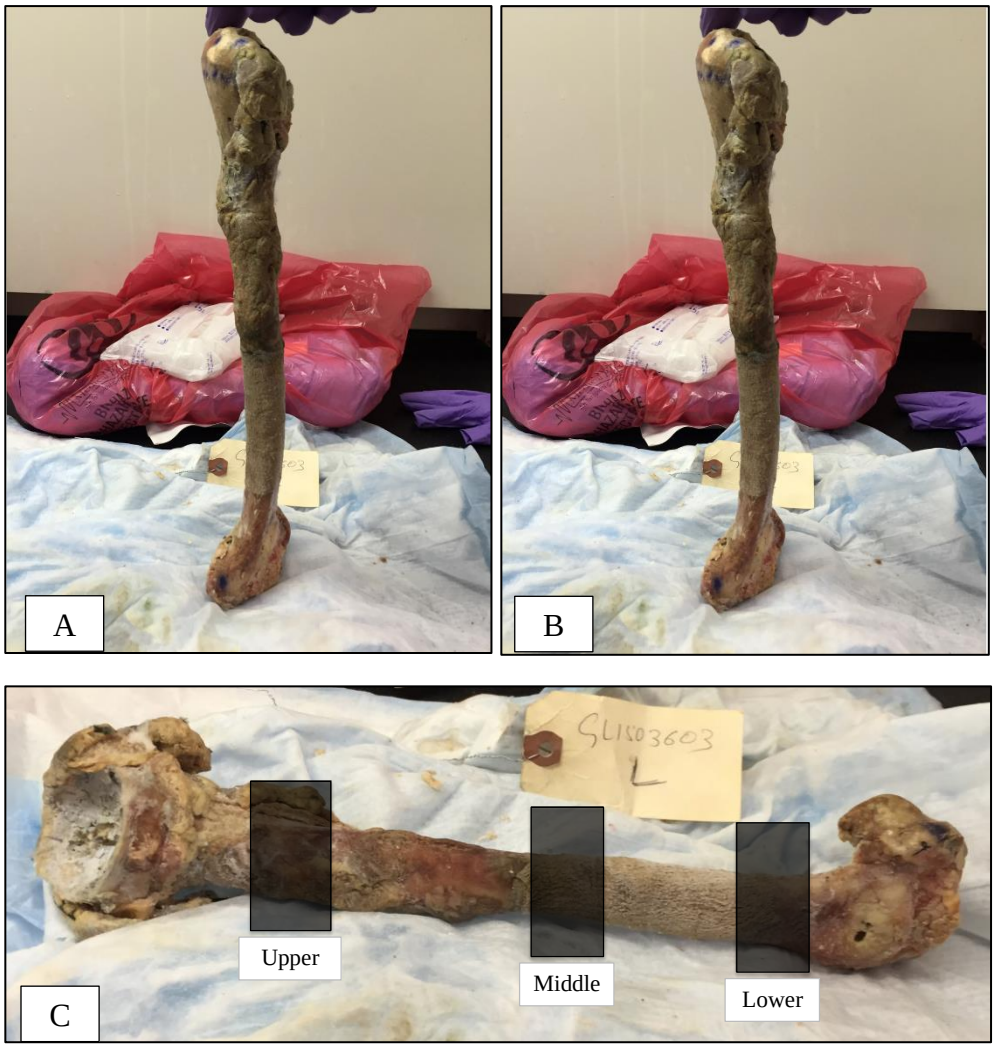

Figure 6. Top (A, B) and bottom row images show the cadaver sample shape. Bottom (C) row image shows the three locations were dimensions were taken. Dimensions were taken with the black shaded regions for the top, middle, and bottom portions of the samples.

Dimensions	Upper (mm)	Middle (mm)	Lower (mm)	Length Between Upper and Lower Region (mm)
Sample 1	23x24	19x21	21x23	190
Sample 2	22x24	19x22	19x21	210
Sample 3	28x32	22x27	22x23	240

Table 2. Dimensional analysis of cadaver samples. Upper, middle, and lower columns represent the upper, middle, and lower regions seen in figure 6.

Figures 8 and 9, and table 3 show the comparison results of the three-point bending and torsion testing, and post testing failure images. A force versus displacement graph was used to allow for easier comparison to literature on osseointegrated prosthetics. The previous M20x2.5mm simulated steel environment bending test recorded a maximum of 5256.37N (1181.68lbs) in bending before failure while the scaled down M14x2.0mm reported a maximum bending force of 2325.93N (522.89lbs) in the simulated environment. While the M14x2.0mm in the cadaver sample achieved a maximum bending force of 1609.76N (361.89lbs).

Additionally, the M20 screw was tested for initial creep and torsion tests in the cadaver sample, figure 9. To demonstrate that the sample to could be repeatedly seated at a torque and backed off after a settling time and still be within the range of a loose and tight fitting osseointegrated prosthetic. The screw needs to be able to be seated during the rehabilitation process to allow for bone growth into the area dedicated for bone tissue scaffolding. If the screw rotates during this process it could cause the newly formed bone to break off and displace causing the bone fixation to be remodeled. Once the bone has

formed enough into the voided areas, it will prevent the screw from being rotated accidently during the rehabilitation process. The seated cadaver sample had a maximum decrease of 34.38% from original seated torque to the back-out torque, while the simulated sample had a maximum decrease of 26.70% from the original seated torque to the back-out torque. Additionally, the cadaver and simulated sample had a maximum failure of 8.10Nm and 6.80Nm respectively, which is above the ideal tight-fitting implant of 4.00Nm.

In order to determine the impact of the 3D-printed material on live cells, we asked whether compounds that are leached from the material into the extracellular environment are toxic[49,50,51,52]. We used U-2 OS osteo cells to perform a 48 hour live-dead assay and observed no evidence of toxicity. A sterile sample of 3D printed material was allowed to soak in growth medium for 72 hours to encourage leaching. This treated medium was applied to cultured U-2 OS cells and viability was measured after 48 hours. From an initial seeding density of ~ 25 cells/mm^2, the control and treated samples reached the expected coverage of ~100 cells/mm^2, or 90-100% confluency. Furthermore, we observed no obvious differences in cell morphology (Figure 10-A). This result indicates that leached medium does not impede cell proliferation. Next, we used SYTOX staining and flow cytometry to determine the proportion of live and dead cells in each sample. In a control experiment, we compared heat-stressed dead cells (incubated at 65^{o}C) to untreated control cells. The dead cell sample showed lower forward scatter and higher side scatter signal, a typical indicator of cell death[53]. The dead cell sample also produced a SYTOX signal that was well above background, by about two orders of magnitude

(Figure 10-B). We used these data to set a SYTOX threshold gate (histogram in Figure 10-B) to distinguish live and dead cells in the experimental sample set. The proportion of live and dead cells did not vary significantly from the control for cell populations that were exposed to test medium or to solid samples of the 3D printed material (disc or ring-shaped) (Figure 10-C).

To further determine if any substances were leaching out of the polymer, the polymer was incubated in phosphate buffer saline solution (PBS). The incubated solution was tested for fluorescence absorbance to determine if any chemicals were released into the solution. Absorbance was taken from 200nm to 1000nm wavelength to give a wide spectrum, with values taken every 10nm. 250μL of each solution was placed in each well. Test well samples included a blank, deionized water, PBS solution, and PBS solution incubated with the polymer, with a sample size of N=3. The results, figure 11 and 12, show that there is minimal change or increase in optical density when the polymer is incubated at 37^0C for 36days, while 48hours to 192hours shows no change from the baseline reading of PBS only solution. There is additionally a change in mass 6.67mg, 0.415% of overall mass, due to hydrolysis of the polyamide-based polymer.

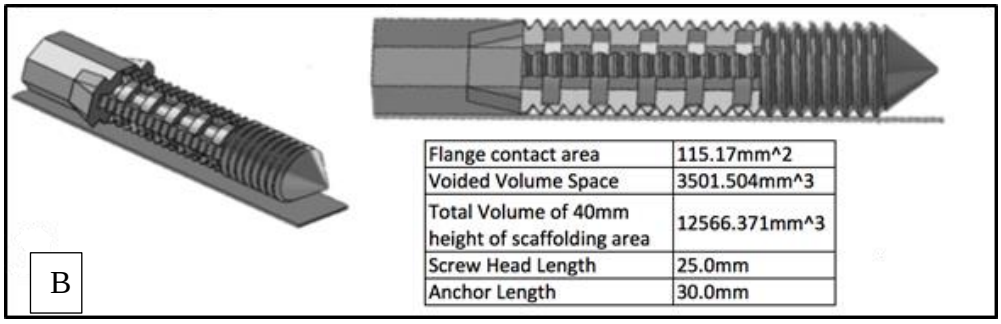

Flange contact area	115.17mm^2
Voided Volume Space	3501.504mm^3
Total Volume of 40mm height of scaffolding area	12566.371mm^3
Screw Head Length	25.0mm
Anchor Length	30.0mm

Figure 7. (A) Three-point bending test fixture for FFF 3D printed osseointegrated screw. (B) M20x2.5mm osseointegration screw with four fins. Anchor Length represents the far right threaded portion and the Screw Head represents the far left portion of the screw with the flange.

DISCUSSION

FFF 3D PRINTED OSSEOINTEGRATED SCREW TESTING

For the three-point bending tests, the cadaver samples were tested with a 14mm outer diameter screw instead of the 20mm diameter due to the cadaver sample

dimensions. Since only three samples were available to us and with the two smaller samples with similar dimensions, they were chosen for the three-point bending tests. Additionally, using the 20mm diameter screw on the smaller samples would not be possible since the cadaver samples would be destroyed in the process. Therefore, the three-point bending tests had simulated and cadaver samples tested to show the changes from a simulated (steel) to an implant-like environment.

The M14x2.0mm samples were threaded into five nickel coated steel nuts for simulated testing or threaded into cadaver samples, which were tapped and threaded to receive the M14x2.0mm osseointegration screw. The samples were then tested for three-bending strength with the applied force perpendicular and parallel to the flange design since the flange is a partial flange and does not completely wrap around the head of the screw, see figure 7 for screw design and test fixture. The applied force parallel to the flange has a higher resistance to bending due to the increase in area moment of inertia and cross-sectional area. The screws had contact points with the u-shaped test fixture of 22.60mm and 38.00mm from the applied force, with the smaller distance being the contact point for the head of the screw. The unique three-point bending test fixture was used to provide a more realistic implant environment then compared to the standard three-point bending test.

A partial flange design was used to develop a minimal design that could leave additional area for potential skin/skeletal muscle scaffolding on to the head of the screw for future prototypes to reduce infections[46]. The results show that the maximum bending

value is seen when the force is applied parallel to the flange instead of perpendicular to it, see figure 8. This data trend is equally present in both the M14 and M20 FFF 3D printed screws.

For the three-point bending results, the M14 screw had a maximum bending stiffness (K) of 292.69N/mm and 262.04N/mm within the simulated environment in the perpendicular and parallel orientations respectively. Within the cadaver environment, the screw had a maximum bending stiffness (K) of 147.82N/mm and 146.49N/mm in the perpendicular and parallel orientations respectively.

Additionally, the M14 FFF 3D printed screw had bending moments (M) of 25763.39Nmm (25.76Nm) and 52566.23Nmm (52.57Nm) to the screw head (M_h) in the perpendicular and parallel orientations respectively. The screw also had bending moments to 43318.97Nmm (43.32Nm) and 88385.69Nmm (88.39Nm) to the steel nut contact (M_n) within the simulated environment. In the cadaver environment, the screw had bending moments (M) of 22942.04Nmm (22.94Nm) and 36380.58Nmm (36.38Nm) to the screw head (M_h) in the perpendicular and parallel orientations respectively. The screw also had bending moments of 38575.11Nmm (38.58Nm) and 61170.89Nmm (61.17Nm) to the cadaver end contact point (M_n).

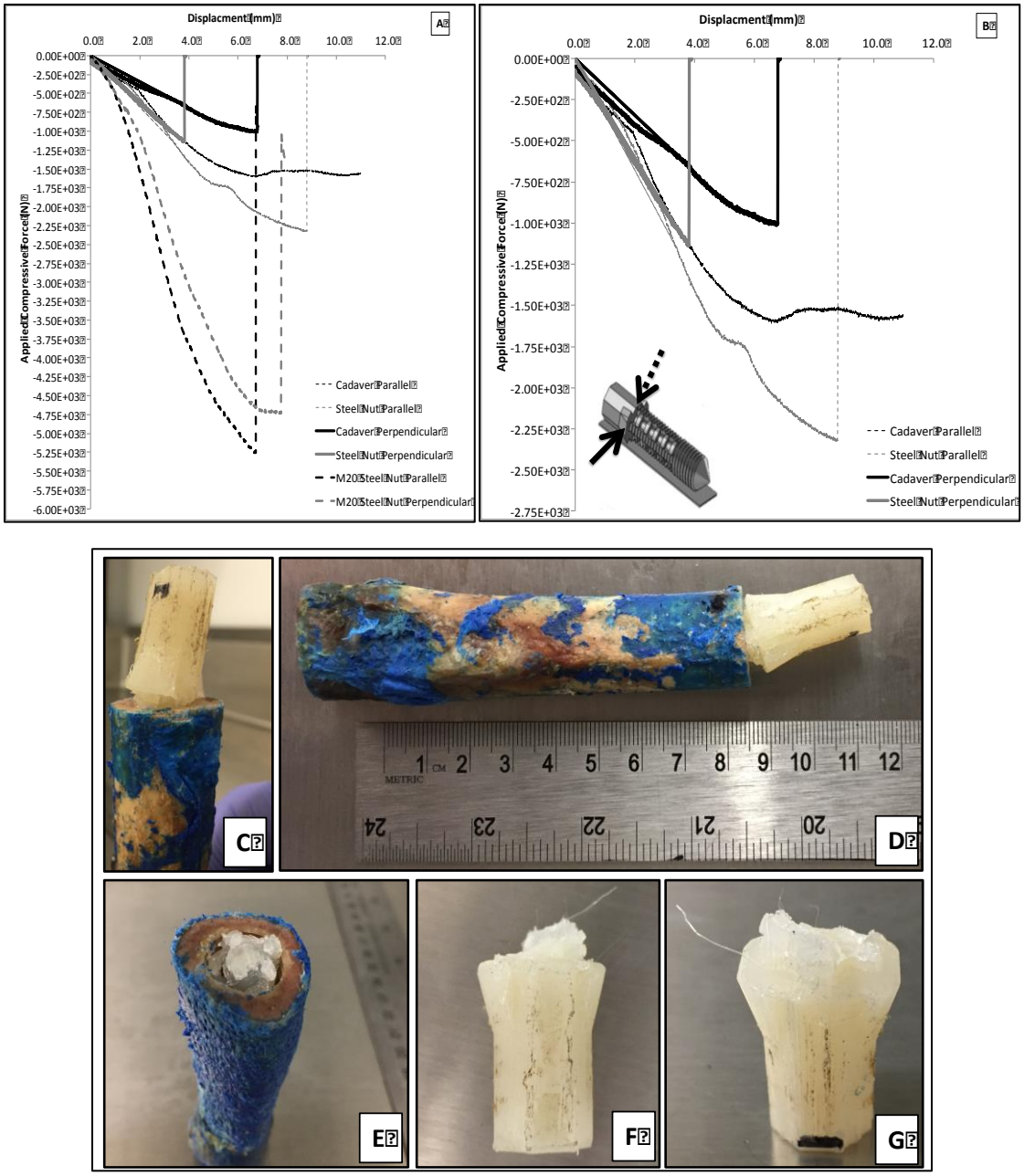

Figure 8. Three-point bending results. (Image A) Shows the M14 cadaver and simulated data versus the original M20 simulated data. (Image B) Shows the M14 cadaver and simulated data only. (Images C-D) Cadaver three-point bending Parallel failure sample. (Images E-G) Cadaver three-point bending Perpendicular failure sample. (Image B) Parallel (solid arrow on subset schematic in top right graph) represents the increase cross-sectional area and Perpendicular (dashed arrow on subset schematic in top right graph) is the smaller cross-sectional area.

	M14 K2.0mm				M20 K2.5mm	
	Steel Nut Perpendicular	Steel Nut Parallel	Cadaver Perpendicular	Cadaver Parallel	Steel Nut Parallel	Steel Nut Perpendicular
Max Displacement (mm)	3.8947606	8.8763523	6.8672595	10.988303	6.8295454	7.89580793
Max Force (kN)	1.139973	2.3259392	1.0151346	1.6097603	5.2596453	4.7372942

Change from Steel Nut to Cadaver	**Perpendicular**		**Parallel**	
Max Displacement Increase % (mm)	43.28508192	Increased from Steel to Cadaver	19.21998966	Increased from Steel to Cadaver
Max Force % (kN)	-12.29771894	Decreased from Steel to Cadaver	-44.48978522	Decreased from Steel to Cadaver
From M14 to M20	**Perpendicular**		**Parallel**	
Max Displacement Increase % (mm)	50.67305798	Increased from M14 to M20	-29.96988496	Decreased from M14 to M20
Max Force % (kN)	75.93620004	Increased from M14 to M20	55.77764151	Increased from M14 to M20

Table 3. (TOP) Represents the maximum displacement and force values for the M14 and M20 tests. (BOTTOM) Represents the differences from the M20 to the M14 and the cadaver to the simulated steel nut samples.

When evaluating the maximum data values out to the forces and moment arms seen in the referenced paper[54] used for the original screw design, the M14 printed screw would only be able to hold 50.11% and 34.68% of the load as the synthetic humeri compared to the simulated and cadaver environments respectively. Additionally, the screw would be able to hold 43.23% more of load compared to the cadaver reference paper values in our simulated steel environment and have nearly identical bending moment values with our cadaver environment results being able to hold 99.13% of the applied load seen in the reference data. The cadaver and synthetic humeri bones in the reference paper have bending moments of 36.7Nm and 104.9Nm respectively.

For the originally designed M20 FFF 3D printed screw, it had a bending stiffness (K) of 769.26N/mm within the simulated environment at a maximum displacement of 6.83mm, and a bending moment (M) of 118,793.74Nmm (118.79Nm) to screw head (M_h)

and 199,741.69Nmm (199.74Nm) to steel nut contact (M_n). Extrapolating this data out to the forces seen in the referenced paper[54], the printed screw would be able to hold 12.14% more load at the same moment distance as the synthetic humeri and 69.11% more load at the same moment distance as the cadaver humeri.

The original M20 screw was designed to meet the average force seen at the wrist of 500.00lbs or 2.20kN at an average fall height and up to a maximum value of just over 900.00lbs or 4.00kN seen at a fall height of six meters[55]. The force seen at the wrist was chosen since it sees the greatest force during a fall. The shoulder and elbow see less of a force because they have the degree(s) of freedom to displace during a fall and decrease the force seen at that joint and subsequent body parts around them. Where the wrist makes a hard contact with the ground during a fall and provides no deflection on contact with a surface. When looking at the maximum bending forces, figure 8 and table 3, we can see that the M20 screw can withstand the forces seen during a fall in either the simulated environment or even when applying the 12.29% decrease seen in the change from a steel nut to the cadaver sample from the M14 screw. While the M14 screw cannot withstand the average or maximum fall forces in either the simulated or cadaver environment; the M14 screw could only withstand the average fall forces seen while in the parallel test orientation.

With the M14 FFF 3D printed screws, it would be recommended that they be used for children or smaller individuals where their mass during a fall would have less impact. The children in this case could go through two surgeries in their lifetime to allow them to

grow into the larger diameter screw if necessary. Allowing children to have an osseointegration screw for prosthetic attachment will increase their performance and use of a prosthetic. The osseointegration screw will increase performance since it is attached directly to the skeletal bone system, providing increased sensation and fixation, and allow the children to have more time with their prosthetic. This increase in time will allow them to adjust and modify their environment to work successfully with their prosthetic, therefore decreasing prosthetic abandonment. Where the reference values from above[55] use individuals with body masses of 51kg (112.43lbs) to 83kg (182.98lbs) and heights of 1.52m (59.8inches) to 1.78m (70.07inches).

Lastly, M14 screw samples that were tested in the parallel orientation had larger displacement values compared to their perpendicular orientation and the parallel orientation for the M20 sample due to the increase in flexibility caused by the change in length to diameter ratio. Since the overall screw lengths were kept the same and the outer diameter changing from 20mm to 14mm, the flexibility increased as the diameter decreased.

For the torsion testing, torque-to-failure with initial creep tests were performed to demonstrate the storage of linear tension generated by torsion and the maximum seating torque in the cadaver sample. Figure 9 shows the seating and break-off torques and torque-to-failure values for the cadaver and simulated environment. The FFF osseointegrated screw was seated to 3.00Nm, given five minutes to settle, then loosened to remove tension, and then repeated two more times. After performing the creep tests,

the sample was taken to failure. Trials numbers 1 and 3 of the cadaver testing were seated to 3.2Nm instead of 3.0Nm.

The seating torque value needed to fall between 4.00Nm and 0.50Nm, representing a secure and loose-fitting implant for insertion[56]. These seating values represent osseointegrated titanium prosthesis used for femur attachment. Femur attachments require higher strength and seating values than humeri attachment, therefore using these as a requirement gives the screw design presented here a safety factor. From the results, we can see the break-off torque values, trials 1-3, and torque-to-failure values for the cadaver and simulated steel nut samples. The data shows that the screw can be seated to well past what is considered a tight-fitting prosthetic, failure torque of 8.1Nm and 6.8Nm for the cadaver and steel sample, and shows an average torque settling of 22.2% and 16.67% for the cadaver and simulate steel nut samples.

FFF 3D PRINTED MECHANICAL PERFORMANCE PTIFALLS/DISADVANTAGES

Future work to evaluate the mechanical properties of the osseointegration screw are to test it with dynamic forces. The mechanical testing presented above uses a slow input load from the Instron. To better evaluate this device, dynamic forces, i.e. dropping or high impacts, would need to be applied to test the screws durability. Since the slow input loads provide the maximum force the system can withstand, a dynamic load would allow the elastic or energy absorbing properties to be better evaluated. A sudden fall or contact with a hard surface is something anyone can inflected on them, therefore future work is needed to test the durability of this design.

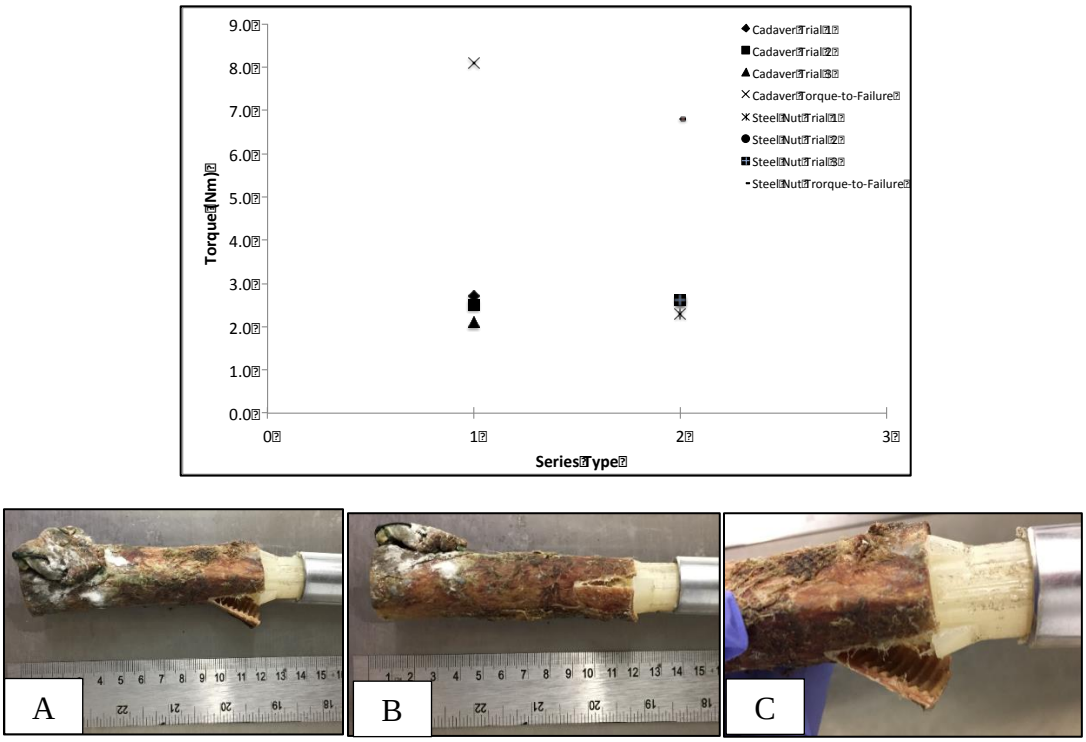

Figure 9. (TOP) Torque to failure and creep testing. Series 1 is the cadaver sample and series 2 is the simulated steel nut sample. (BOTTOM) Peak torque was observed when cadaver sample failed (A, B, C) not osseointegration screw.

FFF 3D PRINTED POLYMER LEACHING AND CYTOTOXICITY TESTING

48 hours after inoculation, the wells were imaged to look for visible indicators of cell death. In figure 10 we can see that the control group, which contained the control medium and osteo cells, and the test group, which contained test medium and osteo cells, had similar morphologies and levels of cell adhesion. The images show that there is little to no increase in cell death compared to the control groups across the entire well. If cell death were to be present, there would be large voids/blank areas in the well were the dead cell became detached from the well bottom.

After imaging, the medium and cells were removed from each well, placed in a test tube, re-suspended, and a green fluorescence dye (SYTOX) was used to stain the samples. The fluorescent dye does not diffuse across intact membranes of viable cells. Therefore, the dye only concentrates within dead cells with permeable membranes. From here, the samples were taken over to the flow cytometry machine to record the fluorescence intensity. The machine is able to detect forward and side scatter, allowing it to detect cells that are in different orientations during testing, see figure 10.

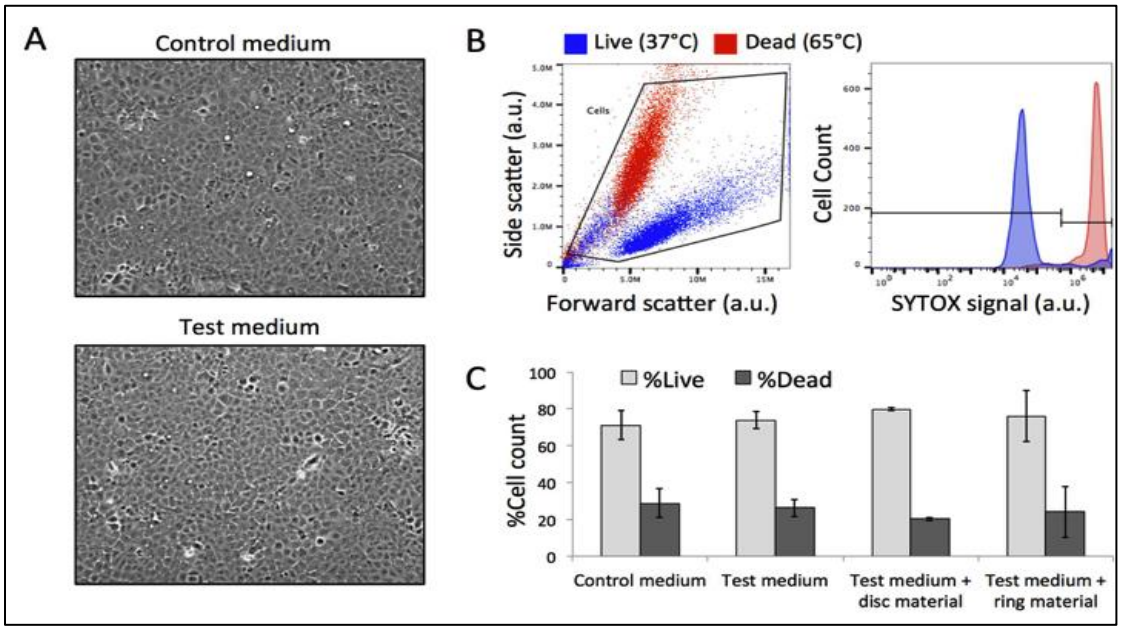

Figure 10. Determination of the cytotoxicity of compounds leached from the 3D printed material into cell growth media. (A) Phase contrast images (100x magnification) of live U-2 OS cells after 48 hours of growth in standard medium or test (treated) medium. (B) Flow cytometry analysis of control cells or cells killed with a high-temperature incubation. The scatter plot shows forward versus side scatter for ~10,000 cells (per sample). The gate excludes non-cellular particles. Histograms show SYTOX fluorescence signal of cells within the gate from the scatter plot. (C) The bar chart shows average proportions of live and dead cells (~5,000 per sample) determined by the SYTOX signal threshold (bar gates in B). Error bars = standard deviation of means for n = 3 (test medium) or n = 2 (all others).

Using live cells and dead cells to determine the SYTOX frequency range first was needed as the control for determining the cell count for future tests. Live cells used were kept at 37^0C while dead cells were fabricated by incubating the cells at 65^0C to kill them. Once the control cell count was performed, the control medium and test medium samples were tested. The average control medium and test medium samples show little difference in live and dead cell counts, with similar error bars. This demonstrates that the FFF 3D printed polymer has no significant impact or any toxic leaching that would cause death to the osteo cells.

The osteo cell line was chosen since the osseointegration device comes into the greatest contact with skeletal bone cells, followed by skeletal muscle and skin cells. Since the device is expected to create a fixation point within the bone, the osteo cell testing was needed as the first step in determining that the device would not be rejected and be able to generate the fixation point.

Since this study was limited to the osteo cell line, future toxicity testing involves testing with skeletal muscle and skin cells. The skin cell testing will be needed because the abutment protrudes out through the skin and the muscle cells are needed since the abutment makes contact with those cells once outside the bone. Skin helps prevent infection in the body by creating a barrier between the body and outside environment, therefore these cells will need to be tested in the future.

The polymer incubation in PBS solution tests showed positive initial results, figure 11 and 12A. The minimal change in data around the 200-300nm wavelengths is caused by hydrolysis of the polyamide polymer. The chemicals that seem to be leaching between 200-300nm are ε-caprolactam, adipic acid, and hexamethylenediamine or another linear aliphatic diamine[57,58, 59, 60]. Since the data around 200-300nm does not change as drastically as seen at 900-1000nm, along with the minimal loss in mass, the lower wavelengths appear to not be as invasive as the substance causing the optical change at the higher wavelengths. This substance is seen in the PBS and DI water samples, demonstrating the change in optical density at 970nm is due to the presence of DI water.

The polymer had a mass loss of 6.67mg, 0.415% of overall mass, caused by hydrolysis, where the polymer had an overall mass increase of 9.69% due to the absorption of DI water during incubation. The loss of mass was determined by dissolving a polymer sample in a toluene solution and then measuring the optical density with fluorescence absorbance and 250μL of each solution into a 96 well plate, figure 12B. The solution was heated at 150.0^0C for 48hours, with 11.5mg of the polymer in powder form with 1000.0mg of toluene. From here, using the density of 1.0715g/mL, the results were used to calibrate the incubation test curve at 864hours and determine the mass loss from hydrolysis. The polymer in the toluene solution had an optical density change of 0.12 from neat toluene, which when compared to the optical density of 0.07 for the 864hours incubation study results in a mass loss of 6.67mg, figure 12C.

The increase in optical density from 200-300nm is seen after incubating for 336hrs or longer, indicating that the change is not due to drastic polymer breakdown/leaching. Where at 192, 144, 96, and 48hours showed no change from the baseline PBS solution indicating that during the cytotoxicity testing no additional chemicals were leached into the mediums. Additionally, the pH level did not alter after the polymer was incubated and stayed at a constant pH level 7.4 or neutral. The polyamide 6 based material does have strong inter-chain interactions caused by the hydrogen bonds between molecular chains of polyamide 6 allowing it to be resistant to leaching[61], but due to the hydrolysis experienced by the polymer here, it is recommended to use a polyamide polymer that has longer chain lengths. Longer chain lengths include polyamide 10, 11, 12, which are still a thermoplastic and have higher mechanical properties then polyamide 6 materials. This will allow the device to still be manufactured on a FFF 3D printer while having a stronger resistance to hydrolysis and stronger mechanical properties.

These two sets of testing show that the initial 48-hour cytotoxicity was positive but the PBS incubation study relives that the material may not be ideal for a long-term implant. Future testing involves determining the exact chemicals leaching into the solution by running a series of tests with various chemicals used to synthesize polyamide 6 based materials. Once the chemicals are identified, those chemicals will be tested for cytotoxicity to determine if they will have a negative impact on the human body. Additionally, polyamide 10-12 polymers will be tested for polymer leaching and compared to the polymer presented here to demonstrate the effect of hydrolysis on longer

chain length polyamides. Since the material tested here is a product provided by Taulman 3D, the exact molecular structure is protected and not made available. Therefore, the initial leaching study was needed to identify if any chemicals were leaching and what those chemicals could be.

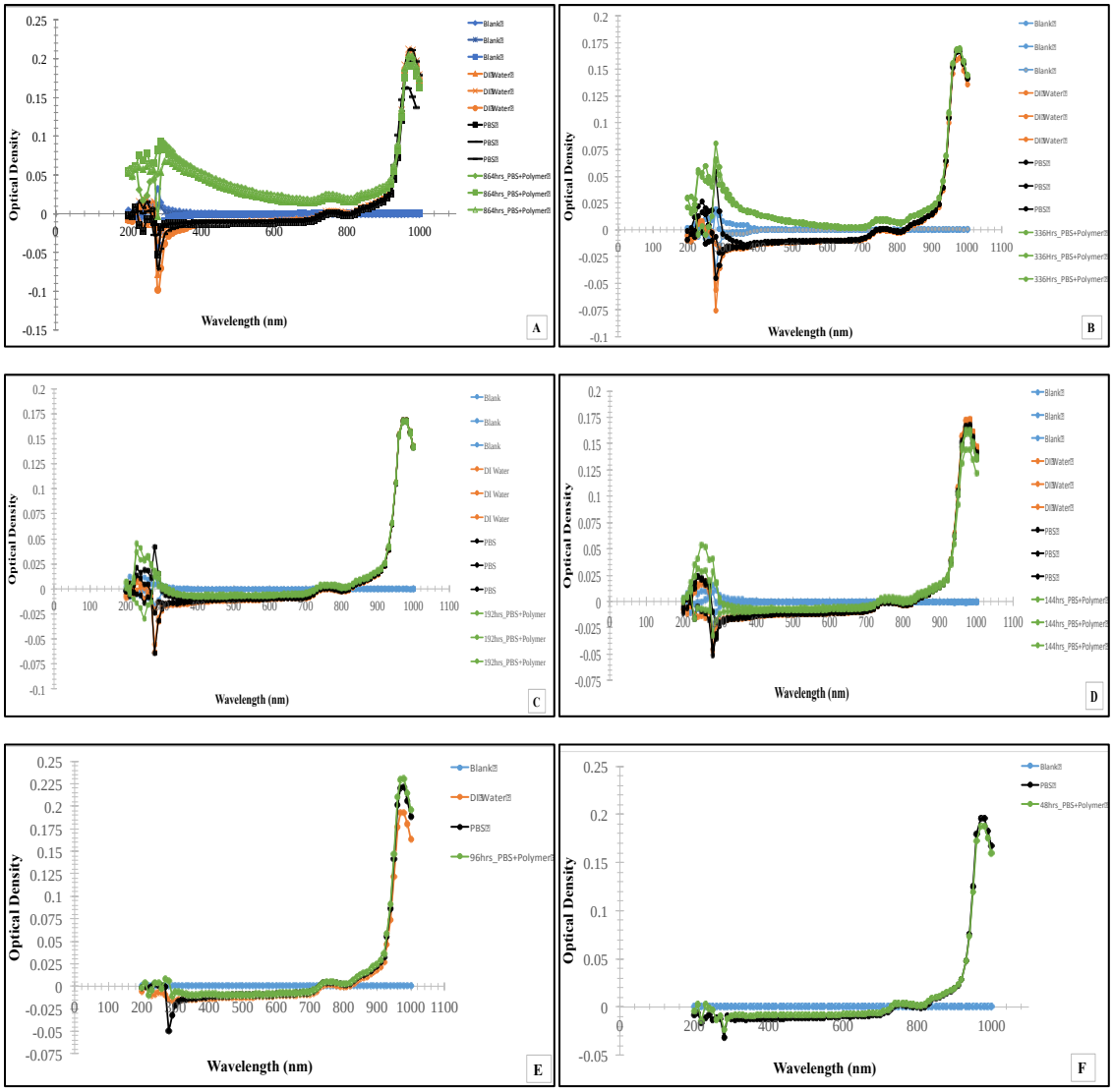

Figure 11. Polymer leeching study in a Phosphate Buffer Solution for 864hours. Image A shows the group data for incubation at 864hours with a sample size of N=3. Image B shows the group data for incubation at 336hours with a sample size of N=3. Image C shows the group data for incubation at 192hours with a sample size of N=3. Image D shows the group data for incubation at 144hours with a sample size of N=3. Image E shows the group data for incubation at 96hours with a sample size of N=1. Image F shows the group data for incubation at 48hours with a sample size of N=1.

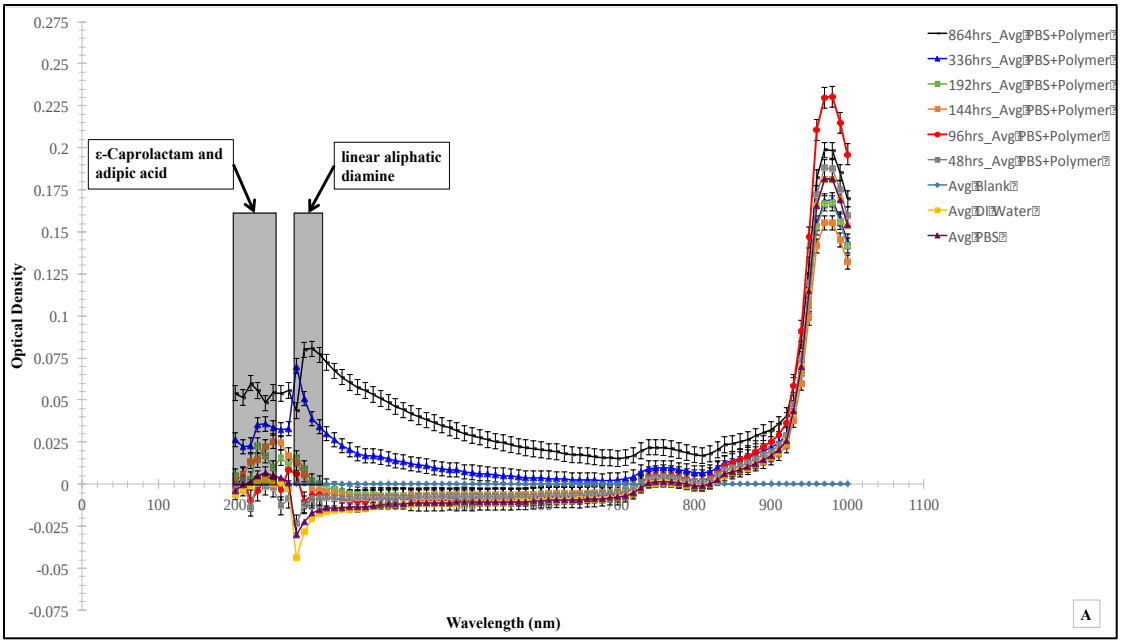

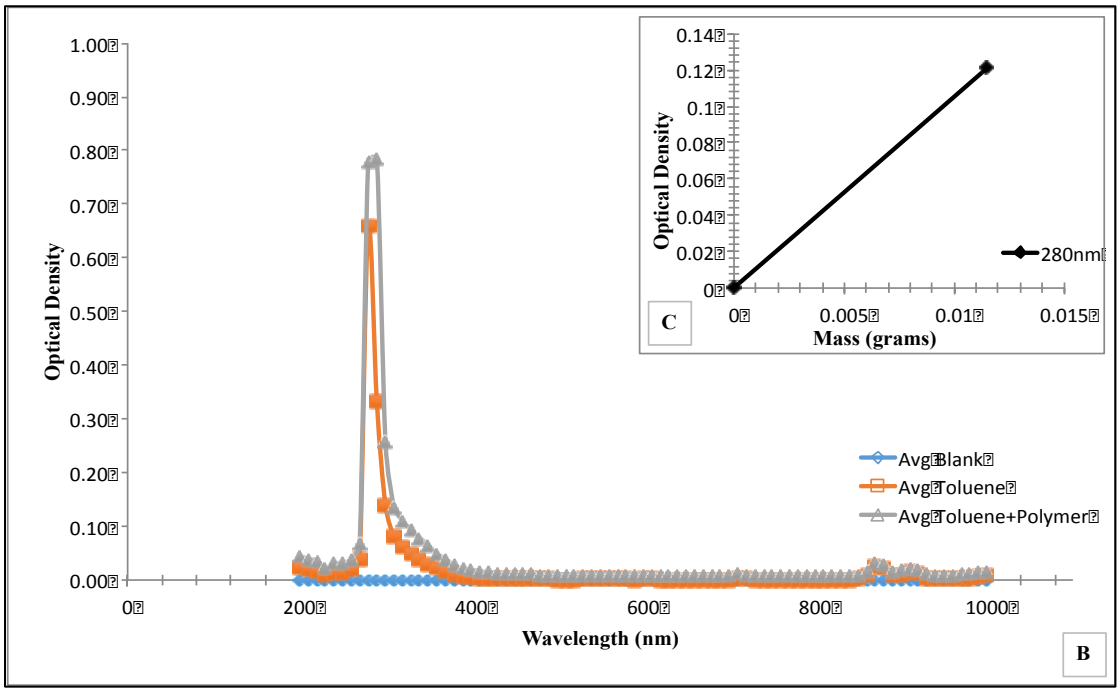

Figure 12. Polymer leeching study in a Phosphate Buffer Solution for 864hours and loss of mass from hydrolysis, all sample types had a sample size of N=3. Image A shows the average of each incubation period results with the error bars representing the standard deviation for each incubation period. Image B shows the dissolved powder polymer in toluene versus neat toluene to determine the impact of chemical leaching in to the solution. Image C shows the optical density with 11.5mg of powdered polymer dissolved in toluene at 280nm wavelength.

CONCLUSION

Here we present the continuation of our research into the biocompatibility and fixation strength of the FFF 3D printed trans-humeral osseointegration screw. The testing shows that there is minimal change in torsion values when going from a simulated to cadaver environment. Additionally, the maximum bending force decreased 12.29% and the maximum displacement increased 43.28% when going from the simulated to cadaver environment. The results also show that the smaller M14 screw is not suitable for adults with body masses between 51-83kg and heights between 1.52-1.78m, but may be suitable for children or small adults.

It was also observed that the polymer, after it was 3D printed, showed no effect on the health of the human osteo cells during the 48-hour cytotoxicity test. Imaging results showed no change in living cells when comparing the cells placed in either the control or test medium. There was observed cell death in the wells were the 3D printed discs were placed to due mechanical abrasion against the cells. The flow cytometry results showed no changes in cell count live versus dead trends when comparing the test medium to control medium samples.

The PBS incubation testing showed that up to 192hours there was no change in optical density, indicating that for the cytotoxicity testing there were no additional substances released from the FFF 3D polymer. The pH level also stayed the same after 864hours of incubation demonstrating that the polymer does not affect the solutions acidity level. While at 864hour of incubation there are some changes in optical density,

caused by hydrolysis, around 200-300nm wavelengths that appear to be due to minimal leaching of ε-Caprolactam, adipic acid, and hexamethylenediamine or another linear aliphatic diamine, where further testing is needed to determine the exact leaching chemicals. Additionally, there was a small mass loss due to the hydrolysis of the polyamide 6 based polymer of 6.67mg, 0.415% of overall mass.

The minimal decrease in fixation strength from a simulated to cadaver environment along with the cytotoxicity and PBS incubation studies demonstrate that the proposed device shows initial positive results for a long-term implant and stable fixation system for upper limb prosthetics. Future directions are to determine the exact chemicals that are leaching into the PBS solution and performing cytotoxicity on each chemical to determine if it is harmful to human bone, muscle, and skin cells. Additionally, polyamide 10,11, and 12 polymers will be obtained and incubated in a PBS solution for 36days to determine if theses polymers have any chemical leaching.

ACKNOWLEDGMENT

We would like to thank the Musculoskeletal Orthopedic Research and Education (MORE) Foundation for the donation of the cadaver humeri samples, and Dr. Karmella A. Haynes and David Nyer for the data presented in figure 10 of the supplemental data. The support and donation has helped us greatly advance our research and Fused Filament Fabrication devices.

CHAPTER FIVE: FUSED FILAMENT FABRICATION 3D PRINTED PRESSURE SENSOR FOR PROSTHETICS WITH LOW ELASTIC MODULUS AND HIGH FILLER RATIO FILAMENT COMPOSITES.

INTRODUCTION

To overcome the pitfalls of strain gage and thick/thin film tactile sensors for prosthetics, a Fused Filament Fabrication (FFF) 3D printed piezo-resistive pressure and shear sensor for daily activity sensing was developed. The 3D printed tactile sensor will be manufactured out of a composite comprising of a low elastic modulus compressible thermoplastic elastomer, and carbon, in graphite form, as the conductive material in high filler amounts.

The sensor is: mechanically compressible to allow for a change in resistance, 3D printed in one step with no post-processing needed, flexible, has a rubber finish that allows it to be similar to human skin, can be customized to various designs to match the user's need, and has a thickness within the average human skin thickness[76, 77]

MATERIALS AND METHODS

All parts were printed on a MakerGear M2 with Simplify3D software, and tested on an MTS Model Sintech 1/S tensile machine (maximum load cell capability of 1,000lbs) and CH Instrument for measuring changes in current. Two types of sensors were created for this paper; one using gravity molds for baseline testing and then 3D printed sensors. 3D printed sensors were made using SOLIDWORKS 3D CAD software and pellets of the composite fed through a filament extruder to create a 1.75mm diameter filament for 3D printing.

Poly-Styrene Ethylene Butylene Styrene (SEBS), the compressible thermoplastic elastomer, was chosen due to its synthetic skin feel, compressibility, and easy application in injection molding. Since FFF 3D printing has a close relationship to injection molding, it provided an addition benefit along with its tactile feel and synthetic skin applications.

The composite was created by first dissolving SEBS pellets in toluene, with a 1.2:1 ratio of toluene to SEBS, to break it down to a gel-like state since SEBS is a difficult polymer to get in to a flow-able state without being injection molded. In order to incorporate the conductive material into the polymer, the material needed to be in a state where it could be stirred. To accomplish this, the toluene was added to the SEBS pellets add left for 24 hours at room temperature to dissolve the polymer.

Once in a liquid/gel-like state, the conductive material graphite was added to the mixture. Multiple iterations were created to show which composites are conductive and how it changes as the ratio increases. Additionally, we demonstrate how to FFF 3D print with materials with low elastic modulus and high filler ratios. With the density of SEBS and graphite being $0.85 g/cm^3$ and $2.25 g/cm^3$ respectively.

The mixture was then thoroughly stirred until the carbon had fully dispersed within the polymer and toluene solution. From here the mixture was placed in a gravity fed mold and allowed to sit for 24 to 48 hours until the toluene had evaporated out of the

mixture. Toluene was chosen for this reason since it is highly evaporative at room temperature and pressure.

When the toluene evaporates out of the mixture, it leaves only the carbon distributed within the SEBS polymer, see figure 13. The distributed particles can now be compressed when a pressure is applied and bring them closer together. This allows for a change in resistance to take place due to the decrease in space between the conductive particles.

After the toluene has evaporated out, the composite is removed from the mold and cut in to 12mmx12mm square samples with a thickness of 2.54 mm for testing. This same process was done for creating the pellets for the filament for 3D printing. The pellets were fed in to a filament extruder at 95-100°C to create the 1.75mm diameter. The filament was fed through the FFF 3D printer with the settings in table 4 and was fabricated in to the sample size as stated above. The quality of the filament post extrusion shows no breaks or tears in the filament. Additionally, the filament has a consistent diameter along the entire length of filament with only a 0.05mm difference in between the 1:1 and 1.33:1 sensor filaments.

Filament strands were tested under tension to demonstrate the composite's low elastic modulus, see figure 14 for results. To determine the optimal applied voltage, cyclic voltammetry (CV) was performed on a molded sample with no applied pressure,

see figure 14 for results. From here, the determined applied voltage of -0.2 volts was used with calibrated masses for testing the molded and 3D printed samples.

FFF 3D Printer Settings	
Extruder Nozzle Temperature	250°C
Bed Temperature	100°C with Kapton tape
Layer Height	0.6mm
Extruder Speed	100mm/minute
Extruder Nozzle Diameter	1.58mm
Extrusion Multiplier	0.9
Extrusion Width	1.9mm
Layer Settings	7 shells with 3 on top and 2 on bottom

Table 4. Software and printer settings for MakerGear M2 3D printer.

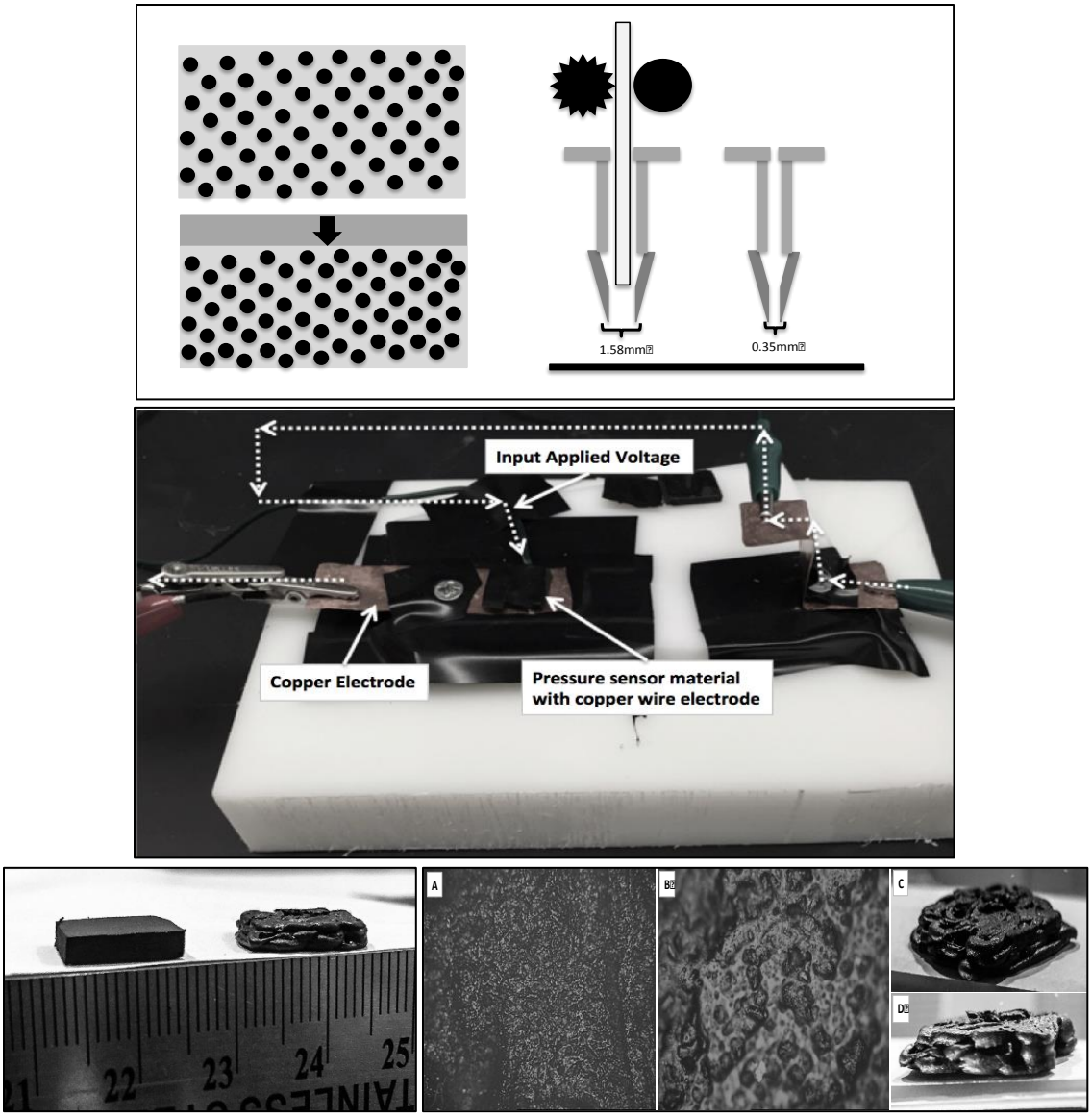

Figure 13. (Top) image represents the compression of conductive particles causing a change in resistance and the enlarged nozzle and heating chamber compared to original nozzle and heating chamber diameter. (Center) image is the pressure sensor test fixture with dotted white arrows indicating applied voltage direction. (Bottom) Left image shows the molded/non-printed sensor design on the left and the FFF 3D printed sensor design with a centimeter scale across bottom. Right image shows sensor surface images with 100x (A) and 200x (B) magnification and side profiles (C and D) of the 3D printed sensor.

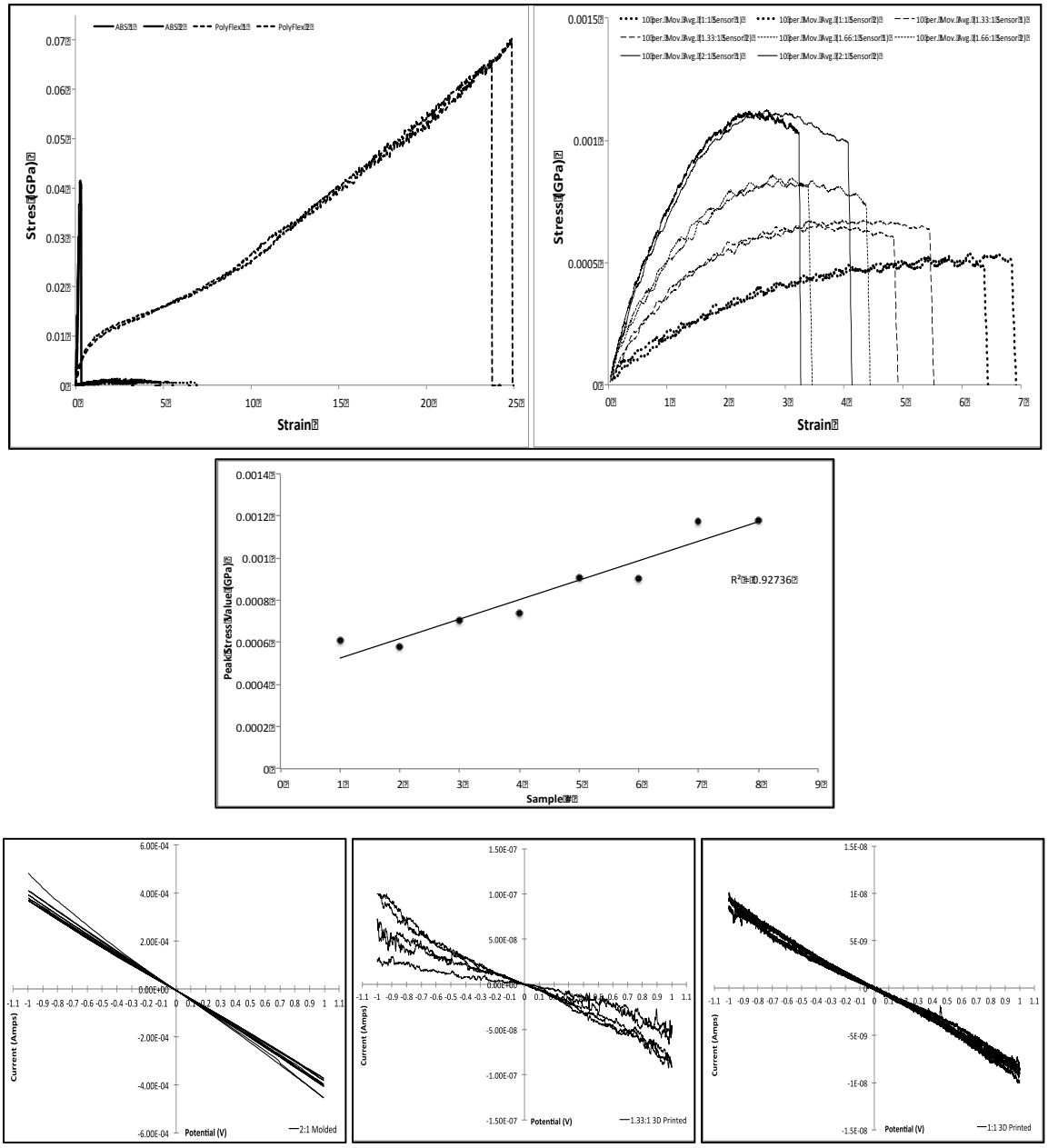

Figure 14. Top row left graph shows tensile testing of sensor composites, ABS, and PolyFlex filament (ABS is sharp solid line curves, PolyFlex is dashed line curves, and the composites are the bottom cluster of curves). Top row right graph shows a zoomed version of the sensor composite filaments only. Sensor composite filaments are plotted with a moving average with the top two runs being the 2:1 ratio down to the 1:1 ratio runs at the bottom.Center row graph shows the maximum tensile strength vs sample number. The sample numbers 1-8 represent the four different filament ratios and the two samples in each filament type. Bottom row from left to right shows Cyclic Voltammetry (CV) curve of an unloaded molded pressure sensor, 1.33:1 sensor ratio, and 1:1 sensor ratio to determine optimal applied voltage.

RESULTS

Tensile testing had a sample size of N=2 to categorize the elasticity of the composites and compare it to two established 3D printing filaments, one being ABS while the other being PolyFlex, which is a flexible, large strain material. After characterizing the multiple moduli and ideal applied voltage, the different samples were tested with masses ranging from 0.25 grams to 750 grams, with masses having an variation of ±0.00019%. The various composite mass-to-mass ratios used were 0.75-2.00:1.00 to demonstrate the lower limit of a conducting material to the upper limit of which ratios can be fabricated, FFF 3D printed, and the lower limit of pressure detection.

Printed samples were printed longitudinally or perpendicular to direction of applied compression to provide the greatest strength since printing parallel to the direction of applied compression would result in a weaker part due to the layer adhesion strength of FFF parts, this effect has been seen here[78].

All pressure testing samples were placed on to the custom test fixture with a copper plate on the bottom, acting as the bottom electrode, and a copper wire placed on top of the sample with vinyl insulating tape to prevent any electrical interferences with the copper wire and the brass weights, see figure 13. The copper wire in our test setup carries the applied voltage and the copper plate carries the output signal to the CH Instrument.

Where the shear force testing samples were performed on the same test fixture described above but used a glass plate with a wire and pulley system while fixing the bottom half of the sensor from moving to generate a shear force. The glass plate, which contacted the entire surface, was placed on top of the sensor with a wire attached to it. The wire was then straightened and redirected to point perpendicular or vertical to the glass plate surface. The redirect, along with fixing half the sensor's thickness, allows the weights to generate a shear force across the sensor's surface. For shear force testing, only the 1:1 and 1.33:1 ratio 3D printed sensors were evaluated.

The testing showed that the lowest composite mixture of 0.75:1 ratio of graphite to SEBS to not be conductive under any pressure or applied voltage, while the 1.00-2.00:1 ratios were. Additionally, the only samples that could be FFF 3D printed were the 1:1 and 1.33:1 mixtures, the 0.75:1 mixture could have been 3D printed but was not since it proved to not be conductive. Composites with a ratio of 1.66:1 or 2:1 were not able to be FFF 3D printed due to the lack of thermoplastic matrix.

In order for the samples to be 3D printed, the extruder nozzle and heating chamber diameter needed to be increased from the standard 0.35mm to a large 1.58mm diameter for both 1:1 and 1.33:1 sensor ratios. This large diameter in tandem with the 1.75mm diameter filament results in very little backpressure to the feeder gear and using almost solely radiating heat to make the composite filament in a flowable state. This style of printing is different from the standard FFF 3D printing technique where temperature and pressure are used to make the filament flowable for extrusion[79,80,81].

The pressure sensors were designed to meet the demands of daily activities or be designed into a two-part system, where two different composite mixtures would be used to create an overall sensor design that could accommodate the feedback needed for daily activities. The pressure sensors presented here are capable of achieving values as low as 17.03Pa and up to 51.09kPa, with the pressures seen during daily activities being 10kPa and a light touch being 100Pa.

The FFF 3D printed sensors are able to detect between 340.63Pa and 51.09kPa and the molded sensors able to detect between 17.03Pa and 47.69kPa for pressure. Where the shear sensors are able to detect between 34.06Pa and 340.63Pa (0.5g and 5.0g). Since the molded sensors can have a higher percentage of conductive material to polymer matrix, they are able to have a greater sensitivity to changes in pressure, where the 3D printed sensors need to have a greater percentage of polymer matrix in order to be FFF 3D printed. The molded samples are still able to be an advanced manufactured pressure sensor since they can be molded in to a variety of 3D printed molds to create point-of-care and embedded pressure sensors for prosthetics or other medical devices.

DISCUSSION

MATERIAL CHARACTERIZATION

The results from the tensile and CV testing show that the sensors have a low elastic modulus and an operating voltage of -0.2V. This shows how flexible the sensor is,

across multiple composite ratios, and that it requires a low operating voltage making it safe for use with prosthetics and interfacing with objects.

Tensile testing used fixtures where the filament wrapped around a top and bottom barrel and was fixed in placed leaving a precise gage length for testing. Samples were pulled at a strain rate of 500mm/min, following the ASTM D638 standard. 500mm/min was chosen over 5 or 50mm/min because the high strain rate places more emphasis on the elastic region of the composite rather than the energy dampening effect of composite.

From the results, we can see that with the increase in filler mass or volume, the ultimate tensile strength and elastic modulus increases from $1.83x10^{-4}$GPa for a 1:1 ratio to $6.01x10^{-4}$GPa for a 2:1 ratio, with 1.33:1 and 1.66:1 having a modulus of $3.17\ x10^{-4}$GPa and $4.64\ x10^{-4}$GPa respectively. Where the increase in mechanical reinforcements to a matrix increases the load absorbing properties by allowing a transfer of load to the higher strength material from the weaker matrix and decreases the mechanical strain a composite can withstand caused by the reinforcement material. The data is plotted with a 10-point moving average to remove noise from the data plots and shows a sample variance between the 1:1, 1.33:1, 1.66:1, and 2:1 filament ratios samples being 4.46%, 4.12%, 0.69%, and 0.84% respectfully. Additionally, plotting the maximum tensile strength vs sample number shows a R^2 of 0.927 demonstrating a high correlation and linear trend in the data, see figure 14. The sample numbers 1-8 represent the four different filament ratios and the two samples in each filament type. For example, samples 1, 2, and 3 are filament types 1:1, 1:1, and 1.33:1 respectively.

When comparing the composite modulus results to ABS or PolyFlex, which are 0.18GPa and 2.72 $x10^{-3}$GPa, we can see on figure 14 that the modulus, and additionally the maximum tensile strengths, of the composites are low are compared to these standard FFF 3D printing materials. This demonstrates that the sensor material is extremely weak with maximum tensile strengths between 0.00057GPa – 0.0011GPa. While ABS and PolyFlex have tensile strengths of 0.41GPa and 0.70GPa.

The second material characterization was the cyclic voltammetry (CV) testing to determine the ideal applied voltage level. This test was performed on a 12mmx12mmx2.54mm sample with a 2:1 composite ratio with no applied pressure to its surface.

The CV test is performed with a CH Instrument with five sweeps from -1.0V to 1.0V and measures the current output, where a sweep is from -1.0V to 1.0V. From here, the ideal voltage is selected by choosing the location where the greatest overlap of sweeps occurs. The ideal voltage chosen for the composite ratios was -0.2V. When reviewing figure 14, we can see that there is more scatter at the outer edges of the sweep pattern. If a voltage was chosen within the scatter areas, then it could induce noise into the pressure sensor data and cause an error in the recordings. Additionally, if a voltage is picked that is too close to 0.0 volts along the sweep pattern, then there will not be a large enough current amplitude offset from zero.

The same applied voltage was used for consistency across all data samples, except for the 1:1 3D printed samples due to fabrication techniques. If multiple composites were to be used in tandem to create a dual-purpose pressure sensor, then having one voltage for calibration would reduce the system complexity. The CV curves for the 3D printed samples show that there is greater variance and noise in the 3D printed samples compared to molded samples, which helps demonstrates that the FFF 3D printing process creates gaps/voids that increases the resistance and decreases the uniformity of the print. Lastly, the CV curve for the 1:1 3D printed samples shows that there is linearity at -0.2V but due to the extremely low current at -0.2V, the higher -0.5V is required to provide a greater pressure detection range.

FFF 3D PRINTED AND MOLDED PRESSURE SENSORS

After determining the applied constant voltage and characterizing the composites mechanical properties, the molded and 3D printed samples with ratios ranging from 0.75:1 to 2:1 were tested to determine the pressure range that each sensor type could record. The molded samples were formed in a cylindrical mold and cut in to the 12mmx12mmx2.54mm samples, while the 3D printed samples were printed with a layer height of 0.6mm and seven shells to print the 12mmx12mmx2.54mm sensor. A layer height of 0.6mm was the only successful printing layer since smaller layer heights caused large gaps to occur and a larger layer would cause the last layer to be drastically different from the lower layers. Once the samples were fabricated, the samples were placed on the pressure sensor fixture and calibrated masses were placed centered on top of the sensor, see figure 14.

The FFF 3D printed shape presented here, see figure 13, is the best quality that can be printed with current FFF technology. One of the main reasons is that when the filament is fed through the feeder gear and idler pulley the filament begins to slip and becomes stationary during extrusion, in turn causing no filament to be extruded. The slippage is caused by the extremely soft, flexible, low friction carbon filled filament, and the backpressure seen at the extrusion nozzle which causes the filament to slip or buckle in some situations.

To overcome this with current FFF feed system, the extrusion multiplier needs to be greater than one to keep up the filament extrusion with the slippage. The extrusion multiplier causes the rate of extrusion from the feeder gear to be larger than the predefined software feed rate. Due to this higher rate of extrusion, the filament can come out during non-slippage points in larger volumes, which causes lobes to be printed instead of continuing the fine line. The presented 3D printed sensors still provided accurate results based upon the slopes/trends and high correlation values shown in figure 16 of the 3D printed versus molded samples, and that the overall shape has little dimensional changes compared to the molded samples.

The printed sensors have an increased contact area of 5.4mm^2 and 0.4mm^2 for the 1:1 and 1.33:1 respectively, from the 150.2mm^2 baseline molded samples. This could theoretically cause an increase of 3.475% and 0.278% detectable pressure for the 1:1 and 1.33:1 3D printed sensors, but the trend in data shows that it has little impact in overall

performance. Additionally, the printed sensors are fabricated on a glass plate, which causes the bottom of the sensors to be completely flat and with no gaps in material. The copper electrode placed on top is also not a plate, like the bottom electrode, and is a copper wire that allows the wire to conform to the top of the sensor if necessary.
To resolve these issues, a new filament feed system would need to be developed and tested. The system would need to replace the feeder gear and idler pulley with a double-sided vertical rubber belt feed system that can increase contact area against the filament and support the filament in between the feeder system and heating nozzle to prevent slippage. Secondly, the distance between the feeder system and heating nozzle will need to be reduced to help prevent buckling within the feeder system. This will help provide a constant flow rate of filament and allow for the increased extrusion multiplier to go back to baseline.

Lastly, we performed multiple extrusions tests prior to final printing and found that only printing with the currently show printing parameters is successful. If the nozzle size is any smaller the filament will slip and buckle constantly causing no filament to extrude. The filament can only be consistently extruded at 267^0C, with a $\pm 2^0$C tolerance, since there is little polymer matrix left in the composite causing the filament to only be flowable/workable at a small window. Any higher temperatures cause the polymer to expand to rapidly which forces the carbon against the heating chamber wall and causes the filament to get stuck and break off. Additionally, extruding at lower temperatures does not make the filament extrude-able and simply passes through the extrusion nozzle

without becoming flowable. To ultimately overcome these issues, a new feeder system, described above, would need to be developed, fabricated, and tested.

Table 5 shows that minimum and maximum pressures each molded and printed sensor can detect along with the masses used to reach each pressure. From the table we can see that there is a difference in the maximum and minimum pressures detected based on the ratio used. There are large differences between the lower and high ratio composites where the 1:1 and 1.33:1 are able to detect higher pressures then the 1.66:1 and 2:1 sensor composites.

Within the molded samples, the higher ratio sensors are able to detect between 0.0170kPa - 20.4375kPa (0.25-300grams) where the lower 1.33:1 and 1:1 ratios are able to detect between 0.3406kPa - 20.4375kPa (5-300grams), and 2.0438kPa - 47.6875kPa (30-700grams), see figure 15. These sensors are able to detect a whole magnitude beneath a light touch on the human skin, and 370% over what is required for daily activities.

Within the 3D printed samples, there are only slight variations from the minimum and maximum force detections levels for the composites that are 3D printable to the molded samples. For the 3D printed samples, only 1:1 and 1.33:1 sensors are able to be 3D printed due to thermal expansion and the large volume fractions of conductive material within the matrix. The printed and molded pressure trends are compared in figure 16 along with the response times and slopes for each mass at each percentage of applied load to develop a predictive response time system.

The 1:1 pressure sensor is able to detect between 3.4063kPa - 51.0938kPa (50-750grams) and the 1.33:1 pressure sensor has the same range as its molded equivalence. Where the 1.33:1 shear sensor was the only detectable sensor and detected between 34.06Pa and 640.63Pa. The shear sensor was only characterized with the 3D printable sensors since the change in resistance magnitude was calibrated with the pressure sensor.

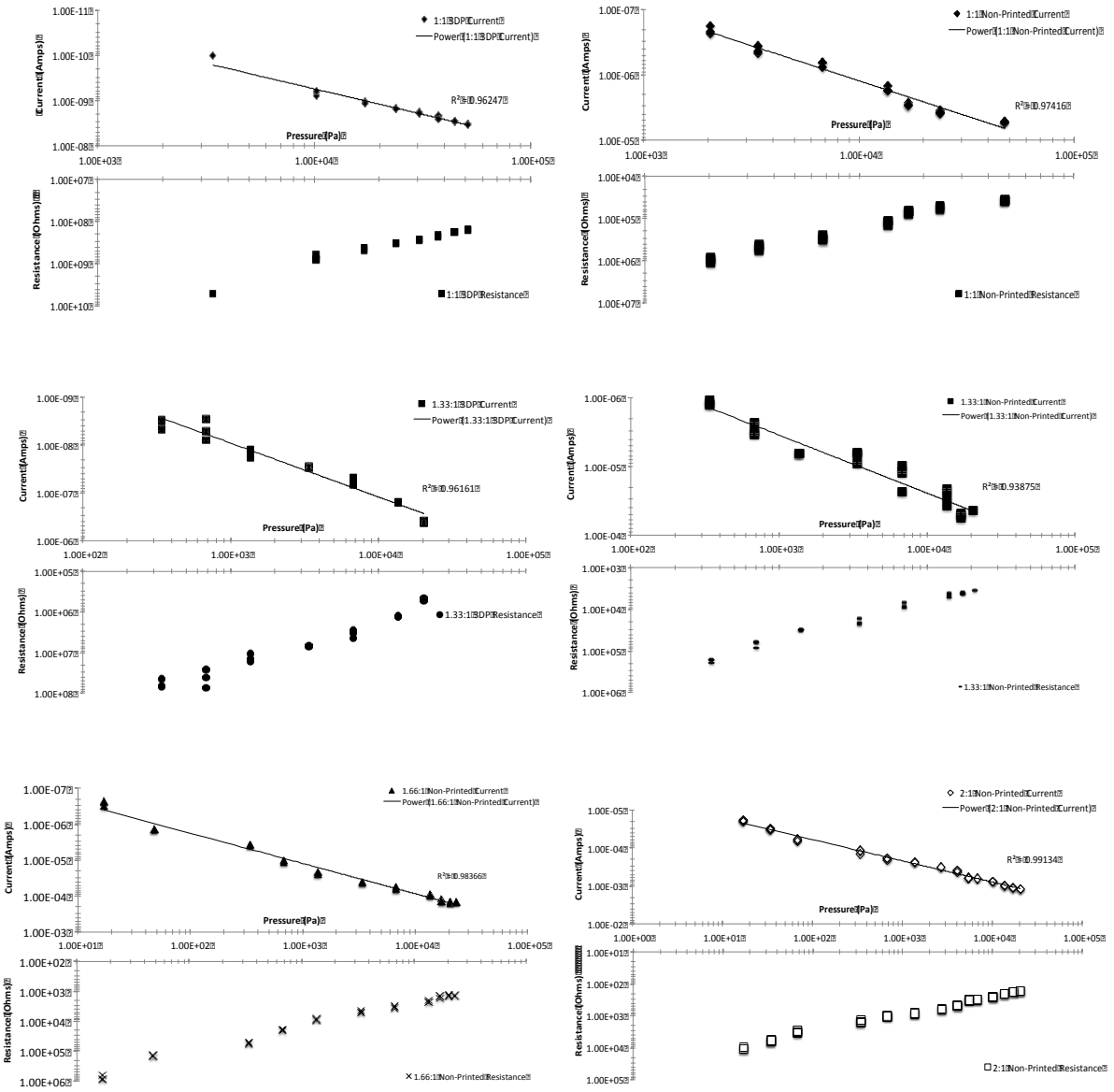

Figure 15. Pressure vs current and resistance data for FFF 3D printed and molded composite sensors from 1:1 to 2:1 ratios.

Sensor Type	Minimum Mass (Grams)	Maximum Mass (Grams)	Minimum Pressure (kPa)	Maximum Pressure (kPa)
Printed 1to1	50	750	3.4063	51.0938
1 to 1	30	700	2.0438	47.6875
Printed 1.33to1	5	300	0.3406	20.4375
1.33 to 1	5	300	0.3406	20.4375
1.66 to 1	0.25	300	0.0170	20.4375
2 to 1	0.25	300	0.0170	20.4375

Table 5. Minimum and maximum pressures that each sensor can detect along with the masses used to reach each pressure.

The reason for the change in detectable pressure range is that during the printing process there are gaps or spaces that occur between each layer causing a greater compression needed to compress the graphite particles closer to together to make an initial path for the current to travel across; this same affect is seen with the 1:1 to 1.33:1 shear sensor. Additionally, the conductive particles could be slightly rearranged during the printing fabrication and cause there to be gaps or voids within the composite causing a break in the current path. This needs to be studied in further detail to confirm our hypothesis, but for the printed 1:1 pressure and 1.33:1 shear sample, an applied voltage of -0.5V was needed for testing could point towards the addition of voids/spaces caused by FFF 3D printing.

The data for the pressure sensors are plotted on a $\log_{10}$ graph, figure 15, with resistance and current shown. The data follows a linear trend with high R^2 values with a

power analysis, $R^2 \geq 0.93$ for all samples. At each pressure value shown, a sample size of N=3 was used to show the variation in data with the same pressure applied. Additionally, the shear sensor is plotted on a figure 17, with resistance versus current. The shear sensor shows a power curve trend with a plateau at 340.63Pa (5.0g).

When the 3D printed sensors are compared to their molded equivalent, we can see that the samples follow similar trends differing only in their output current value, figure 16. Where the 3D printed samples are operating on an outputted current value four magnitudes lower than the molded samples, this holds true for the 1:1 and 1.33:1 sensors.

For the 3D printed pressure response times, the total response time to a complete steady state value is greater than five seconds due to the design requirements for a FFF 3D printed flexible, compressible, piezoresistive sensor. In order to have response times less than one second, commonly seen for mass production strain gage sensors at 90% of applied load, we need to use a predictive measuring system. Figure 16 shows the average slope versus the percentage of applied load, and the average time versus the percentage of applied load for the 1:1 and 1.33:1 sensors. For example, the percentage of the applied load implies that at 100% the sensor is at steady-state current levels for that mass.

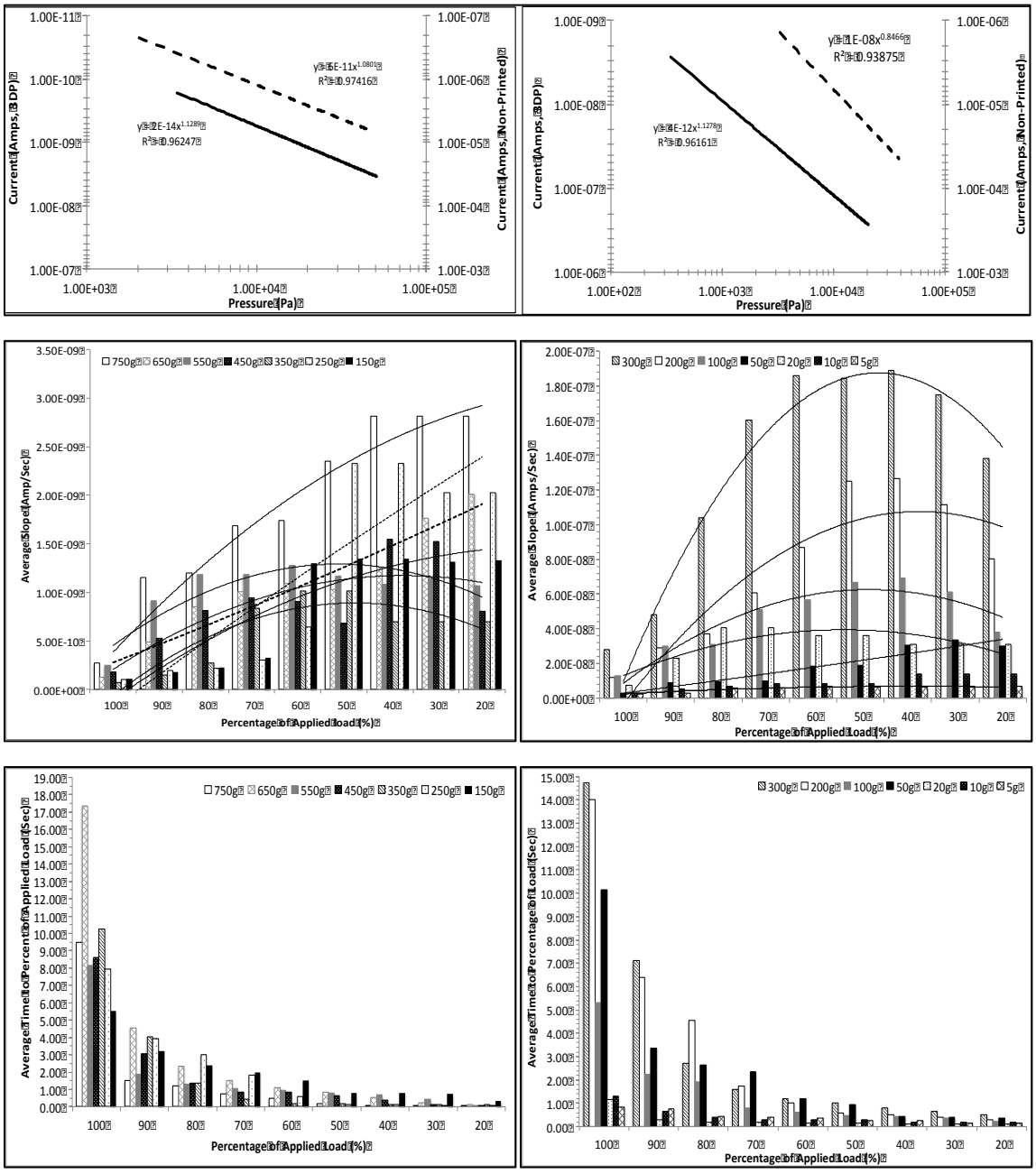

Figure 16. 1:1 ratios on LEFT and 1.33:1 ratios on RIGHT. Top row: Pressure vs Current fitted power lines of 3D printed (Solid Lines) and non-printed sensors (Dashed Lines) to demonstrate the similarity in data trend. FFF 3D printed samples have slight changes to their pressure detection ranges due to manufacturing fabrication. Center row: Average slope versus percentage of applied load. Bottom row: Average time to percentage of applied load.

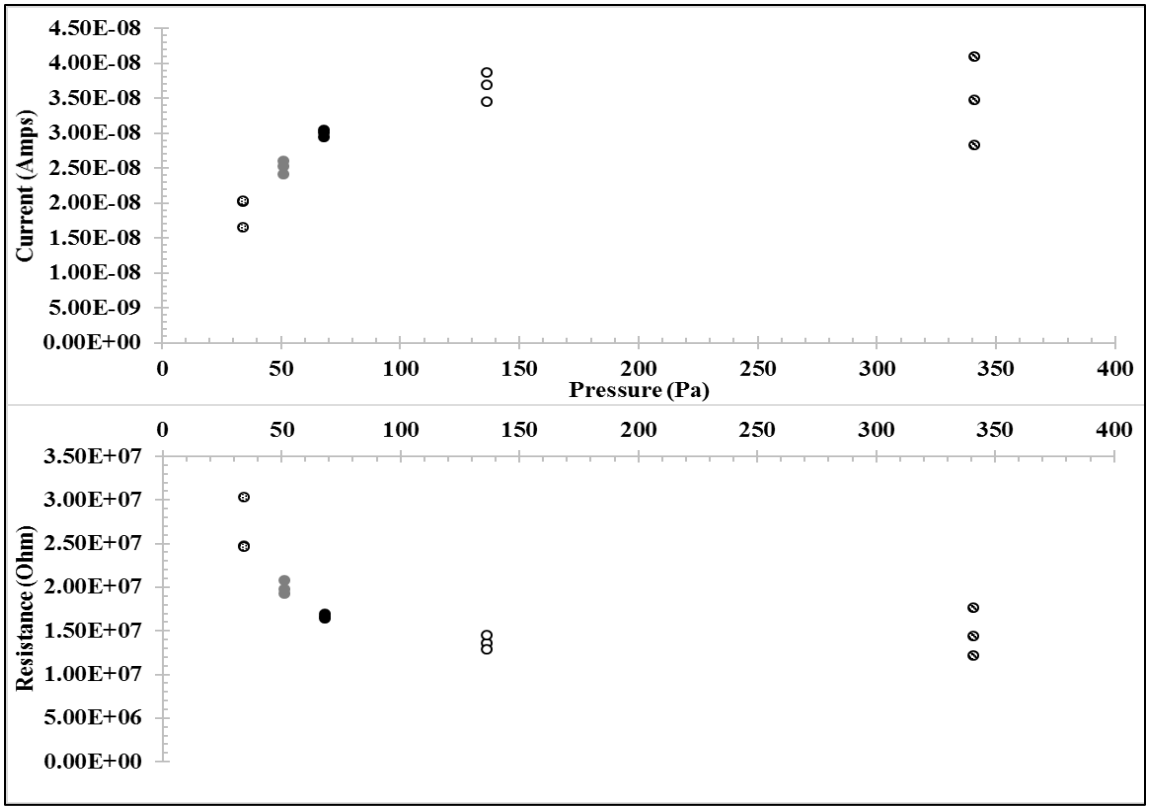

Figure 17. Shear Pressure vs Current and Resistance data for FFF 3D printed 1.33:1 composite sensor. Sensor used an applied voltage of -0.5V. Data point clusters going from left to right represent 0.5g, 0.75g, 1.0g, 2.0g, and 5.0g masses applied in the shear direction. A samples size of N = 3 was used for each mass.

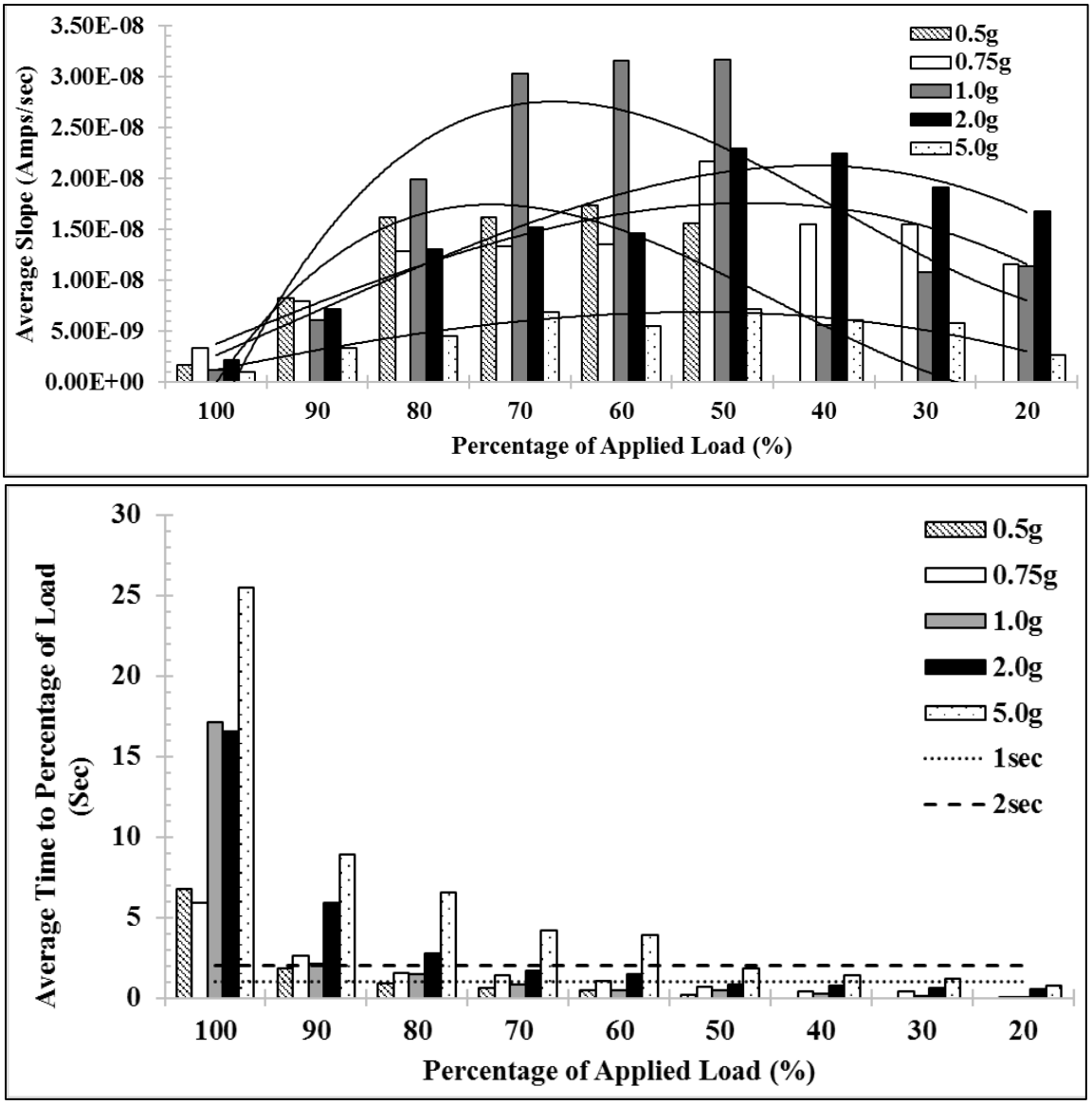

Figure 18. Shear pressure response time for 1.33:1 FFF 3D printed sensor. Top row: Average slope versus percentage of applied load. Bottom row: Average time to percentage of applied load. Straight dashed lines represent one and two second thresholds.

These plots show that a response time for under one second can be determined by using the unique slope seen at 50% of applied load or by using the change in slope from 20% to 50% of applied load. For the masses 20 grams and under for the 1.33:1 sensor,

response times for below one second can be seen at 90% or less of applied load due to the low pressure. This is valuable for fine motor control for prosthetics since performing fine motor tasks is ideal for increasing prosthetic performance.

Using a moving two-point average for the plots, black lines on bar graph, we can see a common parabolic, or inverted parabolic, curve trend for the 1.33:1 and 1:1 sensors. This curve represents the non-linear uptake of pressure that shows an initial high rate of load detection and then a decline in rate when the pressure gets close to steady-state internal pressure. The two dashed (250g and 650g masses) moving two-point average plots on the 1:1 sensor graph are the plots following a linear trend instead of the parabolic curve. These two curves still follow the initial high rate followed by the decrease in detection rate though. The overall trend between both sensors is that as the applied load decreases, the slope at each percentage of applied load decreases with a few data points that do not follow the trend shown.

For the FFF printed shear sensors, the predictive response time used above is need. In figure 18, the data shows that the shear sensor has the greatest impact when detecting minute shear force changes, 0.5g to 1.0g. This allows the shear sensor to detect immediately when an object is being grasped, touched, or falling/slipping. The unique slope change from 20% to 60% for forces from 0.5g-1.0g allows the sensor to have a response time under one second. Where using the sensor to detect forces 0.5g and under, will allow for 80% of applied load detection under one second and under two seconds for 90% of applied load.

FFF 3D PRINTING WITH LARGE NOZZLE DIAMETER

For printing on a Fused Filament Fabrication device, it is difficult to force a weak and flexible material through the nozzle for extrusion. The difficulty is caused by the fact that the filament relies on the hot nozzle temperature along with pressure from the feeder gear that is located away from the heating chamber and nozzle. With the composites described here, the difficulty happens since the feeder gear is far away from the nozzle it causes buckling within the feeder tube, heating chamber, and nozzle, see figure 13.

To combat this, the nozzle and heating chamber diameter was expanded to 1.58mm, which is almost the same diameter as the filament, to decrease the chance of buckling within the system. When the filament is in our heating chamber it expands to a diameter of 1.75mm, now the nozzle diameter is only being reduced 0.17-0.22mm from the filament diameter, where printing with ABS uses a 0.35mm nozzle diameter and causes a diameter reduction of 1.4mm. The larger nozzle opening allows for little back-pressure on the filament and also compensates for the composites thermal expansion. Since the composite uses a filler material that is incompressible and non-flowable, when the polymer matrix expands it pushes the graphite particles outwards and increases the diameter of the filament without having the particles transition to a molten state. Therefore, we have to apply mostly radiating heat with very little pressure and slow speeds to 3D print the composites with large filler ratios.

DESIGN IMPACT/ADVANTAGES

The FFF 3D printed sensors presented here can be used as a tactile sensor for daily activities and can be used to detect levels just above a light touch and minute changes in shear force. Since the 1:1 or 1.33:1 3D printed sensors can detect between 3.4063kPa - 51.0938kPa (50-750grams) and 0.3406kPa - 20.4375kPa (5-300grams) in pressure, with daily activities (DA) and a light touch operating in the 10kPa and 100Pa range, the pressure sensors presented here can be used in conjunction with one another to create a dual or zone sensor that can operate for the DA's and light pressures. Where the shear sensors can detect between 34.06Pa and 640.63Pa shear pressure. This allows for early detection of movement across the sensors surface.

This allows for a low cost, simple fabrication, and low-level detection pressure sensors that can be customized to the user's needs and wants. Figure 19 visually shows the sensors presented here compared to thick/thin film sensors and human skin pressure levels. Where the shear force sensor can detect minute changes in object placement along the sensors surface. This allows the sensor to detect and predict when an object is falling or slipping out of the prosthetic's grasp.

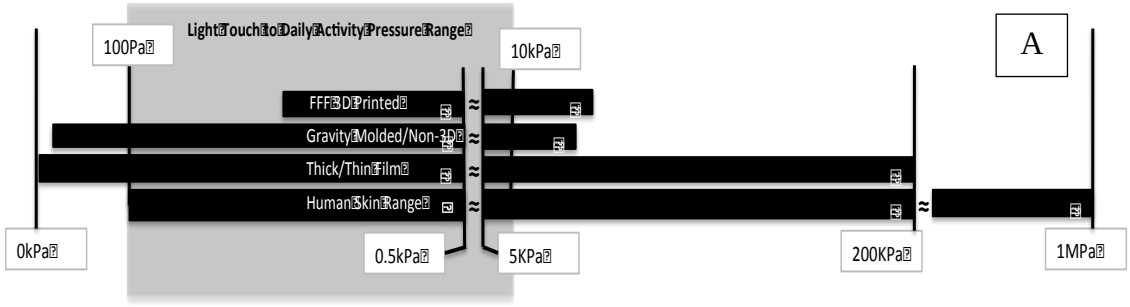

Figure 19. (A) Pressure sensor ranges of the FFF 3D printed and molded sensors compared to current thick/thin film sensors and human skin detection limits.

The printed pressure sensor's also show positive hold values, up to pressure values for daily activities (10.22kPa), where the sensor is able to maintain a fairly constant output when a constant load is applied for 120seconds, figure 20 and table 6, when compared to a small human trial. The human trial used three samples/subjects with two tests for each sample. The subjects would lift a T-shaped object, figure 21, off a table no more than 50mm and hold it for 120seconds while seated using only their thumb and pointer finger. The T-shaped object had a 50g mass in its base with two force sensors on either side of its shaft. The results showed that the average variance or fluctuation in human data was 45.6% greater than either the 1:1 or 1.33:1 sensor.

The human data demonstrates that the human hand cannot hold a constant force on an object and is constantly readjusting/evaluating the applied pressure needed. Where the minimal variance in pressure sensor data does not affect the applied pressure range above or below it. Therefore, the variance for each applied load falls within the acceptable limit for that range of pressure. Additionally, the object being grasp will be constantly fluctuating, resulting in the sensor readjusting its baseline value continually. With a varying baseline, the sensor will not be holding a true constant applied load.

Fluctuations in Grip Force (N)		
High	Low	Difference (%)
9.99	6.1	38.94
9.59	6.5	32.22
13.36	6.06	54.64
12.18	5.88	51.72
10.09	6.28	37.76
	Average	**43.06**

1:1 FFF 3D Printed				
Mass (g)	Pressure (Pa)	Voltage Start (V)	Voltage End (V)	Difference (%)
50	3.41E+03	4.07E-11	4.54E-11	11.55
100	6.81E+03	3.59E-10	4.83E-10	34.54
150	1.02E+04	6.81E-10	9.32E-10	36.86
			Average	27.65

1.33:1 FFF 3D Printed				
Mass (g)	Pressure (Pa)	Voltage Start (V)	Voltage End (V)	Difference (%)
5	3.41E+02	8.34E-10	1.16E-09	39.09
10	6.81E+02	1.19E-08	1.22E-08	2.52
50	3.41E+03	2.74E-08	4.38E-08	59.85
100	6.81E+03	1.09E-07	1.22E-07	11.93
150	1.02E+04	2.27E-07	2.86E-07	25.99
			Average	27.88

Table 6. Shows the fluctuations in applied pressure force over a 120second sample hold time. (Top Table) Fluctuations, high vs. low values, in grip force with human testing. A sample size of three was used with two tests per sample. (Middle and Bottom Tables) Show the 1:1 and 1.33:1 FFF pressure sensor hold response.

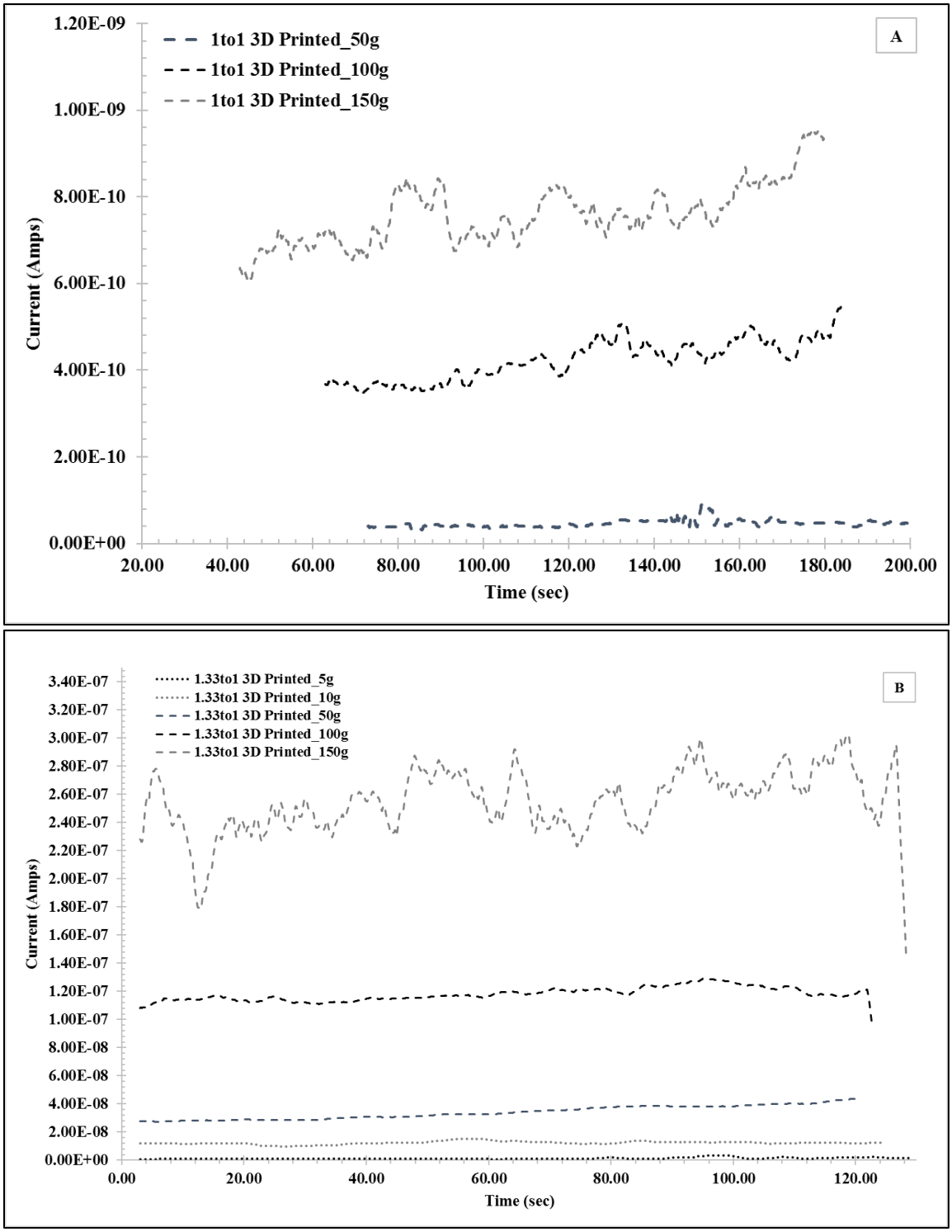

Figure 20. Fluctuations in applied pressure over a 120second sample hold time with 1:1 and 1.33:1 printed pressure sensor samples. Samples were tested up to 150g (10.22kPa) to demonstrate its holding capabilities for daily activities.

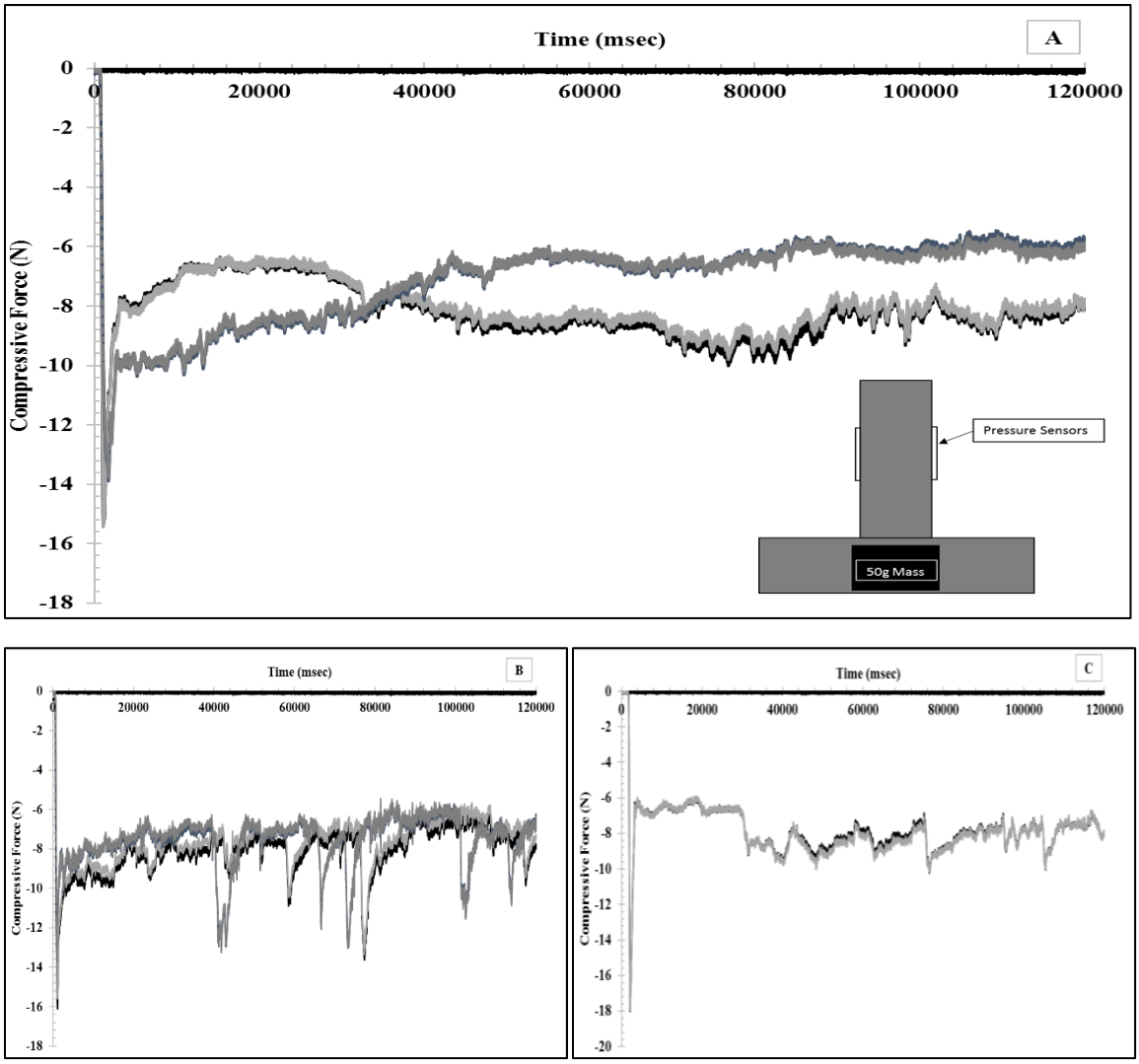

Figure 21. Fluctuations in applied pressure force over a 120second sample hold time with human samples. Graphs A-C represent each sample, where the black/light gray line and dark gray/steel blue line are tests one and two. Graph C only had one test performed. Subset image in graph A is the test device used for the hold testing. The T-shaped device has a 50gram mass in its base and two force sensors on its vertical shaft. The high vs. low values are shown in table 6.

The 3D printed sensors also have the ability to be embedded within a 3D printed part to allow for complex devices to be manufactured or created. Where devices with unique/difficult geometries can have sensors placed in locations that are currently too difficult to place a sensor in. Being able to 3D print a fully function sensor without the

needed for additional manufacturing will open up the opportunities for new and intelligent completely 3D printed devices.

Lastly, the molded pressure sensors can still be formed in any 3D printed mold to create unique geometries and ideal pressure sensor designs. These molded sensors will not have the same flexibility and ideal fabrication techniques but they can allow for a low cost, effective pressure sensor that can detect pressure values all the way down to 17Pa, well below the pressure value for a light touch. Detecting values well below the light touch threshold will allow prosthetics to be able to detect the early onset of contact with an object allowing the user to have feedback before a person without an amputation can detect.

DESIGN PIFALLS/DISADVANTAGES

The FFF tactile sensor presented here has many benefits as a sensor but needs further dynamic force testing and designed with a surrounding material to encapsulate the composite materials presented above. The surrounding material needs to be a highly compressible elastic material to allow for an increase in response time. The sensor has a low response time, under one second, using the current predictive technique, but needs to have a quicker response time, around 10msec, to create a biomimicking response time.

The surrounding material will allow the forces imposed on the sensor to compress quicker than the conductive composite created above, which will allow for the sensor to have an increased response time since the composite will have a smaller compressive displacement. The smaller displacement is created sense the effective load seen by the conductive composite will now be less, therefore generating a smaller compressive

displacement. When using the material characteristics presented above, we can see that smaller loads/displacements result in quicker response times due to the relative large compressive displacements. The relative larger displacements are caused by there being more effective compressible room when using a smaller load compared to a large load. The larger loads need more time to reach a steady state signal since there is less room for compression as the carbon particles come closer together.

Lastly, the tactile sensor needs to be tested with dynamic and gradual/onset forces. Dynamic forces, i.e. impacting or sliding, will have different response characteristics than static forces, which were used for the data presented above. Then gradual or onset forces, i.e. applying a gradual increasing grip force on to an object, will need to be tested to evaluate the change in outputted current when an increasing force is being applied in a constant fashion.

Testing the tactile sensor with static loads provides valuable material and response characteristics but does not demonstrate how the sensor will respond to a dynamic setting; where both dynamic and static settings are seen in a real-world environment.

CONCLUSIONS

Presented here is an alternative to the current strain gage and thick/thin film sensors with a 3D printed piezo-resistive tactile sensor that can operate within the daily activity range, within the same magnitude as a light touch on human skin, and detect early changes in shear force. We have also presented other advanced manufactured

sensors that can formed in to a 3D printed mold and detect pressure ranges down to 17Pa and up to 47kPa.

The 3D printed sensors can be printed in one step with no post-processing needed and has an approximate manufacturing cost of $0.125, ignoring equipment and manufacturing overhead. The sensor can also be embedded within a 3D printed prosthetic or part to create intelligent, one manufacturing step devices. The option for creating embedded electronics will allow for improvements and help grow the area of 3D printing and medical devices. We have also demonstrated a type of radiating heat 3D printing with little nozzle pressure to create 3D printed parts with high filler composite filaments.

Future directions are to develop the sensors with FFF printed electrodes and housing to demonstrate a complete 3d printed tactile sensor system. Figure 22 shows the future housing design that will allow for shear force and pressure to be detectable separately and simultaneous with a two-chamber design. Where figures 23 and 24, show preliminary testing using the FFF 3D printed 1:1 and 1.33:1 pressure sensors presented above with a FFF PLA-Carbon black powder mixture electrodes. The electrodes, fabricated with Graphene 3D Lab's Conductive Graphene PLA filament, are 1.0mm thick, with a 12x12mm surface.

Material characterization shows that the PLA-Carbon material has an increase in resistivity (Ωm) of $1.39x10^5$ % compared to copper. The pressure sensor results with PLA-Carbon electrodes show that the power trend is still present and there is

approximately a 100% difference from the copper, previous testing, to PLA-Carbon electrodes.

There are fluctuations in resistance change at the higher-pressure values caused by the uneven surface on the printed sensors, figure 24. Due to the even surface, the top electrode can tilt under high pressure causing a change in recorded resistance. To resolve this issue, the modified extruder system described above would need to be developed or the electrode would need to be fabricated with a surface fitting design so that it can have higher stability on the sensor's surface.

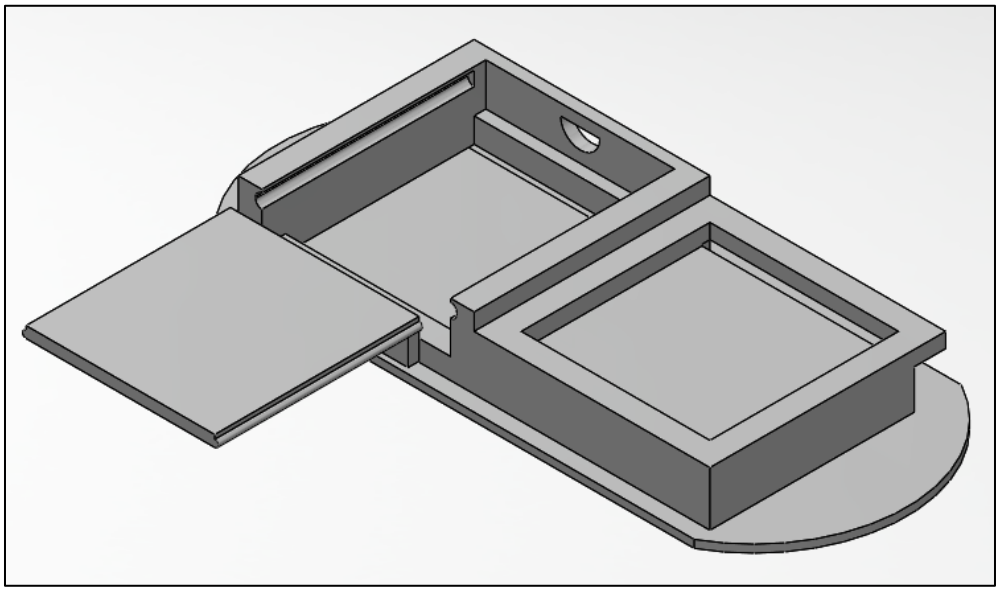

Figure 22. FFF 3D printed housing for pressure and shear sensors. Pressure sensor housing is represented with the bottom chamber and the shear sensor housing being the top chamber with sliding lid.

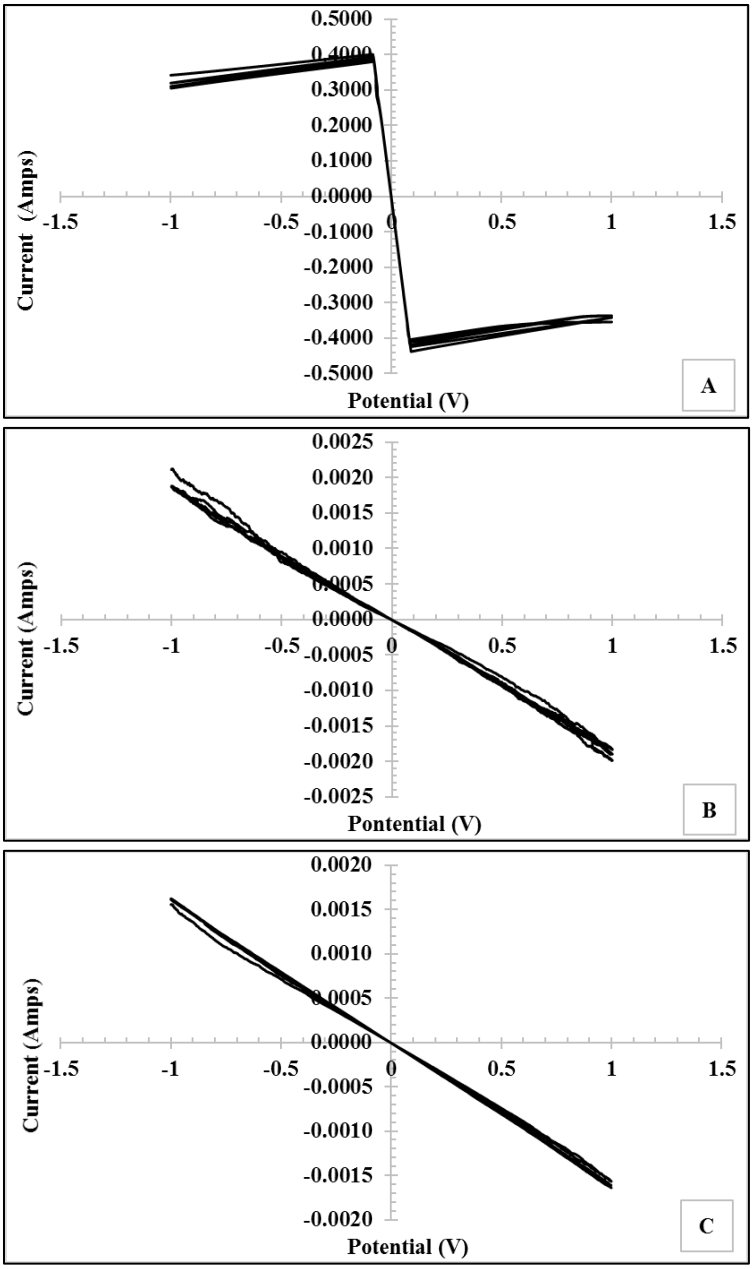

Figure 23. CV sweeps from -1.0 to 1.0volts for copper wire (A), PLA-Carbon powder filament (B), and PLA-Carbon powder single electrode (C).

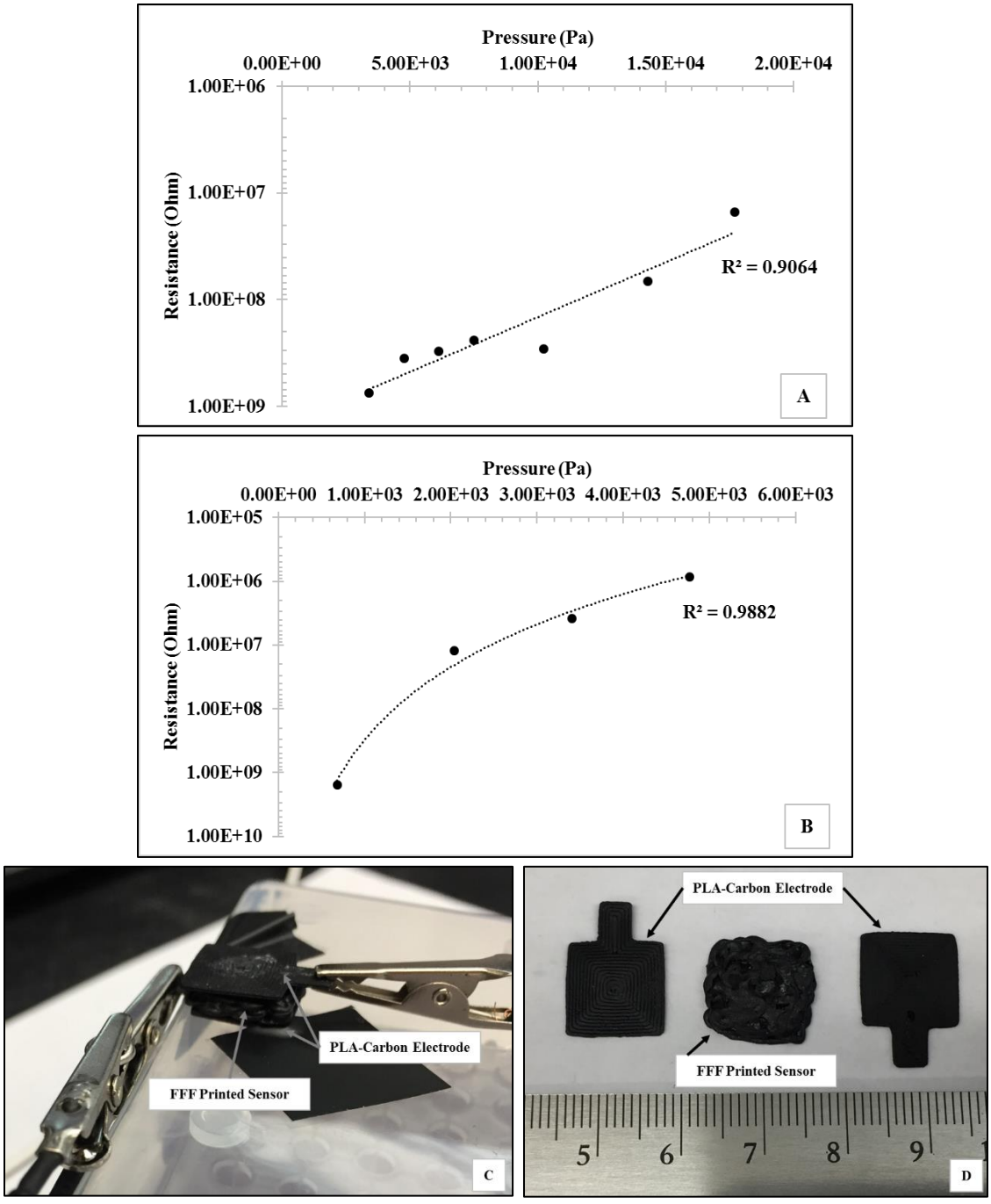

Figure 24. Preliminary FFF printed 1:1 (A) and 1.33:1 (B) pressure sensors with conductive PLA-Carbon powder top and bottom electrodes. Y-axis is Log_{10} with each data set following a power curve. Applied voltages of -0.5V and -0.2V where used for 1:1 and 1.33:1 sensors respectively. Images C and D show the test sensor(s) layout with the PLA-Carbon electrodes.

CHAPTER SIX: FUSED FILAMENT FABRICATION 4D PRINTED BIOMIMICKING ACTUATOR WITH PLA AND TPU SHAPE MEMORY POLYMER COMPOSITE FOR PROSTHETIC ACTUATORS.

INTRODUCTION

To overcome the issues of high operating temperatures, low contractile strain, complexity, high weight and cost, and linear output, a Fuse Filament Fabrication (FFF) 3D printed shape memory polymer (SMP) actuator that has non-linear contractile and passive forces, contractile forces comparable to mammalian skeletal muscle[94-99], reaction time under one second, low operating temperature, high contractile strain, and low cost, mass, and volume was developed.

SMP's are able to recover a predetermine/memorized shape (shape memory effect) by shaping the polymer at room temperature or in its glass transition temperature (Tg) range. Using the Tg allows the polymer to be easy shaped/deformed since the polymer has transitioned from a hard/glassy state to a soft/rubbery state, where the polymer-chains can be rearranged. The polymer is then cooled (shape fixity) in its deformed shape until it returns to a glassy state. Once the polymer is heated to its Tg, it recovers its original shape/polymer-chain configuration.

The biomimicking actuator here is achieved by melt-blend mixing poly-lactic acid (PLA) and thermoplastic polyurethane (TPU) in a 7:3 ratio respectively[100,101]. Where PLA and TPU both demonstrate shape memory effects, but blending them together introduces additional elasticity from the TPU and shape fixity at room temperature from

the PLA. The composite is then manufactured in a 2D spring shape design and uses radiating heat to generate actuation. Using a shape memory polymer allows the actuator to memorize a predetermined shape and recover that shape with the application of heat when the polymer is deformed/displaced.

MATERIALS AND METHODS

The SMP composite was created by using purchased PLA and TPU filament, from SainSmart, that was then cut to pellet rods. The pellets where then aerated in a funnel with compressed air, and a film of 99.9% isopropyl-alcohol and grounding wire to minimize static charge build up, figure 25A. Aeration was performed by applying 100.0psi compressed air with three second bursts for 60seconds with 28.5grams of composite mixture until a homogeneous mixture was obtained. The mixture was then extruded in to a filament with the use of a single screw extruded with a 1.5mm nozzle diameter. The extruder had a nozzle temperature of 180.0°C with a screw rotational speed of 0.037revolutions/sec.

All actuators were designed on SOLIDWORKS 3D-CAD and FFF on a MakerGear M2 with Simplify3D software. Actuators had a cross-section of 1.5mm x 0.4mm, overall length and width of 50.0mm and 12.38mm, and were printed with a 0.35mm diameter nozzle at 240.0°C with the bed at 70.0°C; figure 25D. Software was coded to print with an: extrusion multiple of 0.97, extrusion width of 0.39, layer height of 0.3mm, and a printing speed of 600.0mm/min.

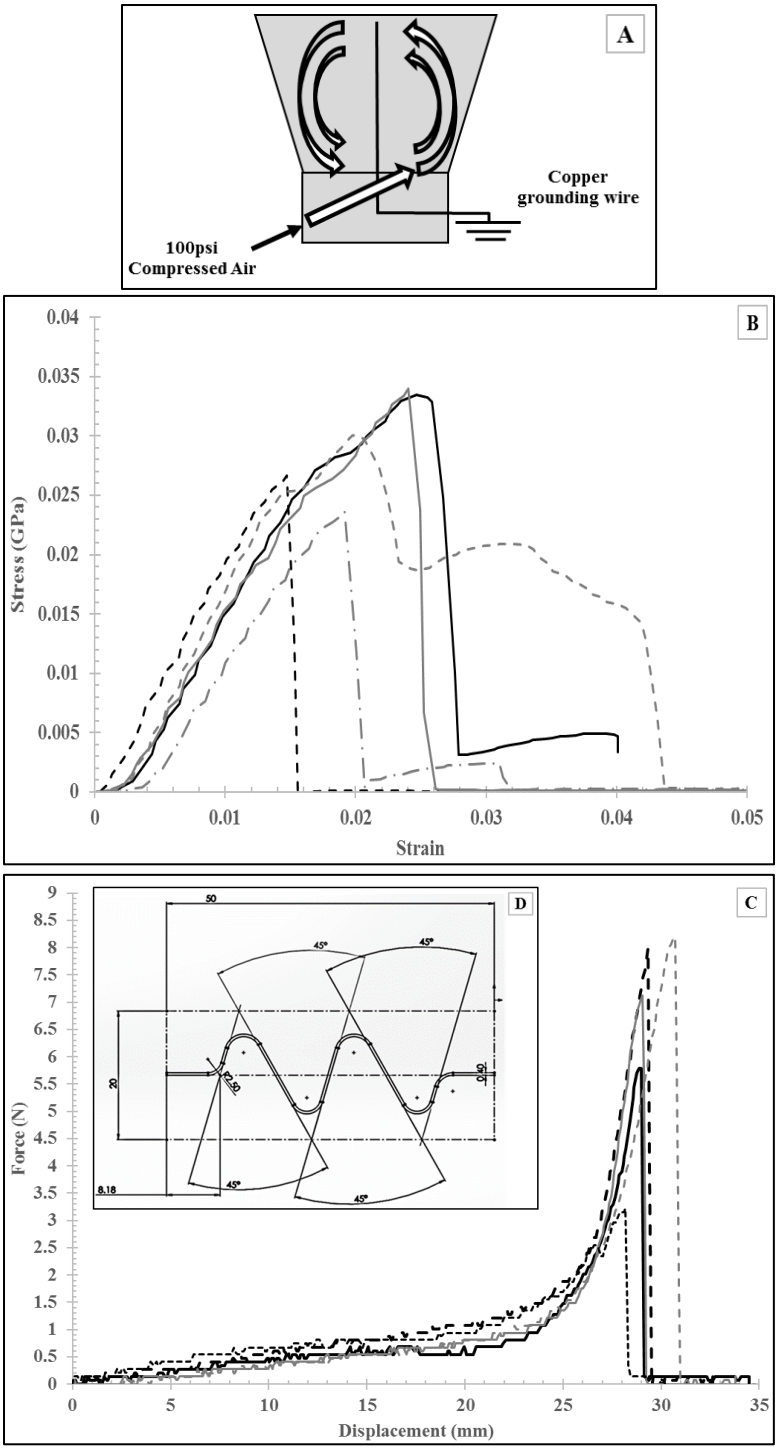

Figure 25. Image A shows a diagram of the aeration technique used to mix the PLA and TPU pellets, with the grounding wire and air circulation patters. Image B shows the tensile stress vs. strain of the extruded SMP filament, with a sample size of five. Image C shows the tensile testing of the FFF SMP actuator. Image D shows the layout/design of the FFF SMP actuator.

Physical and chemical material properties where acquired with the use of Fourier-transform infrared-spectroscopy (FTIR), differential scanning calorimetry (DSC), scanning electron microscope (SEM), and tensile testing. SEM images were taken of sections at the ends and middle cross-sections of the actuator. Sections were made by freezing the samples at -10°C and the cutting with a razor blade at 90° and 45°. Tensile testing used an MTS Model Sintech 1/S tensile machine (maximum load cell capability of 900lbs). Where actuator force data was collected with an iWorx data logger, 250gram force transducer, and a 100°C k-type thermocouple transducer to monitor force and temperature simultaneously.

To deform the actuators/samples, a water bath of 70.0°C was used to strain each sample to the varying pre-determined strain values; strain values include 100%, 80%, 60%, 40%, and 20%. The range of predetermined strain values was to demonstrate the range of recovery force with varying strain input, while 70°C was used since the glass transition temperature of PLA is 60-65°C. Additionally, the samples were cyclically fatigued by stretching and recovering its shape at 70.0°C for each strain value. This process was also used to measure the strain recovery of each fatigue cycle at each strain percentage.

To ensure that each sample was at room temperature prior to being stretched, the samples would be submerged in the water bath, stretched, and then allowed to cool at 21.0°C for five minutes prior to testing. For fatigue cycles greater than one, the process is repeated until the fatigue cycle number is reached.

Force data was collected by placing the samples in an incubator with a temperature ramp rate of 1.12°C/min to accurately show the onset and end of the contraction cycle; incubator was heated from 30°C to 70±5°C. Additionally, an increased heating source was created with ceramic heating elements to demonstrate the actuator force characteristics under a temperature ramp rate of 8.68celcius/min, approximately eight-times faster. The ceramic heating system was placed inside of the incubator, where the incubator was heated up to 40°C to get the entire chamber at 40°C and then the ceramic heating elements were activated to reach 75°C. Two 40.0mm diameter circular ceramic heating elements, with an internal resistance of 4.8Ω, were used with an applied 9.0V and 1.015Amps to generate radiant heat.

RESULTS

MATERIAL CHARACTERIZATION

Once the SMP filament was extruded it was tested with an FTIR machine to identify that both PLA and TPU were present in the melt mixed blend. FTIR samples of PLA, TPU, and SMP filament were tested with a sample size of three with sweeps from 4800-400cm^{-1}. Additionally, the FFF printed actuator was tested with a sample size of three to show that the extruded device still had a blended polymer matrix, figure 26A-D. FTIR results show that all key bonds are present in all samples and types.

Following FTIR testing, the extruded SMP filament was visually evaluated with an SEM to view the distribution of TPU within the PLA matrix, figure 27A. Imaging was taken with an oblique cut, approximately 45°, through the filament and imaged from

x1500-x20,000 magnification. Images showed that the distribution of TPU within the matrix is even apart from one area where the TPU appears to be clusters instead of blended.

SMP filament was tensile tested to show its mechanical material property at a loading rate of 50mm/min, following ASTM D638 standard. Five samples were tested in tension and showed that the SMP filament is brittle, due to the 70%PLA matrix content. Testing showed a consisted linear elastic region with fluctuations in peak stress ranging from 0.0337GPa-0.0236GPa, figure 25B. Fluctuations in peak force appear to be indications of TPU clusters seen in SEM imaging.

FFF ACTUATOR CHARACTERIZATION

To determine the shape recovery (SR) percentage at each strain and fatigue cycle, the samples were stretched and SR at 70°C. Results after five cycles show that 100% strain has the lowest SR of only 24.6%, 80%-60% have similar recoveries of 31%-29.2%, and 40-20% have the highest at 43.2%-42.6%, figure 28A-F. It is observed that using strain values of 100%-80% result in actuator material fracture/peeling due to the increased induced stress with fatiguing. The ideal strain is 60% due to the high SR similar to the 20% for typical mammalian skeletal muscle strain[94-99], and positive material fatigue results, while 40% and 20% strain generate no stress recovery.

The response time, time at which shape recovery begins, was also determined since the true actuator response time cannot be established due to the force testing

system. Response time was determined with a FLIR One thermal imaging camera (frame rate of 0.11seconds) and the 70°C water bath, figure 28G. The actuators were attached at one end on the platform, allowing the other end to be free to move/actuate, and submerged in the water bath at a low incline angle, 10-15°. This allows for the actuator response to be measured without a rush of water generating high turbulence if the platform was submerged parallel to the water.

The imaging showed that the actuator with a thickness of 1.5mm had an initial response time of 0.77seconds. Additionally, actuators with thicknesses of 1.2mm and 0.9mm were tested for response time and had response times of 0.77seconds and 0.66seconds respectively. The thinner samples were not tested for contractile forces since they would not generate enough force for the force transducer and were difficult to remove from the bed without damage, but show that a thinner sample would have an increase in response time.

For the actuator force testing, the actuators were tested similar to an isometric muscle contraction. Where the FFF actuator is stretched to a given strain percentage, fixed at the bottom and to the force transducer, and then heated to 70°C. Strain values used show the range of capable displacement values for the actuator since straining above 100% causes fracture in the actuator during stretching. The strain values of 100%, 80%, 60%, 40%, and 20% represent displacement values of 50mm, 40mm, 30mm, 20mm, and 10mm respectfully.

From the results, figure 29A-I, the samples with 100% strain cycled one to five times showed the largest peak force along with the greatest rate/slope of force generation. Where the force and rate decreased linearly as the strain percentage decreased until 40% and 20% when the actuator could not generate enough internal stress to cause a recovery stress/force. The peak contraction values for each strain are comparable to mammalian skeletal muscle contractions and follow a non-linear force generation due to the spring shape design and force generation throughout the entire glass transition zone.

Where mammalian contraction values range from 0.1MPa (typical/average) to 0.45MPa (maximum), and the actuator here ranges from 0.58MPa to 0.17MPa for 100% to 60% strain respectively. It is observed that after cycling the actuator once there is an initial drop in peak force and rate averages, followed by a relative leveling or constant peak force and rate. Additionally, we see that the 60% strain samples tested in the ceramic heating system show comparable result averages to its counterparts tested in the incubator chamber. This demonstrates that increasing the heating rate will not affect the performance of the actuator. 60% strain was chosen since it demonstrated the highest strain recovery with minimal material failure.

To show the non-linear passive tension characteristics of the actuator, five samples were tested in tension at 50mm/min. The results show that as the actuator is displaced, there is a shallow force uptake followed by a steep absorption of force and then failure at 30mm of displacement, which follows the non-linear passive tension that skeletal muscles demonstrate[94-99], figure 25C.

ANALYSIS FOR FFF VARIANCES

To determine the quality of the actuator and if there is any thermal degradation of the SMP after FFF, SEM imaging and DSC testing were performed. DSC results, figure 26E, show that there is a decrease in thermal energy required to progress through each material phase when the filament is extruded again when FFF. The glass transition and melting temperatures are similar, but the decrease in heat flow/specific thermal energy demonstrates that there is less energy needed to go from one state to the next due to thermal degradation. Furthermore, there is spike in exothermic energy during annealing of the filament that is not seen in the FFF actuator.

SEM images, figure 27B, show that there is inconsistency in the density/layer adhesion throughout the FFF actuator. Imaging shows parting lines where the printed layer has not fully or partially fused with the layer beneath it, and that the cross-section is not uniform with valleys and peaks present.

DISCUSSION

MATERIAL CHARACTERIZATION

Initial FTIR and tensile material analysis showed that the extruded SMP filament and FFF actuator had the appropriate carbon (C), hydrogen (H), oxygen (O), nitrogen (N), Sp^3 carbon to hydrogen, and carbon to carbon or oxygen double bonds for PLA and TPU, figure 26A-D. The FTIR results show the amount of infrared-radiation (IR) absorbed versus wavenumber. This is obtained since absorbed IR causes a molecule to be

excited into a higher vibrational state. Where the change in energy from the at-rest to excited molecule state is a function of the amount of absorption at a wavenumber by a particular molecule/bond[102].

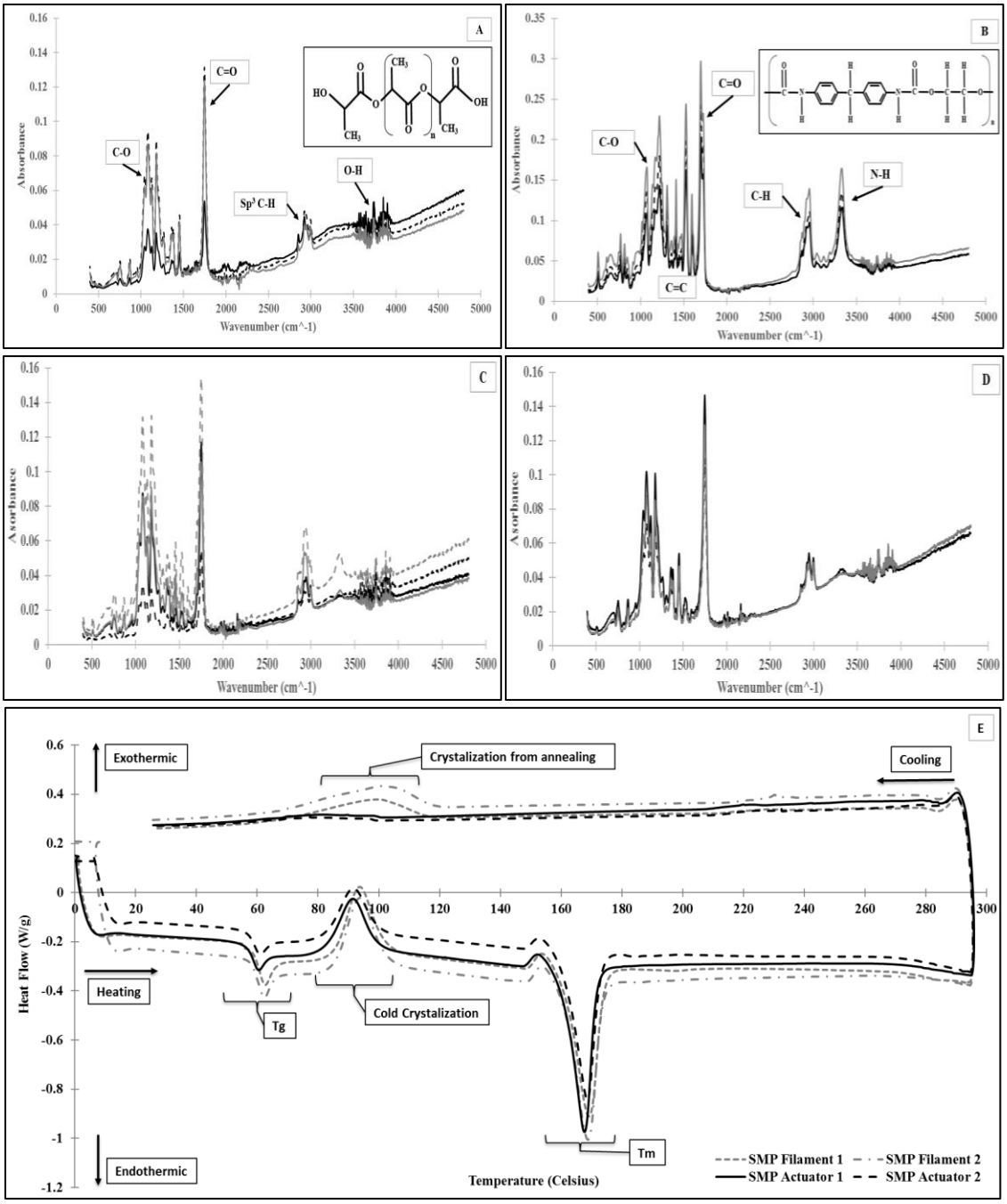

Figure 26. Graphs A-D show the FTIR results and key bonds of the PLA (A), TPU (B), SMP filament (C), and FFF SMP Actuator (D); the PLA and TPU molecular structures are shown within their respective graph. Graph E shows the DSC curve of the SMP filament and FFF SMP actuator. Graph E demonstrates that there is a thermal degradation from the filament to the FFF actuator.

FTIR testing was followed with SEM imaging to evaluate the distribution of TPU within the PLA matrix since PLA makes up 70% of the blend. In figure 27A, the samples were coated with a gold/palladium film to remove charge from the surface during imaging. The dark regions/area make up PLA where the lighter or white highlights/regions are TPU. There is even distribution of the TPU within the matrix, with possible regions of TPU clustering. Imaging shows possible clustering within the matrix since the TPU particles are spherical/isolated instead of elongated and distributed. The clustering effect could have been caused by using a single-screw extruder with a premixed pellet blend. Where a twin-screw extruder with simultaneous blending could resolve the particle isolation issue. This clustering effect appears to have influenced the tensile peak results of the SMP filament.

Where the tensile results showed consisted linear elastic regions with fluctuations in peak stress. These fluctuations may have been caused by clustering, where a large cluster may cause a high stress or weakening point in the sample and cause it to fail early. Additionally, two samples showed a slight increase in ductility with one sample having a secondary peak. The increase in ductility and the secondary peak are due to a particle or cluster of TPU material within the cross-section. Even though SEM imaging showed an evenly distributed composite, if the point of failure in the filament has a cluster of TPU the sample can demonstrate a secondary tensile peak. The increase in ductility is minimal in these samples and does not affect the elastic tension regions. Where the actuator only works within the elastic region of the polymer since going above the elastic region would cause plastic deformation in the actuator.

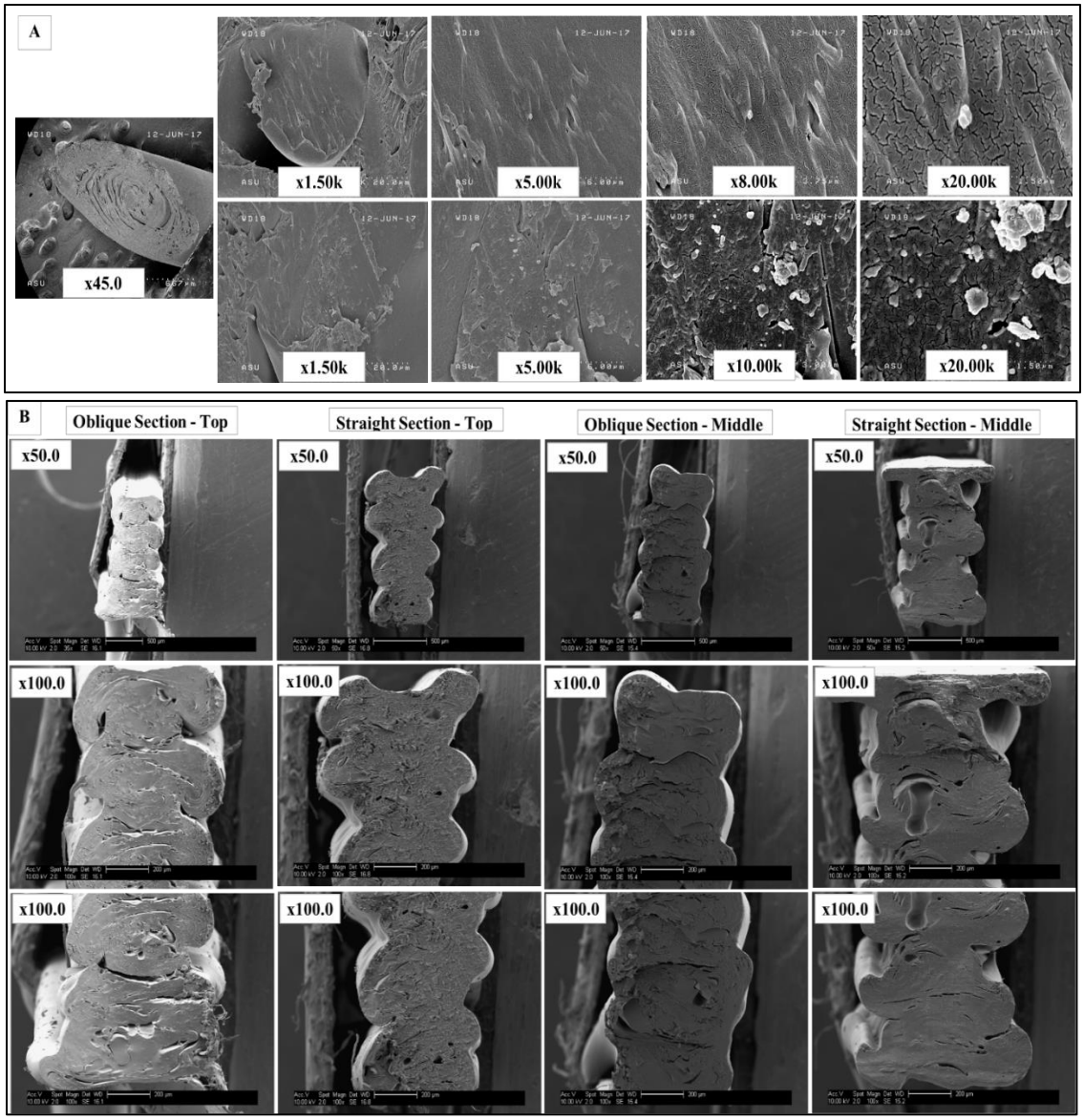

Figure 27. Section A represents the SEM images taken of the extruded SMP filament prior to FFF. Where the x45.0 magnification image shows the oblique cut made through the filament. Section B represents the FFF SMP actuator with oblique and straight sections made through the cross-section at the tops, or ends, and middle of the actuator.

FFF ACTUATOR CHARACTERIZATION

The functionality of the actuator was demonstrated with contractile, SR, and passive actuator tensile testing. Shape recovery, along with initial response time, show that the actuator with 60% strain is optimal for SR with a response time of 0.77sec, figure

28. Since cyclic fatiguing appears to level off after five cycles for all strains, 60% strain is ideal since it achieves 29.2% recovery with minimal plastic deformation.

Strains of 80% and 100% exhibit higher peak force and higher response rates, but due to the increased applied stress, have lower SR due to plastic deformation/breakage. Since the actuator has an overall length of 50mm with 78mm in material length, when the material is strained well past 78mm it begins to fail. Where 60% strain is only displaced to 80mm, which results in minimal applied strain (2.0mm) after full stretch while still generating internal stress. This allows the actuator to stay within the elastic region of the composite; demonstrated in figure 25B.

The spring shape design allows the actuator to have a: high deformation prior to change in CS, and high SR response initially due to the decrease in CS (high stress on polymer-chain structure) followed by a lower response once the CS is recovered (low stress on polymer-chain structure). Where a straight line/wire would only allow for deformation of the polymer with a decrease in CS, which would cause plastic deformation at low strain levels due to the brittle nature of the polymer and decrease SR. This effect is seen where the 100%-80% strain samples have a low SR due to plastic deformation and the 60%-20% samples have a high SR due to no plastic deformation, figure 30.

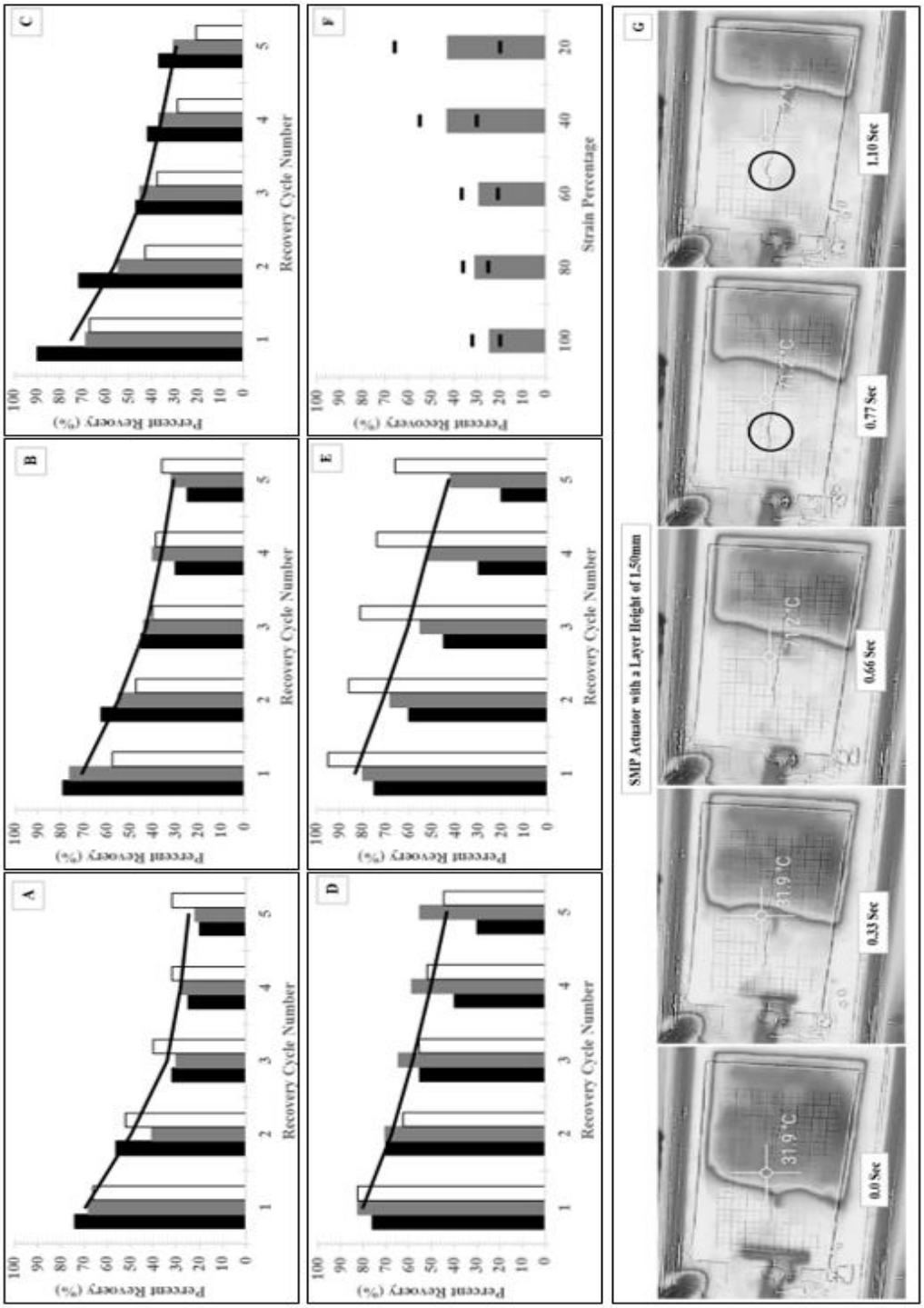

Figure 28. Graphs A-F show the shape memory effect or strain recovery of each strain at cycles 1-5, where A = 100% strain, B = 80% strain, C = 60% strain, D = 40% strain, and E = 20% strain; where the black line represents the samples average at each cycle. Thermal imaging time-step, G, show the onset of shape memory effect of an SMP actuator with a layer height of 1.5mm. The black circle shows the onset of shape recovery, which is at 0.77sec after contact with 70°C DI water.

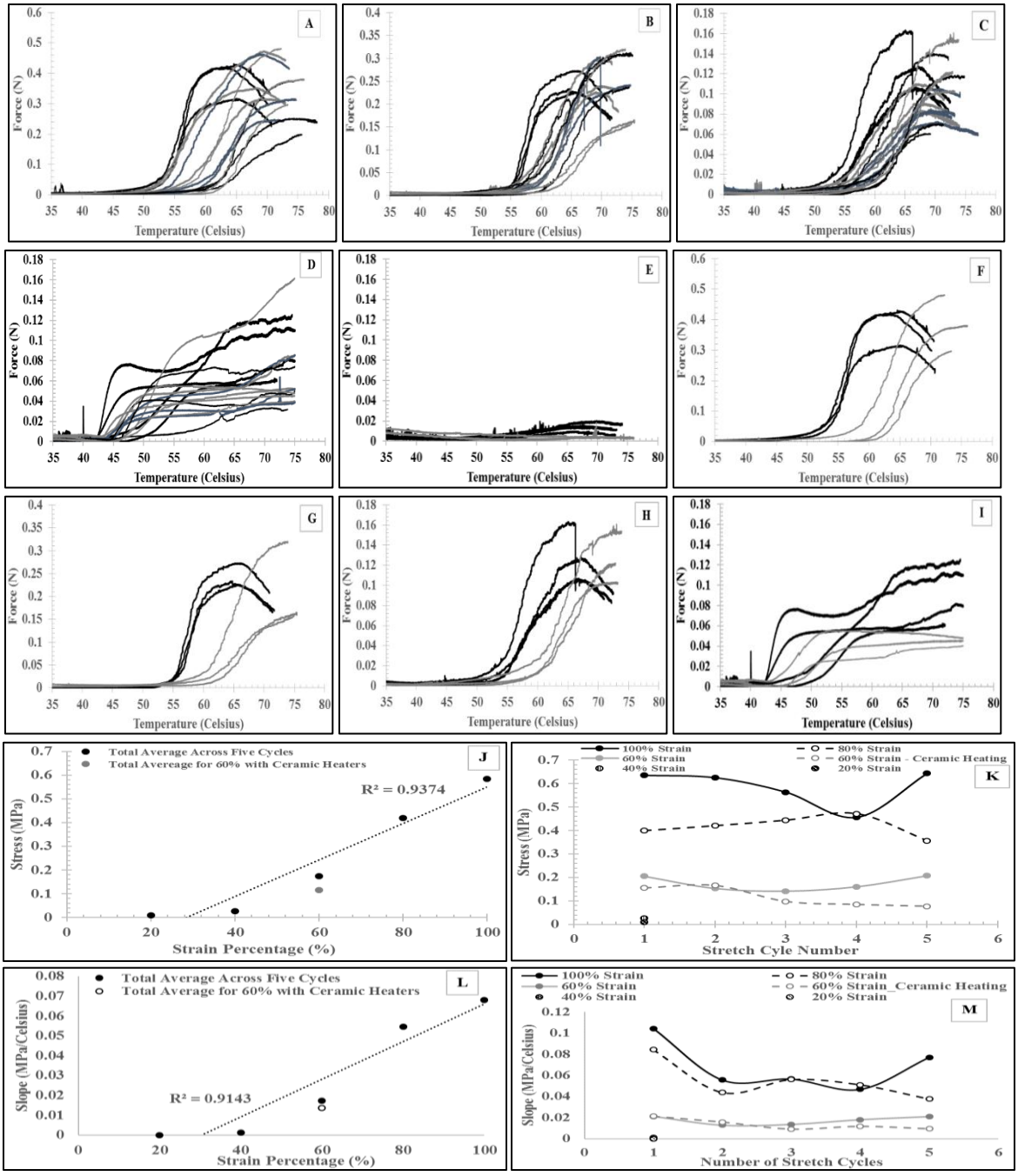

Figure 29. Graphs A-E show each strain with cycles 1-5, where A = 100%, B = 80%, C = 60%, D = 60% with Ceramic heaters, and E = 40 & 20%. Graphs F-I show strains 100-60% with only cycles 1 and 5, where F =100%, G =80%, H =60%, and I = 60% with Ceramic heaters. Cycles 1-5 samples are represented in order as follows: thick black (cycle 1), thick gray (cycle 2), thick steel gray (cycle 3), thin black (cycle 4), and thin gray (cycle 5). Graphs J-M show the average stress and slope (stress/degree Celsius) at each strain (J and L) and the average stress and slope at each cycle number (K and M).

Results, figure 29J-M, from the force/contractile testing showed that as the strain percentage decreases, the peak force and rate (stress/°C) decreases as a linear function. This linear decrease is due to the function of input/applied stress generated during stretching and the amount of stretching/displacement. As the strain decreases, the applied stress decreases since there is less elongation along its cross-section. Therefore, when using strains of 40% and 20% there is no elongation/decrease in the cross-section after stretching. This is observed since the strain values higher than 40% show consistent force generation while 40% and 20% show little to zero force generation.

Fatigue cycling the samples showed an initial decrease in peak force and rate, figure 29J-M, after one cycle followed by a relatively constant peak force and rate. Where the onset of force generation is shifted with each cycle, with the largest offset happening after the first cycle. Additionally, the force generation follows a non-linear pattern of contractile force due to the gradient response to thermal input and SR, and actuator spring shape. The SMP responds non-linearly since force generation is initiated prior to the Tg, near 50°C, and continues through the Tg range, near 75°C, along with the spring shape allowing a duel SR effect described above.

Lastly, the FFF actuator was tested in tension to demonstrate the passive tension properties of the design, figure 25C. As the actuator is displaced it provides minimal resistance initially, and then has an exponential increase in resistance to displacement when nearing the complete straightening of the actuator. This spring design allows for the

actuator to have non-linear properties and behave comparable to skeletal muscle in passive movement, strain/shape recovery, and peak force generation[94-99].

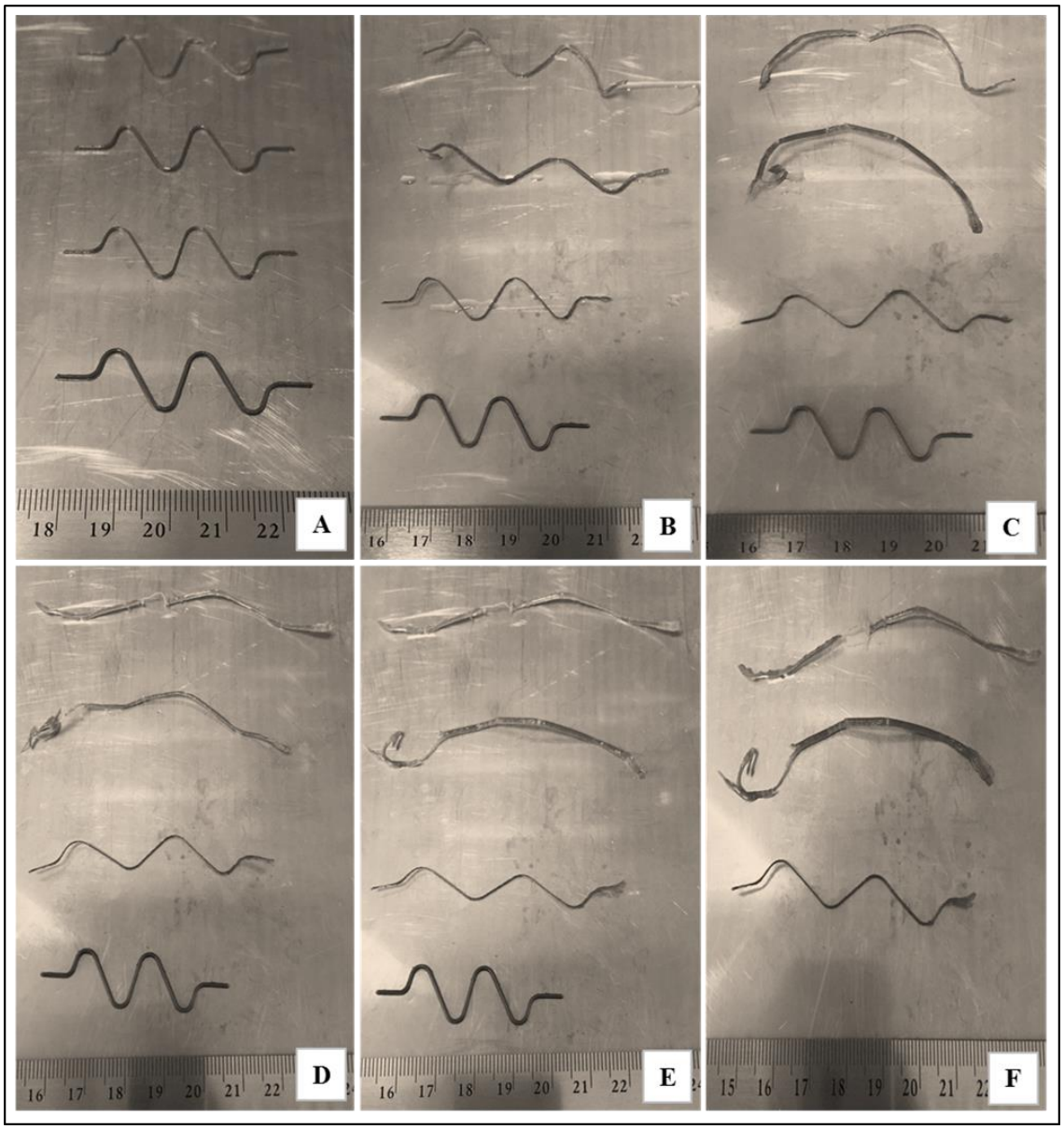

Figure 30. Images A-F show the progress of cyclic fatigue on the FFF actuator. Image A is a baseline, and images B-F are cycles one to five respectively. The top actuator was strained at 100%, the middle actuator was strained at 80%, and then followed by the 60% strained actuator. The bottom actuator in images B-E is a constant unstrained actuator. Plastic deformation and failure is seen in the 100% and 80% strain actuators at minimal cycles, where the 60% strain actuator shows minimal polymer plastic deformation.

ANALYSIS FOR FFF VARIANCES

To determine the cause(s) for variances in contractile data, DSC was used to determine polymer degradation and SEM to evaluate layer adhesion, and print quality of the actuator. The DSC test was heated from 0°C to 300°C and then cooled to 22°C at a rate of 10°/min. The results, figure 26E, show a glass transition (Tg) endothermic event first, followed by a cold crystallization exothermic event second, then the melting temperature (Tm) endothermic event. Upon cooling from 300°C, an exothermic event is seen due to crystallization from annealing. Where an endothermic event represents an absorption of heat in to the sample and an exothermic event represents the release of heat from the sample[103-108].

The cold crystallization event is present since the SMP's content is 70% PLA, which is an amorphous semi-crystalline polymer. Where the TPU has a pseudo crystal structure where the hard segments within the polymer are ordered and the soft segments are amorphous. Once the SMP reaches its Tg, the polymer-chains reorder themselves and increase their crystallization, inducing an exothermic event. If the polymer had high crystallinity originally, then the exothermic event would be minimal or not present.

When comparing the DSC cycles from the SMP filament to FFF actuator, it is visible that thermal degradation is present due to the decrease in specific thermal energy (area under the curve) in each endothermic phase along with the absence of an exothermic event during the transition into the Tg when annealing from 300°C. The

thermal degradation is caused by oxidation and random chain scission due to thermal cycling, which decreases the molecular weight.

Lastly, SEM imaging revealed that the FFF actuator has an inconsistent cross-sectional area (CSA), and layer separation, figure 27B. Images were taken at the ends and center of the actuator and revealed that the layer adhesion is inconsistent throughout the actuator and causes layer separation. Where separation is caused by the cooling of the layer beneath it prior to the next layer being extruded on it and are displayed as parting lines or gaps in the image. Additionally, the CS of the actuator is composed of peaks and valleys instead of constant/straight lines, which causes a variation of the CSA throughout the sample.

FFF ACTUATOR FUTURE WORK

Future work is to use unextruded PLA and TPU pellets prior to creating the SMP composite filament to decrease the amount of thermal degradation and to increase the previous layer's temperature prior to the new layer be extruded on to it. Increasing the previous layer will allow for better adhesion/fusion to the new layer since it will be a resting temperature closer to the extrusion temperature. This will be accomplished with an external heat source and nozzle that will direct heated air, approximately 240°C, directly in front of the extrusion nozzle.

Next, the FFF actuator will be fabricated using the changes listed above and then evaluated using the same tests as before. The results will be used to compared the impact

thermal degradation and layer adhesion have on the design. Lastly, the actuator will be tested for 10, 15, and 20 cycles to see if there is any continual decrease in mechanical results with an increase to fatigue cycles.

CONCLUSION

Presented here is a biomimicking FFF skeletal muscle actuator that demonstrates non-linear properties, peak force and strain comparable to mammalian skeletal muscle, a response time of 0.77sec, low operating temperature at 70°C, and has a low mass (74.0mgrams), volume (46.74mm^3), and material costs of $0.0098 per actuator.

The FFF actuator here has non-linear contractile properties that have peak contractions similar to mammalian muscles ranging from 0.58MPa to 0.17MPa for 100% to 60% strain respectively. Additionally, the ideal strain of 60% has a strain recovery of 29.2%, which is comparable to the 20% for typical mammalian skeletal muscle strain.

CHAPTER SEVEN: CONCLUSION

In conclusion, presented here are initial prosthetic component designs manufactured with Fused Filament Fabrication. A one-step surgical design osseointegration screw is shown with mechanical properties greater than cortical bone and can withstand falls up to six meters. The screw also has an elastic modulus less than cortical resulting in minimal to no stress shielding.

A FFF flexible tactile pressure and shear sensor was developed that can detect early onset of shear movement/forces and detect pressures for daily activities or a light touch. This allows prosthetics to have thin, flexible, biomimicking pressure sensors that can be embedded and fully functional with a FFF system. Additionally, a biomimicking skeletal muscle actuator was created with non-linear contractile and passive forces. The actuator was created with a melt blended shape memory polymer composite. The actuator has peak contractile forces and strain values similar to mammalian skeletal muscles. Additionally, the SMP composite actuator is silent, lightweight, with low overhead cost allowing for prosthetic improvement.

Future directions are to place the osseointegration screw material inside of a sheep or mouse model to confirm that this polyamide six material is as susceptible to bone tissue formation as other polyamide six materials have shown in the past. Additionally, determining the exact chemicals leaching into the PBS solution by running a series of tests with various chemicals used to synthesize polyamide 6 based materials. Once the

chemicals are identified, those chemicals will be tested for cytotoxicity to determine if they will have a negative impact on the human body. Lastly, polyamide 10-12 polymers will be tested for polymer leaching and compared to the polymer presented here to demonstrate the effect of hydrolysis on longer chain length polyamides.

The future direction of the tactile sensors is to develop the sensors with FFF printed electrodes and housing to demonstrate a complete 3d printed tactile sensor system. The housing will allow for the pressure sensor to only see pressure and the shear sensor to only displace in the shear direction. While creating a FFF housing with electrodes and sensor will allow for a complete tactile sensor to be manufactured with one step; decreasing the complexity and assembly needed for a prosthetic tactile sensor.

Lastly, the next direction for the actuator is to reduce the variation in manufacturing to improve its performance. This will be done by eliminating the use of PLA and TPU pellets that have already been extruded prior to melt blending and FFF printing them to reduce thermal degradation. Additionally, the layer adhesion will be increased by elevating the existing FFF layer temperature prior to the next extruded layer.

REFERENCES

1. Amputee Coalition. 'Limb Loss Statistics'. N.p., 2015. Web. 12 Oct. 2015.

2. Ziegler-Graham K, MacKenzie EJ, Ephraim PL, Travison TG, Brookmeyer R. Estimating the Prevalence of Limb Loss in the United States: 2005 to 2050. Archives of Physical Medicine and Rehabilitation 2008;89(3):422-9.

3. Owings M, Kozak LJ, National Center for Health S. Ambulatory and Inpatient Procedures in the United States, 1996. Hyattsville, Md.: U.S. Dept. of Health and Human Services, Centers for Disease Control and Prevention, National Center for Health Statistics; 1998.

4. HCUP Nationwide Inpatient Sample (NIS). Healthcare Cost and Utilization Project (HCUP). Rockville, MD: Agency for Healthcare Research and Quality; 2009.

5. Fisher ES, Goodman DC, Chandra A. Disparities in Health and Health Care among Medicare Beneficiaries: A Brief Report of the Dartmouth Atlas Project. Robert Wood Johnson Foundation2008.

6. Robbins JM, Strauss G, Aron D, Long J, Kuba J, Kaplan Y. Mortality Rates and Diabetic Foot Ulcers. Journal of the American Podiatric Medical Association2008 November 1, 2008;98(6):489-93.

7. Pandian G, Hamid F, Hammond M. Rehabilitation of the Patient with Peripheral Vascular Disease and Diabetic Foot Problems. In: DeLisa JA, Gans BM, editors. Philadelphia: Lippincott-Raven; 1998.

8. National Limb Loss Information Center. Amputation statistics by cause. Limb loss in the United States. NLLIC fact sheet. 2008. Available at: http://www.amputee-coalition.org/fact_sheets/amp_ stats_cause.pdf. Accessed February 6, 2012.

9. Ziegler-Graham K, MacKenzie EJ, Ephraim PL, Travison TG, Brookmeyer R. Estimating the prevalence of limb loss in the United States: 2005 to 2050. Arch Phys Med Rehabil 2008;89: 422-9.

10. Advanced Upper Limb Prosthetic Devices: Implications for Upper Limb Prosthetic Rehabilitation, Resnik, Linda et al., Archives of Physical Medicine and Rehabilitation, Volume 93, Issue 4, 710 – 717

11. Mitka M. Advocates Seek Better Insurance Coverage for Amputees Needing Limb Prostheses. JAMA. 2008;299(18):2138-2140. doi:10.1001/jama.299.18.2138

12. McFarland, Lynne McFarland et al. 'Unilateral Upper-Limb Loss: Satisfaction And Prosthetic-Device Use In Veterans And Service members From Vietnam And OIF/OEF Conflicts'. *Journal of Rehabilitation Research & Development (JRRD)* 47.4 (2010): 299-316. Web. 2010.

13. Stenlund, Patrik. "On the role of surface properties for implant fixation: From finite element modeling to in vivo studies." (2015).

14. Lundberg, Mari, Kerstin Hagberg, and Jennifer Bullington. "My prosthesis as a part of me: a qualitative analysis of living with an osseointegrated prosthetic limb." *Prosthetics and orthotics international* 35.2 (2011): 207-214.

15. Pitkin, M. "Design features of implants for direct skeletal attachment of limb prostheses." *Journal of biomedical materials research Part A* 101.11 (2013): 3339-3348.

16. Wu, Shuilin, et al. "Biomimetic porous scaffolds for bone tissue engineering."*Materials Science and Engineering: R: Reports* 80 (2014): 1-36.

17. Susmita Bose, Sahar Vahabzadeh, Amit Bandyopadhyay, Bone tissue engineering using 3D printing, Materials Today, Volume 16, Issue 12, December 2013, Pages 496-504, ISSN 1369-7021, http://dx.doi.org/10.1016/j.mattod.2013.11.017.

18. Benjamin C. Weed, et al. "3D Printing – Assisted Rapid Prototyping and Optimization: Development of a Novel Small Intestinal Cannula for Equine Research." *3D Printing and Additive Manufacturing.* VOL. 1 NO. 2 • 2014 • DOI: 10.1089/3dp.2013.0008

19. Rose, Austin S., et al. "Pre-operative simulation of pediatric mastoid surgery with 3D-printed temporal bone models." *International journal of pediatric otorhinolaryngology* 79.5 (2015): 740-744.

20. Bernhard, Jean-Christophe, et al. "Personalized 3D printed model of kidney and tumor anatomy: a useful tool for patient education." *World journal of urology* (2015): 1-9.

21. Johnson, Blake N., et al. "3D Printed Anatomical Nerve Regeneration Pathways." *Advanced Functional Materials* 25.39 (2015): 6205-6217.

22. Dally, Corinne, et al. "Characteristics of a 3D-printed prosthetic hand for use in developing countries." *Global Humanitarian Technology Conference (GHTC), 2015 IEEE*. IEEE, 2015.

23. Gretsch, Kendall F., et al. "Development of novel 3D-printed robotic prosthetic for transradial amputees." *Prosthetics and orthotics international* (2015): 0309364615579317.

24. "680 Features." *Taulman 3D*. Web. 8 Jan. 2016.

25. "Nylon 680, 1.75 Mm, 1Lb (Taulman)." *Www.blackmagic3d.com*. Web. 8 Jan. 2016.

26. Abdal-hay, Abdalla, Abdel Salam Hamdy, and Khalil Abdelrazek Khalil. "Fabrication of durable high performance hybrid nanofiber scaffolds for bone tissue regeneration using a novel, simple in situ deposition approach of polyvinyl alcohol on electrospun nylon 6 nanofibers." *Materials Letters* 147 (2015): 25-28.

27. Li, Xiang, et al. "Osteogenesis and chondrogenesis of biomimetic integrated porous PVA/gel/V-n-HA/pa6 scaffolds and BMSCs construct in repair of articular osteochondral defect." *Journal of Biomedical Materials Research Part A* (2015).

28. Sriram, M., et al. "Biomaterials mediated microRNA delivery for bone tissue engineering." *International journal of biological macromolecules* 74 (2015): 404-412.

29. Jothi Lakshmi, D., G. Illakiya, and R. Rajkamal. "A Novel Approach and Design of Embedded Controlled Prosthetic Upper Limb to Assist the Above Elbow Amputees." *Advanced Materials Research*. Vol. 403. 2012.

30. Tsikandylakis, Georgios, Örjan Berlin, and Rickard Brånemark. “Implant Survival, Adverse Events, and Bone Remodeling of Osseointegrated Percutaneous Implants for Transhumeral Amputees.” *Clinical Orthopaedics and Related Research* 472.10 (2014): 2947–2956. *PMC*. Web. 11 Jan. 2016.

31. Miquel Domingo-Espin, Salvador Borros, Nuria Agullo, Andres-Amador Garcia – Granada, and Guillermo Reyes. “Influence of Building Parameters on the Dynamic Mechanical Properties of Polycarbonate Fused Deposition Modeling Parts.” *3D Printing and Additive Manufacturing*. VOL. 1 NO. 2 • 2014 • DOI: 10.1089/3dp.2013.0007

32. Chiu, James, and Stephen N. Robinovitch. "Prediction of upper extremity impact forces during falls on the outstretched hand." *Journal of biomechanics* 31.12 (1998): 1169-1176.

33. Cairns, Nicola J., et al. "Ability of modal analysis to detect osseointegration of implants in transfemoral amputees: a physical model study." *Medical & biological engineering & computing* 51.1-2 (2013): 39-47.

34. Welke, Bastian et al. "Stiffness and Ultimate Load of Osseointegrated Prosthesis Fixations in the Upper and Lower Extremity." *BioMedical Engineering OnLine* 12 (2013): 70. *PMC*. Web. 7 Jan. 2016.

35. Jeyapalina, Sujee, et al. "Progression of bone ingrowth and attachment strength for stability of percutaneous osseointegrated prostheses." *Clinical Orthopaedics and Related Research®* 472.10 (2014): 2957-2965.

36. Pal, Subrata. *Design of Artificial Human Joints & Organs, Chapter 2 Mechanical Properties of Biological Materials*. Springer US, 2014.

37. Mastronardi, L., A. Ducati, and L. Ferrante. "Anterior cervical fusion with polyetheretherketone (PEEK) cages in the treatment of degenerative disc disease. Preliminary observations in 36 consecutive cases with a minimum 12-month follow-up." *Acta neurochirurgica* 148.3 (2006): 307-312.

38. Lathers, Steven, and Jeffrey La Belle. "Advanced Manufactured Fused Filament Fabrication 3D Printed Osseointegrated Prosthesis for a Transhumeral Amputation Using Taulman 680 FDA." *3D Printing and Additive Manufacturing* 3.3 (2016): 166-174.

39. "680 Features." *Taulman 3D*. Web. 8 Jan. 2016.

40. "Nylon 680, 1.75 Mm, 1Lb (Taulman)." *Www.blackmagic3d.com*. Web. 8 Jan. 2016.

41. Abdal-hay, Abdalla, Abdel Salam Hamdy, and Khalil Abdelrazek Khalil. "Fabrication of durable high performance hybrid nanofiber scaffolds for bone tissue regeneration using a novel, simple in situ deposition approach of polyvinyl alcohol on electrospun nylon 6 nanofibers." *Materials Letters* 147 (2015): 25-28.

42. Li, Xiang, et al. "Osteogenesis and chondrogenesis of biomimetic integrated porous PVA/gel/V-n-HA/pa6 scaffolds and BMSCs construct in repair of articular osteochondral defect." *Journal of Biomedical Materials Research Part A* (2015).

43. Sriram, M., et al. "Biomaterials mediated microRNA delivery for bone tissue engineering." *International journal of biological macromolecules* 74 (2015): 404-412.

44. Karmella A. Haynes and Pamela A. Silver. "Synthetic Reversal of Epigenetic Silencing." *THE JOURNAL OF BIOLOGICAL CHEMISTRY*, VOL. 286, NO. 31, pp. 27176 –27182, August 5, 2011

45. Iván Navarro-Baena, Valentina Sessini, Franco Dominici, Luigi Torre, Jose M. Kenny, Laura Peponi, Design of biodegradable blends based on PLA and PCL: From morphological, thermal and mechanical studies to shape memory behavior, Polymer Degradation and Stability, Volume 132, October 2016, Pages 97-108, ISSN 0141-3910, http://dx.doi.org/10.1016/j.polymdegradstab.2016.03.037.

46. Jothi Lakshmi, D., G. Illakiya, and R. Rajkamal. "A Novel Approach and Design of Embedded Controlled Prosthetic Upper Limb to Assist the Above Elbow Amputees." *Advanced Materials Research*. Vol. 403. 2012.

47. Tsikandylakis, Georgios, Örjan Berlin, and Rickard Brånemark. "Implant Survival, Adverse Events, and Bone Remodeling of Osseointegrated Percutaneous Implants for Transhumeral Amputees." *Clinical Orthopaedics and Related Research* 472.10 (2014): 2947–2956. *PMC*. Web. 11 Jan. 2016.

48. Miquel Domingo-Espin, Salvador Borros, Nuria Agullo, Andres-Amador Garcia – Granada, and Guillermo Reyes. "Influence of Building Parameters on the Dynamic Mechanical Properties of Polycarbonate Fused Deposition Modeling Parts." *3D Printing and Additive Manufacturing*. VOL. 1 NO. 2 • 2014 • DOI: 10.1089/3dp.2013.0007

49. Chan LK, Leung VY, Tam V, et al.: Decellularized bovine intervertebral disc as a natural scaffold for xenogenic cell studies. Acta Biomater 9:5262-5272, 2013.

50. ISO 10993-1, "Biological evaluation of medical devices - Part 1: Evaluation and testing within a risk management process". Guidance for Industry and Food and Drug Administration Staff. Issued on April 23, 2013.

51. Mihai, R et al. "In Vitro Biocompatibility Testing of Some Synthetic Polymers Used for the Achievement of Nervous Conduits ." *Journal of Medicine and Life* 4.3 (2011): 250–255. Print.

52. Morrison, C., et al. "In vitro biocompatibility testing of polymers for orthopaedic implants using cultured fibroblasts and osteoblasts." *Biomaterials* 16.13 (1995): 987-992.

53. Lackie JM. *The Dictionary of Cell and Molecular Biology*. 2012. p.249

54. Welke, Bastian et al. "Stiffness and Ultimate Load of Osseointegrated Prosthesis Fixations in the Upper and Lower Extremity." *BioMedical Engineering OnLine* 12 (2013): 70. *PMC*. Web. 7 Jan. 2016.

55. Chiu, James, and Stephen N. Robinovitch. "Prediction of upper extremity impact forces during falls on the outstretched hand." *Journal of biomechanics* 31.12 (1998): 1169-1176.

56. Cairns, Nicola J., et al. "Ability of modal analysis to detect osseointegration of implants in transfemoral amputees: a physical model study." *Medical & biological engineering & computing* 51.1-2 (2013): 39-47.

57. Cho, Hyun-Seok, et al. "The contamination mechanism and behavior of amide bond containing organic contaminant on PEMFC." *Journal of The Electrochemical Society* 162.4 (2015): F427-F435.

58. Wang, Xiaohui, et al. "Morphology and thermal properties of nylon copolymers containing dimer acid, adipic acid, and hexamethylenediamine." *Journal of Applied Polymer Science* 119.5 (2011): 2511-2516.

59. Guerrini, Luca, et al. "α, ω-aliphatic diamines as molecular linkers for engineering Ag nanoparticle clusters: tuning of the interparticle distance and sensing application." *Plasmonics* 5.3 (2010): 273-286.

60. Allen, Norman S., and Alan Parkinson. "Ultraviolet derivative absorption spectra of nylon 6, 6: Effect of photolysis versus photo-induced oxidation." *Polymer Degradation and Stability* 4.4 (1982): 239-244.

61. Tokiwa, Yutaka et al. "Biodegradability of Plastics." *International Journal of Molecular Sciences* 10.9 (2009): 3722–3742. *PMC*. Web. 29 Jan. 2017.

62. Mohsin I. Tiwana, Stephen J. Redmond, Nigel H. Lovell, A review of tactile sensing technologies with applications in biomedical engineering, Sensors and Actuators A:

Physical, Volume 179, June 2012, Pages 17-31, ISSN 0924-4247, http://dx.doi.org/10.1016/j.sna.2012.02.051.

63. Hahn, Gábor Harsányi-Emil. "Thick-film pressure sensors." *Mechatronics* 3.2 (1993): 167-171.

64. Park, Jonghwa, et al. "Giant tunneling piezoresistance of composite elastomers with interlocked microdome arrays for ultrasensitive and multimodal electronic skins." *ACS nano* 8.5 (2014): 4689-4697.

65. Zhu, Bowen, et al. "Microstructured graphene arrays for highly sensitive flexible tactile sensors." *Small* 10.18 (2014): 3625-3631.

66. Shao, Qi, et al. "High-Performance and Tailorable Pressure Sensor Based on Ultrathin Conductive Polymer Film." *Small* 10.8 (2014): 1466-1472.

67. Mascaro, S., & Asada, H. (2001). Photoplethysmograph fingernail sensors for measuring finger forces without haptic obstruction. *IEEE Trans. Robot. Automat. IEEE Transactions on Robotics and Automation, 17*(5), 698-708. doi:10.1109/70.964669

68. Gong, Shu, et al. "A wearable and highly sensitive pressure sensor with ultrathin gold nanowires." *Nature communications* 5 (2014).

69. Pan, L., Chortos, A., Yu, G., Wang, Y., Isaacson, S., Allen, R., . . . Bao, Z. (2014). An ultra-sensitive resistive pressure sensor based on hollow-sphere microstructure induced elasticity in conducting polymer film. *Nature Communications Nat Comms, 5*. doi:10.1038/ncomms4002

70. Schwartz, G., Tee, B. C., Mei, J., Appleton, A. L., Kim, D. H., Wang, H., & Bao, Z. (2013). Flexible polymer transistors with high pressure sensitivity for application in electronic skin and health monitoring. *Nature Communications Nat Comms, 4*, 1859. doi:10.1038/ncomms2832

71. Park, S., Kim, H., Vosgueritchian, M., Cheon, S., Kim, H., Koo, J. H., . . . Bao, Z. (2014). Stretchable Energy-Harvesting Tactile Electronic Skin Capable of Differentiating Multiple Mechanical Stimuli Modes. *Adv. Mater. Advanced Materials, 26*(43), 7324-7332. doi:10.1002/adma.201402574

72. Choong, C., Shim, M., Lee, B., Jeon, S., Ko, D., Kang, T., . . . Chung, U. (2014). Highly Stretchable Resistive Pressure Sensors Using a Conductive Elastomeric Composite on a Micropyramid Array. *Adv. Mater. Advanced Materials, 26*(21), 3451-3458. doi:10.1002/adma.201305182

73. Mannsfeld, Stefan CB, et al. "Highly sensitive flexible pressure sensors with microstructured rubber dielectric layers." *Nature materials* 9.10 (2010): 859-864.

74. Gerratt, Aaron P., Hadrien O. Michaud, and Stéphanie P. Lacour. "Elastomeric electronic skin for prosthetic tactile sensation." *Advanced Functional Materials* 25.15 (2015): 2287-2295.

75. Wettels, Nicholas, et al. "Grip control using biomimetic tactile sensing systems." *IEEE/ASME Transactions On Mechatronics* 14.6 (2009): 718-723.

76. Laurent, A., Mistretta, F., Bottigioli, D., Dahel, K., Goujon, C., Nicolas, J. F., Laurent, P. E. (2007). Echographic measurement of skin thickness in adults by high frequency ultrasound to assess the appropriate microneedle length for intradermal delivery of vaccines. *Vaccine, 25*(34), 6423-6430. doi:10.1016/j.vaccine.2007.05.046

77. Dubey, P. (2016, January). DEPENDENCE OF ABSORPTION AND SCATTERING SPECTRUM OVER MELANIN CONCENTRATION. *International Journal of Engineering Sciences & Emerging Technologies, 8*(4), 202-207.

78. Miquel Domingo-Espin, Salvador Borros, Nuria Agullo, Andres-Amador Garcia – Granada, and Guillermo Reyes. "Influence of Building Parameters on the Dynamic Mechanical Properties of Polycarbonate Fused Deposition Modeling Parts." *3D Printing and Additive Manufacturing*. VOL. 1 NO. 2 • 2014 • DOI: 10.1089/3dp.2013.0007

79. Matsuzaki, Ryosuke et al. "Three-Dimensional Printing of Continuous-Fiber Composites by in-Nozzle Impregnation." *Scientific Reports* 6 (2016): 23058. *PMC*. Web. 9 Jan. 2017.

80. NIIR Board of Consultants and Engineers. *The Complete Technology Book on Plastic Extrusion, Moulding And Mould Designs*. N.p.: NATIONAL INSTITUTE OF INDUSTRIAL RESEARCH, 2006. Print.

81. Ibrahim, M. Ibrahim, N. Isa, N. Sa'ude, and M. Ibrahim. "VERIFICATION OF FEED RATE EFFECTS ON FILAMENT EXTRUSION FOR FREEFORM FABRICATION." *ARPN Journal of Engineering and Applied Sciences* 11.10 (2016): 6556-561. Web.

82. Chandler RF, Clauser DE, McMconville JT, Reynolds HM, Young JW. Investigation of inertial properties of the human hand. Washington (DC): U.S. Department of Transportation; 1975 Mar. Report No. DOT HS-801 430.

83. Tözeren A. Human body dynamics: Classical mechanic and human movement. New York (NY): Springer; 2000.

84. D.W. Repperger, C.A. Phillips, A. Neidhard-Doll, D.B. Reynolds, J. Berlin, Actuator design using biomimicry methods and a pneumatic muscle system, Control Engineering Practice, Volume 14, Issue 9, 2006, Pages 999-1009, ISSN 0967-0661, http://dx.doi.org/10.1016/j.conengprac.2005.06.009.

85. Kim, Sangbae, and Et Al. "Soft robotics: a bioinspired evolution in robotics." *Trends in Biotechnology*31.5 (2013): n. pag. Web.

86. Sreekumar, M. "Critical review of current trends in shape memory alloy actuators for intelligent robots." *Industrial Robot*34.4 (2007): 285-94. Web.

87. Carter S. Hanes, et al. Artificial Muscles from Fishing Line and Sewing Thread, *Science*, Volume 343, Issue 6173, PP. 868-872, DOI: 10.1126/science.1246906

88. Feinberg, A. W., A. Feigel, S. S. Shevkoplyas, S. Sheehy, G. M. Whitesides, and K. K. Parker. "Muscular Thin Films for Building Actuators and Powering Devices." *Science*317.5843 (2007): 1366-370. Web.

89. Cvetkovic, C., R. Raman, V. Chan, B. J. Williams, M. Tolish, P. Bajaj, M. S. Sakar, H. H. Asada, M. T. A. Saif, and R. Bashir. "Three-dimensionally printed biological machines powered by skeletal muscle." *Proceedings of the National Academy of Sciences*111.28 (2014): 10125-0130. Web.

90. Baughman, Ray H. "Playing Nature's Game with Artificial Muscles." *Science*, vol. 308, no. 5718, 2005, pp. 63–65. *JSTOR*, www.jstor.org/stable/3841393.

91. Hosseini V, Ahadian S, Ostrovidov S, et al. Engineered Contractile Skeletal Muscle Tissue on a Microgrooved Methacrylated Gelatin Substrate. *Tissue Engineering Part A*. 2012;18(23-24):2453-2465. doi:10.1089/ten.tea.2012.0181.

92. Gu, B. K., et al. (2009). A Linear Actuation of Polymeric Nanofibrous Bundle for Artificial Muscles. *Chemistry of Materials*,*21*(3), 511-515.

93. Bailey, Sean A., Jorge G. Cham, Mark R. Cutkosky, and Robert J. Full. "Biomimetic Robotic Mechanisms via Shape Deposition Manufacturing." *Robotics Research*(2000): 403-10. Web.

94. Bottinelli, R., M. Canepari, M. A. Pellegrino, and C. Reggiani. "Force-velocity properties of human skeletal muscle fibres: myosin heavy chain isoform and temperature dependence." *The Journal of Physiology*495.2 (1996): 573-86. Web.

95. Bottinelli, R., S. Schiaffino, and C. Reggiani. "Force-velocity relations and myosin heavy chain isoform compositions of skinned fibres from rat skeletal muscle." *The Journal of Physiology*437.1 (1991): 655-72. Web.

96. Josephson, R K. "CONTRACTION DYNAMICS AND POWER OUTPUT OF SKELETAL MUSCLE." *Annual review of physiology*. Vol. 55, Issue 1, (1993): 527-546

97. Madden, John. "Artificial Muscle Technology: Physical Principles and Naval Prospects." *IEEE Journal of Oceanic Engineering*29.3 (2004): 706-28. Web.

98. Oatis, Carol A. *Kinesiology: the mechanics and pathomechanics of human movement*. 2nd ed. N.p.: LWW, 2008. Print. Chapter 4

99. Martini, and Bartholomew. *Essentials of Anatomy & Physiology*. 6th ed. N.p.: n.p., 2007. Print. Chapter 7

100. Jing, Xin, et al. "Injection molding of novel polylatic acid/thermoplstic polyurethane (PLA/TPU) blends with shape-memory behavior." *POLYMER ENGINEERING AND SCIENCE*(2014): 1-9. Web. DOI: 10.1002/pen

101. Navarro-Baena, Iván, Valentina Sessini, Franco Dominici, Luigi Torre, Jose M. Kenny, and Laura Peponi. "Design of biodegradable blends based on PLA and PCL: From morphological, thermal and mechanical studies to shape memory behavior." *Polymer Degradation and Stability*132 (2016): 97-108. Web.

102. Pavia, Lampmanm Kriz, and Vyvyan. *Introduction to Spectroscopy*. 5th ed. Cengage Learning, 2014. Print.

103. Ramani, A., and A.e. Dahoe. "On flame retardancy in polycaprolactam composites by aluminium diethylphosphinate and melamine polyphosphate in conjunction with organically modified montmorillonite nanoclay." *Polymer Degradation and Stability*105 (2014): 1-11. Web.

104. Larrégola, Sebastián A., José A. Alonso, Denis Sheptyakov, Miguel Algueró, Angel Muñoz, Vladimir Pomjakushin, and José C. Pedregosa. "An Original Polymorph Sequence in the High-Temperature Evolution of the Perovskite Pb2TmSbO6." *Journal of the American Chemical Society*132.41 (2010): 14470-4480. Web.

105. PerkinElmer, Inc. (2014). Differential Scanning Calorimetry (DSC) – A Beginners Guide. Waltham, MA

106. EAG Laboratories (2016). Characterization of Polymers Using Differential Scanning Calorimetry (DSC) White Page. San Diego, CA.

107. Mettler-Toledo AG Laboratory Division (2013) Thermal Analysis of Polymers – Application Handbook. Greifensee, Switzerland

108. Yutaka Obata, et al. "Bulk Properties of Syndiotactic 1,2-Polybutadiene. III. Melting and Crystallization Properties." *Polymer Journal*. Vol 7, Issue 3, PP 312-319

APPENDIX A

MOLDED FLEX SENSOR FABRICATED WITH SEBS-CARBON COMPOSITE

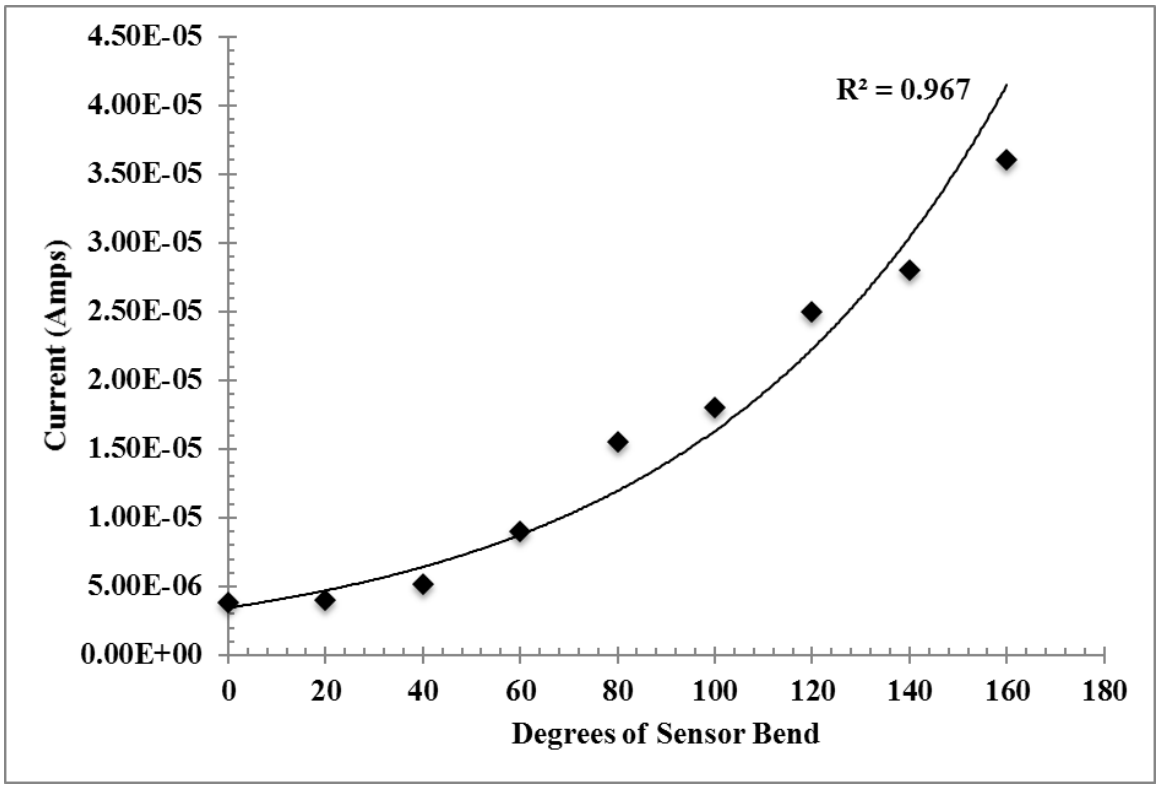

Figure A1. Plotted data of current output with a molded flex sensor fabricated with SEBS-Carbon with an applied voltage of 0.2Volts. Flex sensor was design with dimensions as follow: 15mmx2.5x2.5mm.

APPENDIX B

FUSED FILAMENT FABRICATION (FFF) GENERAL PROTOCOL

To obtain optimal fused filament fabricated (FFF) parts, it is best to follow the general protocol rules below. In FFF, a solid polymer filament is fed through a heating chamber and extruded out the heated nozzle out to a bed /platform. When the polymer is extruded, it enters a molten state with a decrease in viscosity. This decrease in viscosity decreases the control that the polymer has when extruded out the nozzle. To increase the control or placement of the molten material during the fabrication of each layer, it is best to use a low printing speed with a zero z-axis gap to the nozzle and bed, first rule.

For example, when printing with a polyamide based material, it is best to use a printing speed of 600mm/min. If a higher printing speed is used, i.e. 5000mm/min, it can create gaps or prevent a layer from being fabricated. With the increased speed, the molten material can not adhere to the layer it is printing on top of. Since the system uses thermal energy to create layer adhesion, a slow speed is required since high speeds decrease material extrusion temperature from convection and allow the nozzle to move faster than the filament feeder can extrude material. Additionally, the vibrations and harshness from the high-speed decreases part dimensional quality.

Second rule is to follow is the use of an external adhesive or surface to increase the adhesion of the first layer to the bed/platform. When printing on to a metal or glass bed, the edges or part can detach from the bed from the low surface texture or adhesion properties. Commonly, a heated bed with Kapton tape is used to prevent this event, but this generally only works for short print times or small parts. To overcome this, it is best to use an adhesive or increasing the bed surface texture.

An adhesive, such as Poly-vinyl acetate (PVA) based glue, is best since it provides adequate adhesion of the layer to the bed or bed with Kapton tape. The adhesive can easily be cleaned with water to dissolve the PVA. Additionally, the surface texture can be enhanced by using tape or etching the surface. The increased surface texture or roughness allows the polymer of the first layer to fill in to the groves and increases the contact surface area.

Third rule is to decrease or remove the cooling fan speed that is directed at the FFF part, not the filament feeder system/gear. The cooling generate by the fan decreases the thermal energy within the molten and printed layers and decreases the adhesion affect. It is best to modify the extruder temperature and feeder gear multiplier to adjust for the cooling fan.

Fourth rule is to manually decrease the software's nozzle diameter representation and increase the extrusion multiple for thin features. If you have a thin line, 0.4mm in width with a 0.35mm nozzle diameter, it is best to use an extrusion width of 0.39 with a multiplier of 0.97.

Lastly, rule five, is to use a filament de-tensioner system when the filament is being pulled through the filament feeder system. If there is too much back tension on the filament, the filament may slip on the feeder gear and prevent full material extrusion displacement.

APPENDIX C

STEREOLITHOGRAPHY (SLA) GENERAL PROTOCOL

Here, the key features for fabricating SLA parts on a Forms Lab system is presented below. Due to the close nature of the equipment and software, there are only a few rules that need to be followed. First rule is to confirm that the reservoir is filled with the correct resin and is filled to the black indicator line.

Second, all partially cured or hardened resin needs to be removed from the reservoir and bed, this can be accomplished by running a dull blade along the bottom of the reservoir and bed. This will remove any hardened resin from the reservoir and allow the light source to pass through the reservoir. If the light source cannot pass through the reservoir, the photocatalyst cannot be activated and therefore prevent any resin curing. While cleaning the bed will allow for the bed to position itself correctly without the bed being offset from the hardened resin.

Third rule is to use the orientation and support structure buttons, figure C2, to place the part in the optimal orientation for SLA fabrication and have enough support material. Additionally, when using the support structure button, it is best to review the support structure preview and manually add or modify the support.

If there are any red highlighted areas on the part, it is best to place a new support structure there. A red highlight represents a location were the software is unsure if it can successfully place material there. While modifying the structure is done by adjusting the structure contact point size and thickness. By increasing or decreasing the contact area and thickness, the printed part quality can be optimized.

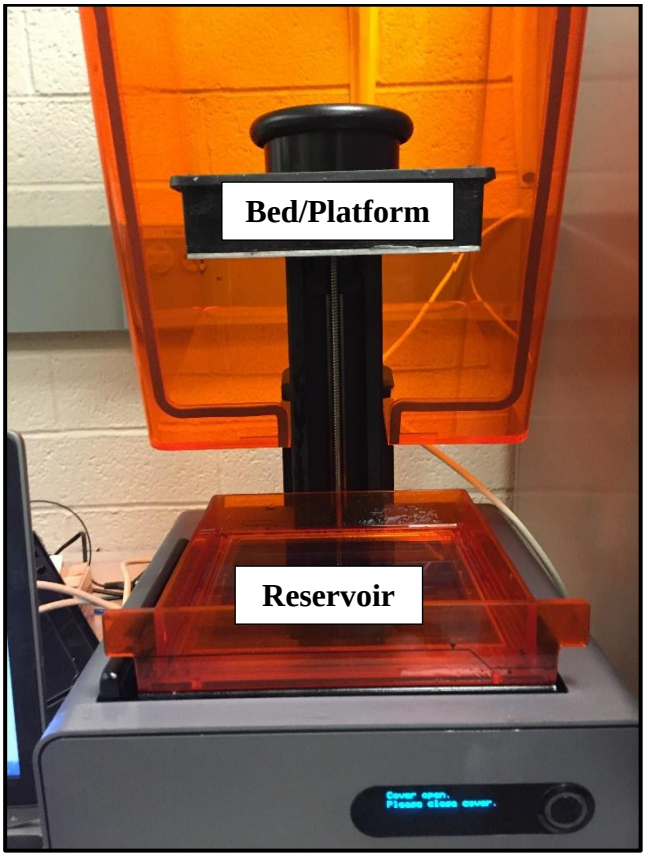

Figure C1. Top platform is the aluminum build platform for SLA parts. The bottom tank or reservoir holds the monomers and photocatalyst required for SLA fabrication.

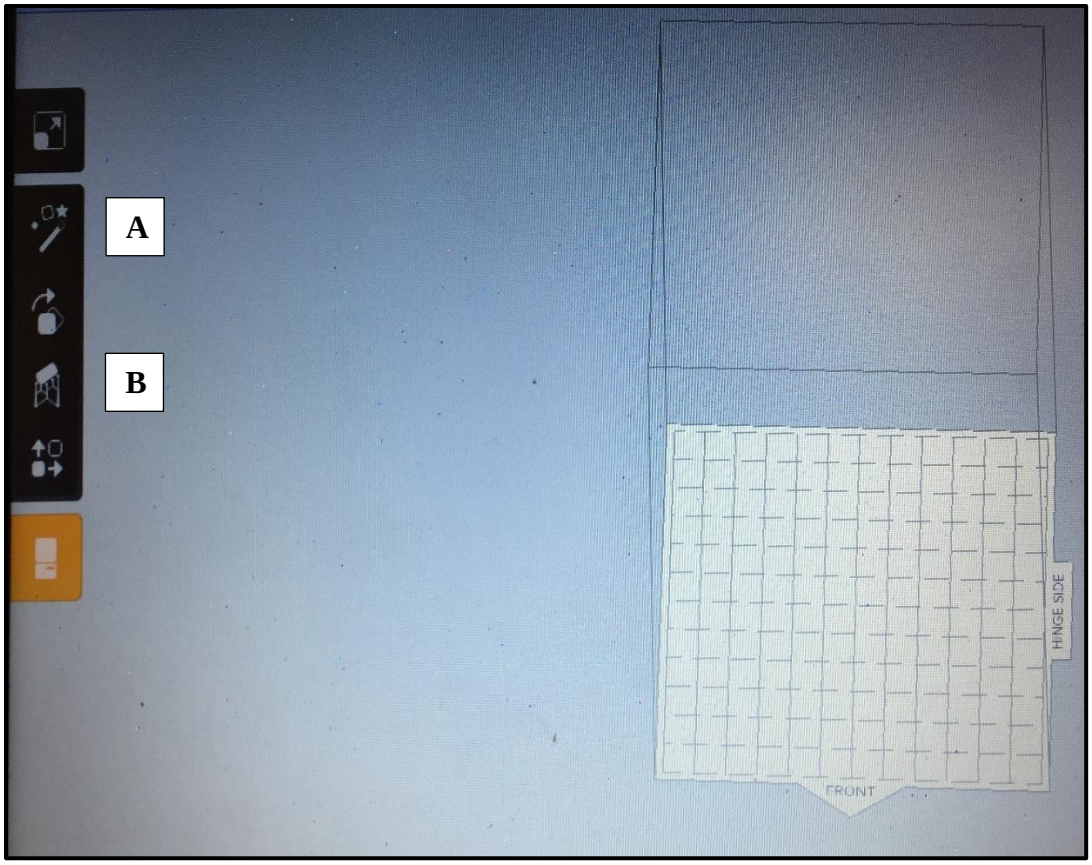

Figure C2. Forms Lab SLA printing software setup. Optimal orientation button (Left of A) and support structure generation button (Left of B).